POLITECNICO
MILANO 1863

SCUOLA DI INGEGNERIA INDUSTRIALE
E DELL'INFORMAZIONE

A numerical study on the effects of laser refractive surgery: PRK vs SMILE

Tesi di Laurea Magistrale in
Biomedical Engineering - Ingegneria Biomedica

Author: **Gaia Caruso**

Student ID: 993571
Advisor: Prof. Rodriguez Matas José Felix
Co-advisors: Prof. Begoña Calvo, Benedetta Fantaci
Academic Year: 2022-2023

Abstract

The cornea is the transparent outer layer of the eye and provides 2/3 of the total refractive power of the eye. Its structure is characterized by the presence of a highly organized network of collagen fibers, which ensures its optical and mechanical properties.
Vision defects such as myopia, hyperopia and astigmatism are one of the most common causes of visual impairments on the world. Over the last two decades, laser refractive surgeries have become increasingly popular in vision defects treatment.
Photorefractive Keratectomy (PRK) and Small Incision Lenticule Extraction (SMILE) are two of the current surgical techniques that, through laser ablation, change the curvature of the anterior surface of the cornea, increasing its refracting power and leading to increased visual acuity.
In this work, both PRK and SMILE surgeries have been computationally modeled by means of Finite Element Method (FEM). The aim of the work is to characterize the two surgeries from an opto-mechanical point of view and to further determine which geometrical, optical and mechanical parameters mostly affect the outcome of the mathematical simulations. Moreover, a validation of the surgery models is carried out, through the comparison of the models built on patient-specific data with the real surgery outcomes of the same patient.

The models are developed using two geometrical approximations: a conic geometry and a patient-specific geometry, derived from the Pentacam device. The biomechanical features of the cornea are modeled using a hyperelastic, fiber-reinforced material. The models are built and meshed using ANSA pre-processor by BETA-CAE. The FEM simulations are run on ABAQUS 6.13 and simulate the action of the intraocular pressure (IOP) and of the laser surgery ablation. The simulations outcomes are analysed from a mechanical and optical point of view, looking at the maximum principal stresses distributions on the corneal surfaces, at the maximum principal logarithmic strains, at the anterior surface displacements [µm] and at the changes in curvature of the anterior surfaces [D].

The finite element simulations show an overall higher correction of the defect in PRK surgery, at equal geometrical set up. Moreover, to correct the same refractive defect, in SMILE surgery it is necessary to eliminare a bigger volume of corneal tissue. The

SMILE simulations confirmed the current clinical practice to perform the surgery in a range of 110-120 µm depth from the anterior surface, while higher depths lead to higher stress distributions on the posterior surface of the cornea, which can eventually cause post-surgical complications like ectasia disease and keratoconus.

The validation of the models revealed the best suitable material parameters through which the dioptric correction best approximates the patient's one. Moreover, the mechanical outputs show that stresses and strains are more homogeneous in corneal thickness for PRK procedure, while SMILE causes mechanical imbalances in the volume under the lenticule extraction area.

These studies have allowed the construction of numerical models of the two refractive surgeries considered, paving the way for modeling a new material that simulates corneal tissue and for simulating pathological corneal models.

Keywords: Cornea, Photorefractive Keratectomy (PRK), Small Incision Lenticule Extraction (SMILE), refractive surgery, numerical simulation

Abstract in lingua italiana

La cornea è lo strato esterno trasparente dell'occhio e fornisce i 2/3 del potere rifrattivo dell'occhio. La sua struttura è caratterizzata dalla presenza di una rete altamente organizzata di fibre di collagene, che ne assicura le proprietà ottiche e meccaniche.
La miopia, l'ipermetropia e l'astigmatismo sono le cause più comuni di disturbi visivi nel mondo. Negli ultimi due decenni, le chirurgie refrattive laser sono diventate sempre più popolari nel trattamento dei difetti visivi.
La Photorefractive Keratectomy (PRK) e la Small Incision Lenticule Extraction (SMILE) sono due delle attuali tecniche chirurgiche che, attraverso l'ablazione laser, modificano la curvatura della superficie anteriore della cornea, aumentandone il potere refrattivo e migliorando la capacità visiva.
In questo lavoro, sono state modellate computazionalmente entrambe le chirurgie, PRK e SMILE, mediante il metodo degli elementi finiti (FEM). Lo scopo del lavoro è stato caratterizzare le due procedure da un punto di vista opto-meccanico per determinare quali parametri geometrici, ottici e meccanici influiscono maggiormente sull'esito delle simulazioni matematiche. Inoltre, i modelli sono stati convalidati attraverso il confronto con dati specifici di pazienti sottoposti alle procedure chirurgiche, al fine di verificare se i modelli riflettessero la pratica clinica attuale.

I modelli sono stati sviluppati utilizzando due geometrie: una geometria conica e una basata sull'utilizzo di dati specifici di pazienti forniti dal dispositivo diagnostico Pentacam. Le caratteristiche biomeccaniche della cornea sono state modellate utilizzando un materiale iperelastico costituito da fibre. I modelli sono stati creati e meshati utilizzando il software ANSA BETA-CAE pre-processor. Le simulazioni FEM sono state eseguite su ABAQUS 6.13 e hanno riprodotto la pressione intraoculare (IOP) e l'ablazione della chirurgia. Gli esiti delle simulazioni sono stati analizzati da un punto di vista meccanico e ottico, osservando le distribuzioni degli sforzi principali massimi [kPa] sulle superfici corneali, le deformazioni principali massime logaritmiche [-], gli spostamenti della superficie anteriore [µm] e le variazioni nella curvatura delle superfici anteriori [D].

Le simulazioni a elementi finiti mostrano una correzione complessivamente maggiore del difetto nella chirurgia PRK rispetto alla SMILE, a parità di configurazione geometrica.

Inoltre, per correggere lo stesso difetto rifrattivo, la chirurgia SMILE richiede l'estrazione di più tessuto corneale rispetto alla PRK. Le simulazioni della SMILE hanno confermato la pratica clinica attuale, che consiste nell'eseguire la chirurgia in un intervallo di profondità compreso tra 110-120 µm dalla superficie anteriore, mentre profondità maggiori nello spessore corneale causano stress maggiori sulla superficie posteriore della cornea, che possono causare ectasia corneale e la comparsa del cheratocono.

La convalida dei modelli ha rivelato i parametri del materiale più adatti attraverso i quali la correzione diottrica si avvicina meglio a quella del paziente. Inoltre, gli output meccanici mostrano che gli sforzi e le deformazioni sono più omogenei nello spessore corneale per la PRK, mentre la SMILE causa squilibri meccanici nell'area immediatamente sotto a dove è stata estratta la lenticola.

Questi studi hanno permesso di costruire dei modelli numerici per le due chirurgie rafrattive, aprendo la strada per la modellizzazione di un nuovo materiale che simuli il tessuto corneale e per poter simulare in futuro modelli patologici di cornea.

Parole chiave: Cornea, Photorefractive Keratectomy (PRK), Small Incision Lenticule Extraction (SMILE), chirurgia refrattiva, simulazione numerica

Contents

Abstract **i**

Abstract in lingua italiana **iii**

Contents **v**

1 Introduction **1**
1.1 Myopia: a worldwide problem . . . 1
1.2 Eye and cornea . . . 2
1.2.1 Corneal anatomy and physiology . . . 2
1.3 Clinical diagnostics of the cornea . . . 5
1.4 Average corneal dimensions . . . 7
1.5 Corneal Biomechanics . . . 7
1.6 Optics . . . 10
1.7 Refractive Disorders . . . 12
1.7.1 Myopia . . . 12
1.7.2 Hyperopia . . . 13
1.7.3 Astigmatism . . . 13
1.8 Vision impairments correction . . . 14
1.8.1 Vision aids . . . 14
1.8.2 Corneal refractive surgeries . . . 15
1.8.3 Surgery Complications . . . 18
1.9 Aim of the thesis . . . 19

2 Materials and Methods **21**
2.1 Geometry of the Cornea . . . 21
2.1.1 Conic Model . . . 22
2.1.2 Ablation Profile . . . 23
2.2 FE Model . . . 24

2.3 Material model . . . 25
2.4 Boundary Conditions . . . 28
2.5 Zero-Pressure . . . 29
2.6 Laser Surgery FE Simulations . . . 31
2.6.1 PRK simulation . . . 31
2.6.2 SMILE simulation . . . 32
2.7 Opto-mechanical Analysis of the simulations . . . 33
2.8 Simulations . . . 35
2.8.1 Lenticule Position analysis in SMILE surgery simulation . . . 36
2.8.2 Dioptric target correction variation . . . 37
2.8.3 CCT variation . . . 38
2.8.4 OZ radius variation . . . 39
2.8.5 Sensitivity analysis: 2^5 full factorial design . . . 39
2.8.6 Montecarlo analysis . . . 42
2.9 Patient-Specific Models . . . 42
2.9.1 PRK surgery . . . 45
2.9.2 SMILE surgery . . . 46

3 Results **49**
3.1 Boundary Conditions analysis . . . 49
3.1.1 Mechanical results . . . 50
3.1.2 Optical Results . . . 53
3.2 Lenticule position in SMILE Surgery . . . 57
3.3 Dioptric corrections analysis . . . 63
3.4 OZ radius . . . 68
3.5 Central corneal thickness . . . 69
3.6 Full-Factorial analysis . . . 74
3.7 Montecarlo analysis . . . 78
3.8 Patient-specific models . . . 80

4 Discussion **91**

5 Conclusions and future developments **99**
5.1 Conclusions . . . 99
5.2 Limits and Future Developments . . . 100

Bibliography **103**

List of Figures **109**

List of Tables **115**

Acknowledgements **117**

1 | Introduction

1.1. Myopia: a worldwide problem

The main refractive defects, are myopia, hyperopia, astigmatism and presbyopia. Refractive errors occur when the eye is unable to bend and focus light appropriately onto the retina. Vision may become blurry, hazy, or doubled, causing you to squint and strain the eyes. Myopia, also called nearsightedness, is the inability to see distant objects clearly and it is a complex eyesight-threatening disease. It is becoming the major cause of blindness and the myopic population is progressively increasing. About one fifth of myopic population is affected by high myopia (i.e. a defect higher than 6 dioptres), which can lead to irreversible vision loss due to retinal detachment, cataracts, macular atrophy, glaucoma and choroidal neovascularization [20]. According to the World Health Organisation (WHO) report, people that have a vision impairment are at least 2.2 billion, among which one billion could have prevented their disease. In this group, the condition causing these vision impairments is the development of refractive errors for 88.4 million of people [3]. Furthermore, distance vision impairments are prevalent in low and middle income regions four times more than in high income regions [10]. Myopia prevalence is considerably high, especially in Asian countries. A review estimated that in 2050, half of the global population (5 billion people) would be myopic, and one fifth of those (1 billion) would be considered highly myopic. Moreover, progression of myopia is faster in children, especially for Asian children [20]. Prevention and treatment in this field are promising, but more effort in research has to be put in place to reduce the incidence of this disease.

1.2. Eye and cornea

The eye is a globular structure, that allows living beings to see and interact with the outer world (Figure 1.1). It is characterized by a system of lens (the cornea and the crystalline), whose main function is to direct the light rays towards a point, called focal point, that, in an emmetrope normal eye, lies exactly onto the retina. The retina is the inner layer of the eye globe, responsible of transmitting the image information through the optical nerve directly to the brain.
Moving from the outer part to the inner part of the eye, the first lens that is encountered is the cornea, which is a transparent structure responsible of 2/3 of the total refractive power of the eye (i.e. the vision optical quality of the individual). In this thesis, the central focus will be the cornea, since the aim of this thesis is to modify its geometry to correct myopia by means of surgery.

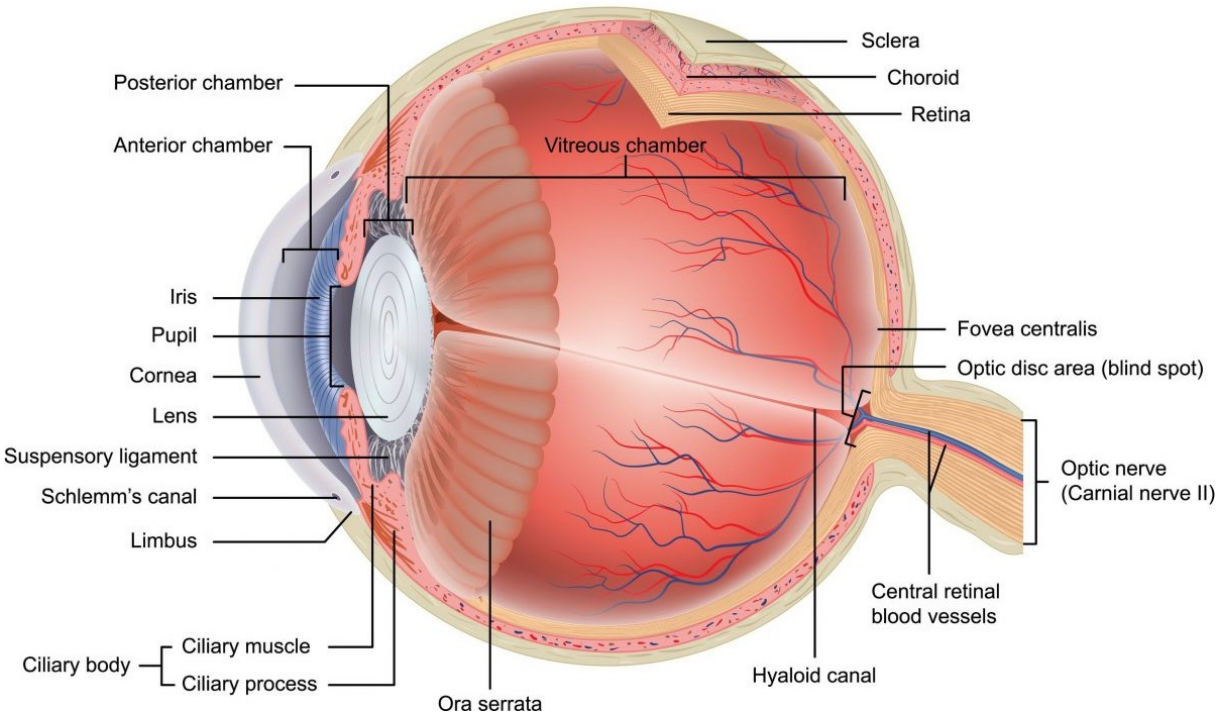

Figure 1.1: Eye anatomy [1].

1.2.1. Corneal anatomy and physiology

The cornea is an avascular tissue and it forms the highly transparent outer layer of the anterior eye. The cornea acts both as a structural barrier, protecting the eye against infections and injuries and as a refractive surface for the eye: together with the crystalline, ciliary muscles, retina, and optical nerve, the cornea contributes to the vision quality: 45

of the 60 dioptres of the optical power of a relaxed eye are provided by the cornea [31]. It creates a continuous stratum together with the opaque sclera, throughout a transitional zone: the limbus. It is itself composed of five layers: the epithelium, the anterior limiting membrane (i.e. the Browman's membrane), the stroma, the posterior limiting membrane (i.e. the Descemet's membrane) and the endothelium (Figure 1.2) [31] .

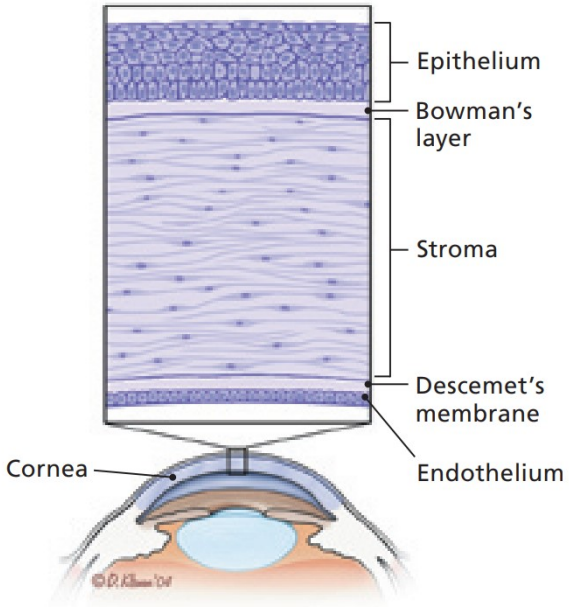

Figure 1.2: Diagram of the corneal structure in transverse section [49].

The corneal epithelium is a non-keratinised layer composed of five to seven cellular layers. Its functions are: physical protection of the deeper layers, refraction, radiation protection in the short ultraviolet wavelength and tear stabilization [31]. Furthermore, it has the function of uniforming the anterior surface and to improve the optical power of the cornea. The anterior limiting lamina (Bowman's membrane) is mostly acellular, formed by a dense layer of collagen I fibers. It is an anatomical landmark that demarkates the corneal limit. In radial keratotomy, a type of refractive surgery, the corneal incisions penetrate through the full thickness of the Browman's membrane and, due to its acellularity, it has been noted that the damage to this layer persists for several years after the surgery [26]. The corneal stroma provides rigidity, houses sensory nerve fibers, but most importantly is the site that mainly determines the biomechanical behaviour of the cornea, making up approximately the 90% of the total thickness of the cornea [39]. The main cell type of the stroma is represented by the keratocytes, which are able to synthesize collagen molecules, glycosaminoglycans, and matrix metalloproteinases (MMPs), contributing to stromal homeostasis. Most of the keratocytes reside in the anterior stroma. The stroma

is characteristically transparent which is the result of precise organization of stromal fibers and extracellular matrix (ECM). The collagen within corneal fibrils is mostly Type I. Moreover, parallel collagen fibers are grouped in fibrils, which are arranged, in turn, in 200-250 orthogonal layers called lamellae. Lamellar density within the stroma varies depending on their location: it is higher in the anterior portion than in the posterior. Furthermore, corneal collagen fibrils are narrower than in many other connective tissues of the body, a feature that provides the transparency of the tissue, being a function of the diameter (Figure 1.3) [41].

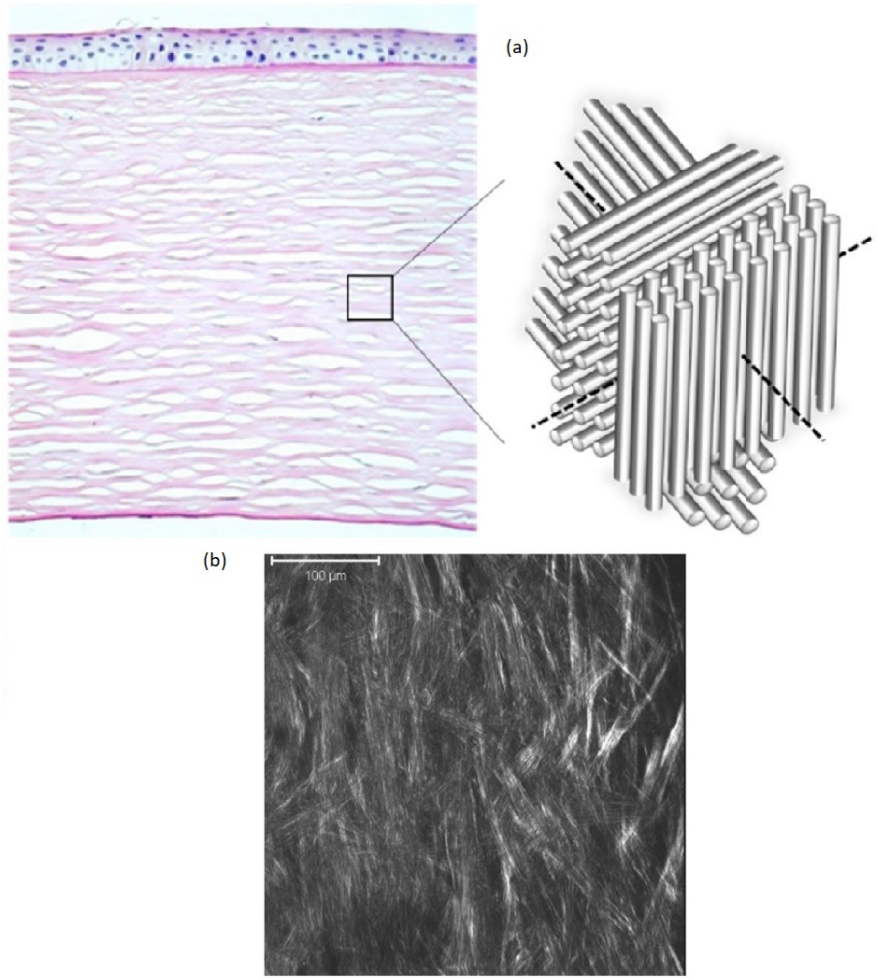

Figure 1.3: (a) Histological section of a human cornea showing the ultrastructure of the three main layers and illustration of orthogonally aligned collagen lamellae present in the human corneal stroma[18, 53] and (b) second harmonic generated (SHG) microscopy of face views from the front of the cornea [40].

More specifically, collagen fibers present a preferred orientation in corneal structure: they are oriented along with nasal-temporal (N-T) and inferior-superior (I-S) directions within

the central region of the human cornea and they start running circumferentially in the limbus region. Moreover, the fibers are more aligned along with N-T and I-S directions within the posterior thirds and are more isotropically oriented within the anterior thirds [44] (Figure 1.4).

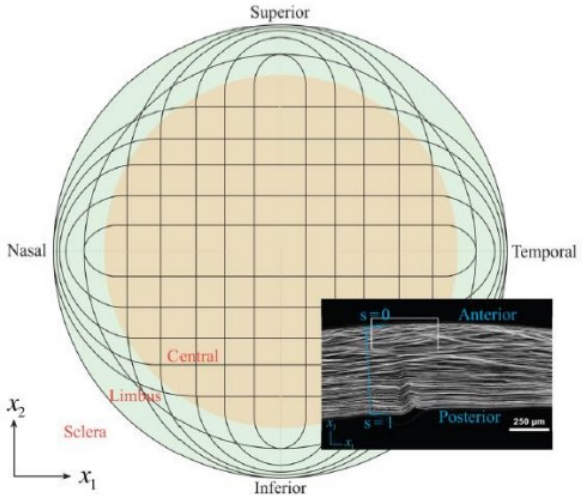

Figure 1.4: Collagen fibers orientation [53].

The posterior limiting lamina (Descemet's membrane) is the thickest basement membrane in the body and provides elasticity [31]. The corneal endothelium, which is of mesenchymal origin, is mostly a single cell layer; where it turns into a multilayerd trabecular meshwork, the beginning of the limbus is found [7]. The importance of the limbus lies in its main function of mediating the corneal epihtelial cells replacement and wound healing, housing the corneal epithelial stem cells [12].

1.3. Clinical diagnostics of the cornea

Whithin the main clinical tests, two main branches can be differentiated: imaging of the corneal surface and anterior segment (*Corneal Topography*), and measurement of dynamical and mechanical parameters of the corneal tissue (*Non-Contact Tonometry*). The Pentacam device (Figure 1.5) is a topography device that allows to investigate the anterior and posterior surfaces of the cornea, providing different types of maps. This is possible thanks to a rotating Scheimpflug camera, which provides an optical cross-sectional analysis [8]. Moreover, it supplies ulterior data such as corneal aberrometry and densitometry for ectasia detection and several indexes such as index of vertical asymmetry (IVA), which measures the corneal symmetry, or the surface variance (ISV), which is an

expression of corneal surface irregularity, an so on. The maps consist in elevation maps and pachymetric maps. The elevation maps are calculated as the difference between the actual corneal surface (anterior or posterior) and a standard reference shape, which is calculated to get the best fit to the measured cornea. The pachymetric maps are corneal thickness distribution maps identifying the true thinnest point (TP) and the CCT. Other data provided are the anterior and posterior surface radius, which will be useful to build an idealized conic model of the cornea (Chapter 2.1), while a more complete set of corneal parameters derived from Pentacam is used for a patient-specific analysis (Chapter 2.9).

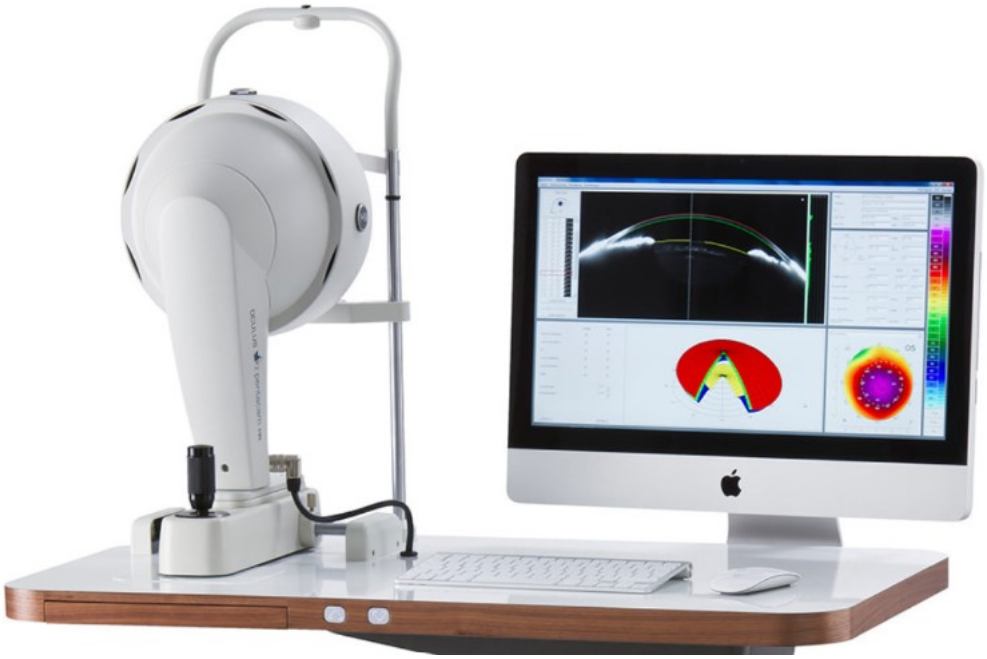

Figure 1.5: Pentacam device

To date, only two commercial systems aim at providing corneal biomechanical data: Ocular Response Analyzer (ORA, Reichert Ophtalmic Instrument) and the Corvis ST (Oculus, Wetzlar, Germany). The Corvis ST device, in particular, exploits a consistent air puff pressure to provide 2-dimesional imaging through a horizontal cross-section of the cornea. It is capable to isolate the corneal deflection from the whole eye-motion. This is possible thanks to the deformation parameters that are collected based on the dynamic inspection of the corneal response to the air puff pressure: the cornea begins to deflect in the backward direction and the whole eye motion follows this path in a slow linear increase at the beginning, until a dramatic increase when the cornea is at its maximum displacement. This test provides several parameters: in the deformation parameters, the

whole eye motion is not compensated, while in the deflection parameters the displacement is taken into account [14] (Figure 1.6).

Figure 1.6: Corcis ST device.

1.4. Average corneal dimensions

Corneal geometry can be assessed by using mainly three parameters, measured by high accuracy devices such as optical coherence tomography (OCT), or corneal topographers (Sirius or Pentacam) (Chapter 1.3): radius of curvature, corneal thickness and corneal diameter. These data are fundamental to evaluate the refractive power of the cornea. The posterior surface is more spherical than the anterior surface. The mean posterior curvature (PCC) is (6.53 ± 0.25) mm, with a range from 5.62 to 7.22 mm, while the mean anterior corneal curvature (ACC) is small, gradually flattening in the periphery, with an average apical radius of curvature of (7.79 ± 0.27) mm [34]. The anterior corneal stromal rigidity is particularly relevant when talking of maintaining the corneal curvature [30]. The thickness of the cornea represents the distance between the anterior surface and the posterior surface. The thickness is not constant over the whole radius of curvature, rather it increases from a central corneal thickness (CCT) of (552.6 ± 34.5) µm to a peripheral thickness of (612.5 ± 35.3) µm [16]. However, corneal dimensions depend on different factors such as the gender or age of the subject considered [17].

1.5. Corneal Biomechanics

The cornea microstructure is tightly regulated by the body's mechanisms and is extremely complex: after death, optical clarity is lost and tissue degradation occurs: all the ex-vivo

studies will be affected by these factors, which will change the biomechanical properties of the cornea. Moreover, the corneas available for research purposes, are the ones not suitable for transplantation, being affected, for example, by ocular disease, positive serology or stored for too long, thus making the mechanical characterization difficult [25]. Furthermore, the corneal tissue biomechanics provides the corneal stability throughout its structural features, which allow to preserve its conic geometry despite the presence of an intraocular pressure (IOP). As said in Chapter 1.2.1, the stroma is the most important layer of the cornea when talking about the mechanical properties. The ECM in the stroma shows a nearly incompressible behaviour, due to its high water content. One of the experimental ways to determine mechanical properties of the corneal tissue is throughout the inflation test, which is carried on specifically to mimic the intraocular pression (IOP), the fluid pressure of the eye, exerted by the acqueous humor on the internal surface of the anterior eye. In physiological conditions, the IOP ranges between 10 mmHg and 20 mmHg, with an average value of (14.7 $\pm$ 2.8) mmHg [55]. The IOP is crucial in the optical behaviour of the structure, having a great impact on the topography of the cornea: excessively high values of IOP lead to pathological conditions such as glaucoma [48]. In the inflation tests carried on by Ahmed Elsheikh et al.[13], the cornea samples were mounted on a pressure chamber, filled with saline solution and subjected to a pressure rate of 37.5 mmHg/min. The results showed that, within the intraocular pressure level (under 15-20 mmHg), corneas demonstrated low stiffness and hyper-elastic behaviour (Figure 1.7 (a)). Thus, the cornea is a hyperelastic tissue, presenting an initial linear behaviour and then a non linear one: the model by Wang et al. [53] will be further applyed in Chapter 2.3 (Figure 1.7 (b))

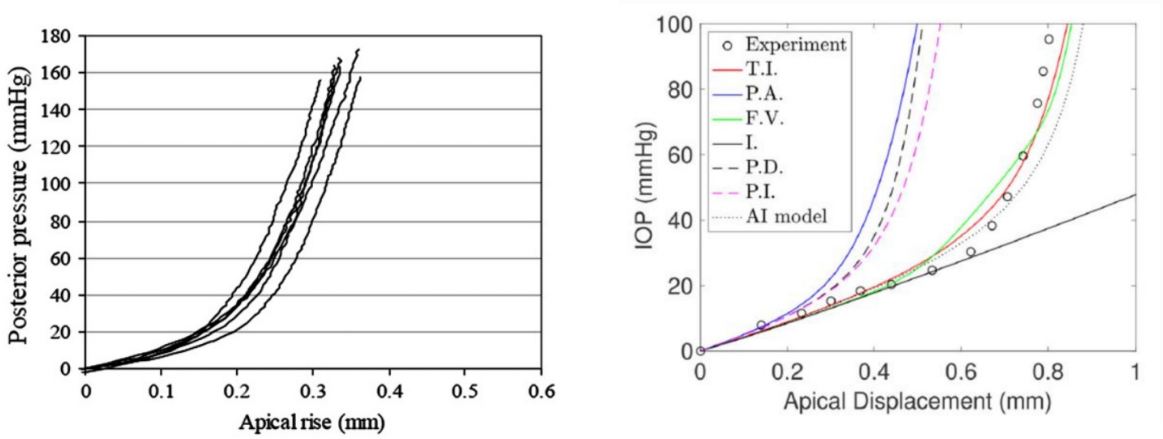

(a) (b)

Figure 1.7: (a) Pressure deformation results of six human corneas with 65-79 years of age presented as examples of human corneal behaviour under inflation test [13] (b) Apical rise–pressure curves: the comparison between experimental data (throughout the inflation test) and six different numerical cases of Wang and Hatami work [53]..

For these reasons, the cornea's elastic modulus is not constant, but varies in function of strain. It ranges between 1.3 MPa and 5 MPa [28]. It is important to know that, due to the crucial stiffness provided by the fibers, the degree of anisotropy is significant. The distribution and orientation of the fibers greatly influences the mechanical behaviour, which is also susceptible to local variations. More specifically, an approach in quantifying the degree of anisotropy is provided by uniaxial tests, which allow to calculate the stress-strain relationship in a single direction. In Figure 1.8, the force-time and stress-strain response of cornea samples are reported, considering a loading rate of 10 mm/min: in the early stage the displacement increases, while the reaction force does not increase significantly, but the response is exponential when higher displacement and tension are applied on the tissue [36].

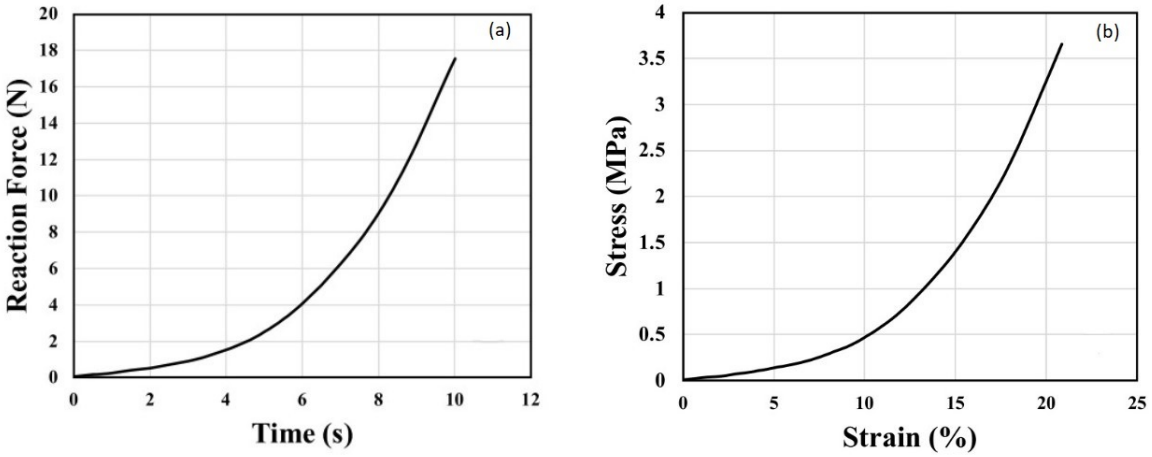

Figure 1.8: Force-time graph (a) and Strain-stress curve (b) of the uniaxial-tensile test [36].

1.6. Optics

The cornea, along with the lens, represents the refractive apparatus of the eye. The optical properties of a refractive surface depend on the ray of curvature and on the refraction index of the means it's composed of. In fact, the corneal tissue has a higher optical density than the air, meaning that a portion of the incident light rays changes its direction, leading to the refractive phenomenon (Figure 1.9).

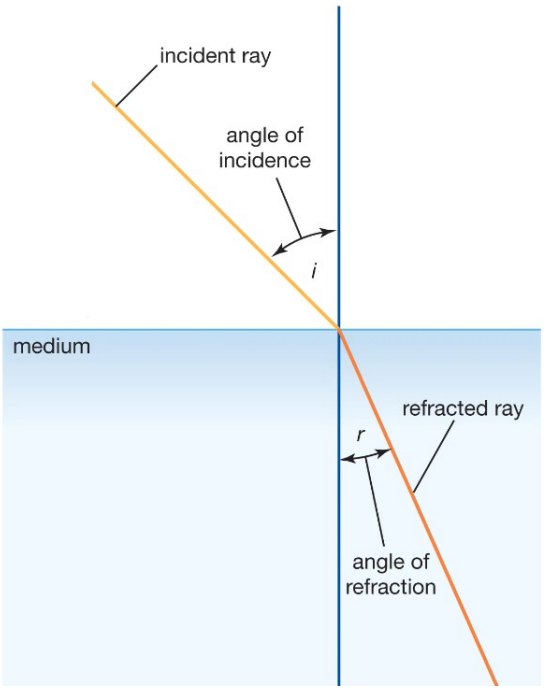

Figure 1.9: The phenomenon of refraction of light [2].

The ratio between the incidence angle (i) and the refractive angle (r) (respect to the perpendicular surface of the incidence surface) is called refractive index (Equation 1.1).

$$n = \frac{\sin(i)}{\sin(r)} \tag{1.1}$$

The refractive index depends on the density of the materials through which the light rays are propagating [11]. Moreover, the optical system features are highly dependent on the surfaces and their corresponding distance. The unit of measurement of the refractive power is the dioptre (D), which is the reciprocal of the focal length f (e.g. the distance at which parallel rays of light coming from an object at infinity will converge after passing through the lens), expressed in metres (Equation 1.2).

$$D = \frac{1}{f}[m^{-1}] \tag{1.2}$$

The total refractive power of the eye is 59 [D], with about two-thirds provided by the anterior surface of the cornea alone. This is due to the refractive index of the cornea, which is much higher than that of air ($n_{cornea} = 1.3775$, $n_{air} = 1$). On the contrast, the refractive index of the eye lens is not greatly different from the indices of the aqueous

humour and vitreous humour, providing a minor contribution to the refractive power of the cornea. (Figure1.10) [19].

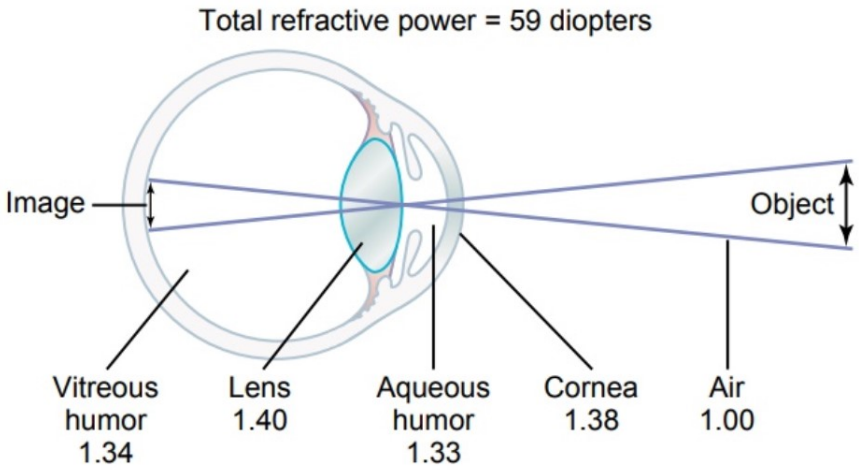

Figure 1.10: The refractive indexes of the eye [19].

1.7. Refractive Disorders

A relaxed, healthy eye, produces the image of an object at infinity on its focal plane at 24 mm behind the vertex of the cornea. If the retina lays on this plane, the image formed is sharp and the conditions for a distinct view are satisfied. The correspondence between the focal length of the optical component of the eye with the one of its axis is called emmetropy (Figure 1.11 (a)). The capability to see distinctly and clearly is highly dependent on this factor, as well as on the integrity of the photochemical and neurophysiological states of the visual process. The missing correspondence between the focal length of the eye optics with the optical axis leads to the refractive disorders, which are myopia, hyperopia and astigmatism [11].

1.7.1. Myopia

Myopia is a condition in which the image of a far object doesn't project to the retinal plate, but in front of it. This occurs because the myopic eye presents a too strong optical power (which means a lower focal length) than the emmetropic or, more commonly, the axial length of the eye is excessive (Figure 1.11 (b)). This leads to bad vision of objects that are far away, but does not influence near objects vision. Myopia may be categorised by the degree of refractive error: low myopia is present for diptric values equal or less than -3 D, moderate myopia ranges from -3 D to -6 D, and high myopia usually is characterized

by -6 D or more [11].

1.7.2. Hyperopia

When the axial length of an eye is too short if compared to its focal length, the retinal plate intercepts the light rays before they become in focus (Figure 1.11 (c)). In this case the eye is considered hyperopic [11]. A hyperopic person sees more clearly distant objects than near objects.

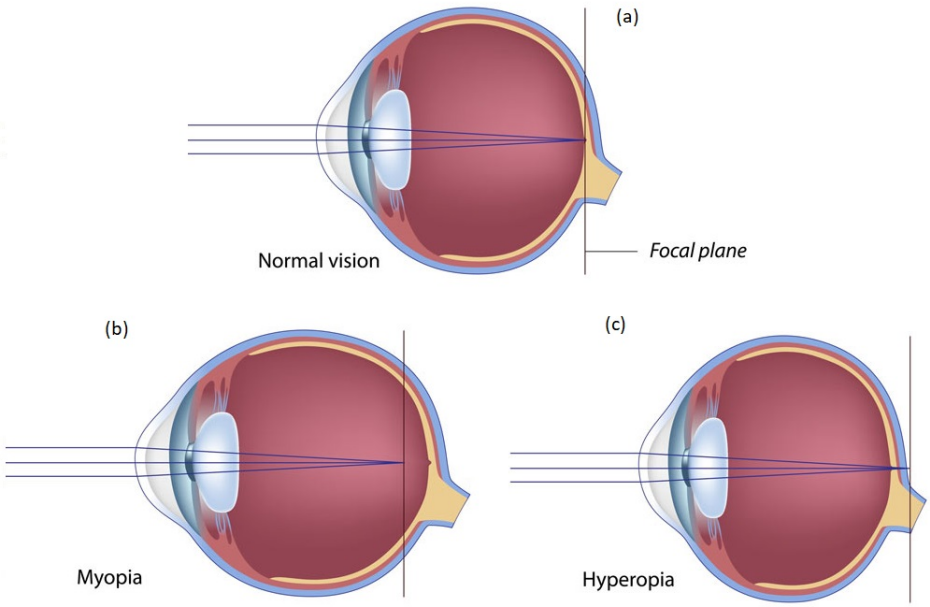

Figure 1.11: Images formation on the retina. (a) Emmetropy: the object of vision projects directly on the retinal plate. (b) In a myopic eye, the image projects in front of the retinal plate. (c) In a hyperopic eye, the image projects behind the retinal plate [45].

1.7.3. Astigmatism

As a first approximation, the existence of two symmetry axes can be hypotesized: an antero-posterior symmetry axis (or horizontal meridian) in correspondence of the optical axis (e.g. the line in which the centers of curvatures of the dioptric surfaces are found) and a vertical meridian, that divides the eye in the nasal and the temporal portions. An important optical anomaly occurs when the the curvature of an optical surface is not the same in all the meridians. For example a cornea can have an higher curvature on the vertical meridian rather than the horizontal one, leading to an higher refraction on the vertical meridian: in this case a point-like object won't project to a point-like image, but to a conoid-like one (Figure 1.12). This condition is called astigmatism [11] and is

chacterized by vision distortion, as light rays are prevented from meeting at a common focus, at every distance the object of interest is found.

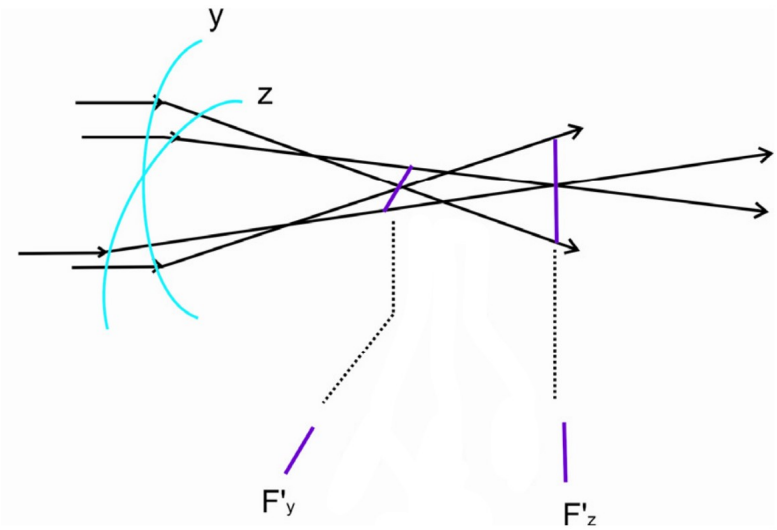

Figure 1.12: Plots showing image formation in an eye with an astigmatic refractive error. The principal meridians (y, z) and the first and second focal lines (F'y, F'z) are shown [35].

1.8. Vision impairments correction

1.8.1. Vision aids

The vision aids used to correct hyperopia, myopia and astigmatism are spectacles and contact lenses. The lenses modify the convergence of the light rays: myopic eyes are corrected employing concave lenses, which increase the focal length, while for hyperopic eyes, convex lenses are used, to give the eye more dioptric power by reducing the focal length (Figure 1.13); the astigmatism is corrected by lenses with different bending radii along the meridians. In spite of their widespread use, both spectacles and contact lenses present some disadvantages: increased light scatter, image magnification or minification, discomfort and inconvenience are some of the issues with glasses, while contact lenses may irritate the ocular surface with increased risk of corneal scratches and infections [4].

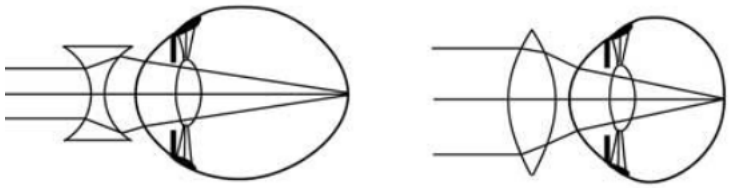

Figure 1.13: Correction of vision defects through concave and convex lenses.

1.8.2. Corneal refractive surgeries

The effort in surgery has been concentrating on changing the corneal focus power, being the cornea accessible for surgery and accounting most of the optical power of the eye. The modern refractive surgery pioneer was Barraquer, who invented keratomileusis over 50 years ago. It consisted on removing an intrastromal tissue layer using a microkeratome, a surgical instrument designed to excide the tissue [23]. In the early 1980s, laser refractive surgery was introduced. At first, the excimer laser was employed: it consists of an ultraviolet laser combining a noble gas (Argon) with a reactive halogen gas (Fluoride), emitting photons at a wavelength of 193 nm, which leads to collagen ablative photodecomposition, (e.g. peptides backbone is broken and corneal collagen is vaporized). This laser has low tissue penetration while preserving high corneal absorption, which means that it can ablate the cornea without causing heating or damage to the adjacent tissue, thanks to the short pulse duration [4]. In 2001, Femtosecond (FSL) laser was introduced: it operates at near-infrared wavelengths, currently at a frequence of 500kHz and uses ultra-fast focused pulses, generating a flow of free electrons and ions that constitutes the plasma state. This causes the so called laser-induced optical breakdown, that leads to the formation of a cut in the focal volume of the laser beam, with minimum collateral damage [46].
Corneal refractive surgeries have a great success rate, limited discomfort in the first days right after the surgery, limited risk of infection and no need to use other vision aids for the rest of life. On the other hand, they have an high cost (a small lenticule extraction surgery (SMILE) (Chapter 1.8.2.3) is about 2400 EUR per eye), and they can lead to condition of dry eye, a rather common condition that occurs after photorefractive keratectomy (PRK) (Chapter 1.8.2.1) or laser in-situ keratomileusis (LASIK) (Chapter 1.8.2.2), due to damage to the corneal afferent nerves that interrupts sensory input into the ocular surface lacrimal gland feedback system. However, dry eye is a transient condition that can last from a few weeks up to 1 year [9].

1.8.2.1. Photorefractive keratectomy (PRK)

PRK is the most popular method for correction of myopia or hyperopia, with or without astigmatism. It consist of two steps: the first is the central corneal epithelium removal and the second is the superficial excimer laser ablation (Figure1.15 (a)). For refractive purposes, the cornea can be reshaped to correct myopia, hyperopia, and astigmatism. For myopia treatment, the aim of the surgery is to lower the curvature of the centre of the cornea to create an oblate shape, which makes the focal length higher, focusing the image at the right distance, right on the retinal plate. The ablation profile for the correction of hyperopia, instead, flattens the periphery of a defined optical zone and effectively steepens the central visual axis (Figure 1.14).

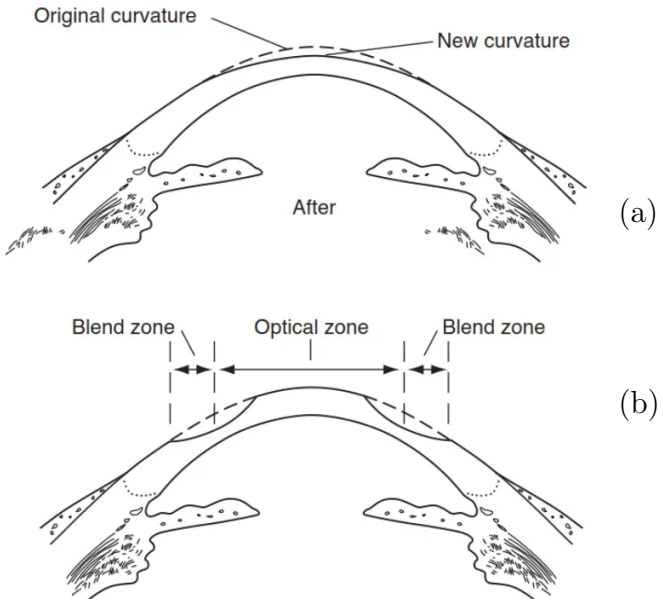

Figure 1.14: Corneal reshaping in (a) correction of myopia and (b) correction of hyperopia. [37].

This procedure has a low to moderately high range of correction (up to -6 D), 3 to 7 days of vision recovery and is more indicated for thin corneas, where the residual stromal bed (RSB) would be less than 250-300 µm. The contraindications would be pain intolerance, predisposition to haze formation, requirement of rapid visual recovery [29].

1.8.2.2. Laser-assisted in situ keratomileusis (LASIK)

While photorefractive keratectomy (PRK) is an effective refractive procedure for appropriate candidates, it does not offer the convenience of the rapid visual rehabilitation of

LASIK. In LASIK the creation of a thin corneal flap (with the aid of a blade or a laser beam) is followed by the excimer laser application on the underlying corneal tissue and the repositioning of the flap in its original place (Figure1.15 (b)). Most refractive surgeons require at least between 480 and 500 µm of central corneal thickness (CCT) to consider LASIK, in order to to leave between 250-325 µm of RSB, to preserve corneal mechanical strength. This is because the flap and the ablation require more thickness than the superficial ablation alone (PRK). The range of correction (up to -6 D) is limited by the residual corneal thickness, while wound healing, post-operative pain and time recovery are minimal. On the other hand, specific complications are strictly connected to the flap: flap wrinkles, epithelial ingrowth, corneal ectasia and flap melt [29].

1.8.2.3. Small incision lenticule extraction (SMILE)

SMILE is an all-in one femtosecond laser-assisted keyhole surgery to correct myopia and astigmatism. Unlike LASIK, SMILE does not require the creation of a hinged flap and excimer laser stromal ablation, but, instead, an intrastromal lenticule is outlined, basing on the refractive corrections desired, and subsequently extracted through a keyhole incision (Figure1.15 (c)). SMILE shows good corneal wound healing and inflammatory responses, better biomechanical stability, less subbasal nerve damage, and faster corneal sensation recovery than LASIK. Since SMILE surgery minimises the impact on the anterior corneal surface, better redistribution of strain compared to LASIK and PRK can be assumed, thus improving postoperative outcome and healing process. Furthermore, SMILE keeps the Bowman's membranes intact, which come with additional advantages for corneal biomechanics over other techniques. In fact, in the case of recisions, corneal mechanical properties decrease, due to lower cohesive tensile strength [51]. Clinically, SMILE has been shown to produce excellent safety, efficacy, predictability and stability, and the refractive outcome is comparable to LASIK [22]. Preservation and reimplantation of the refractive lenticule has rendered SMILE to be reversible, providing an opportunity for further refractive surgery. Reinstein et al.[47] have developed a mathematical model that calculates the total corneal tensile strength after LASIK and SMILE. The model has revealed that in a 550 µm-thick cornea, the total tensile strength post-SMILE (with 130 µm thick cap) would be 75% and post-LASIK (with 110 µm-thick flap) would be 54% after 100 µm tissue removal. This finding suggests that the thickness of the SMILE lenticule could be 100 µm greater than the LASIK ablation depth and the post-SMILE cornea would still have equivalent tensile strength as the post-LASIK cornea, which translates to an additional -7.75 D myopic correction in SMILE [29].

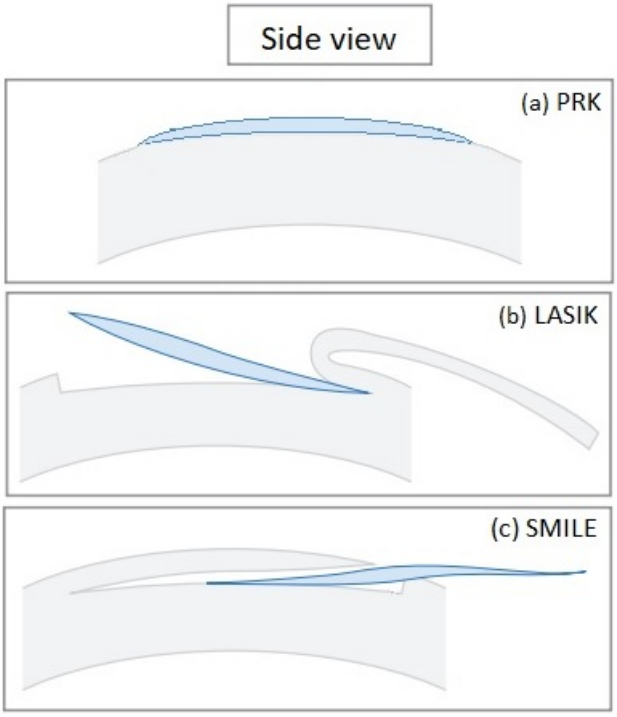

Figure 1.15: Side view of lenticule removal (the blue portion is the one to be removed in order to lower the cornea superficial curvature for myopia treatment) in (a) PRK surgery, (b) LASIK surgery, (c) SMILE surgery.

1.8.3. Surgery Complications

Refractive surgery contraindications include infections, autoimmune conditions, medications and abnormal corneal anatomy. Being the effective thickness of the cornea reduced, a change in the biomechanics of the structure occurs and, in a small percentage of patients, it results in significant loss of biomechanical integrity, which can lead to severe patologies. The main concerns about refractive surgeries, in particular regarding LASIK and PRK, are ectasia and keratoconus development. Corneal ectasia is one of the rare yet potentially devastating complications encountered after refractive surgery. It consists in a progressive increase in myopia, with or without increasing astigmatism, with keratometric steepening of the cornea and topographic asymmetric inferior corneal steepening. Over time, thinning of the central and paracentral ectatic cornea occur [54].
Keratoconus is a bilateral, asymmetrical, non-inflammatory, progressive thinning disease of the cornea. It involves a protrusion of the cornea, with a central or infero-central apex (Figure 1.16). The biomechanical properties of keratoconic corneas are different from those of normal corneas. As the disease progresses, myopia increases and image quality is further reduced by higher-order ocular aberrations. The exact patho-genesis of

keratoconus is not clear but it is believed that the thinning and the bio-chemical stress, expecially on the corneal posterior surface induced by laser surgery triggers further biomechanical weakening of a pathologic cornea [43]: posterior corneal changes are essential to keratoconus diagnosis [6].

Figure 1.16: Picture of a keratoconic eye.

Even though the posterior surface brings a minimal contribution to the refractive power of the eye, having a minimal difference in terms of refraction index between the cornea and the acqueous, it is recognized to be the earliest indicator of ectatic disease and predates the changes in mechanical properties of anterior corneal surface [6].

1.9. Aim of the thesis

The overall objective of this thesis is to develop a numerical methodology to simulate, by means of finite elements method, two refractive surgeries: PRK and SMILE. In order to achieve this aim, the following procedures have been carried out:

- Construction of different average geometrical models of the cornea using the conic approximation (to correct myopia only), to perform several analysis on the geometrical, mechanical and optical parameters, that could influence the optomechanical behavior.
- Optimization of the SMILE simulation by analyzing the mechanical and optical impact of lenticule positioning in the corneal thickness in SMILE surgery.
- Analysis of the impact of the boundary conditions on the two corneal surgery models (PRK and SMILE) from an optomechanical point of view.
- Analysis of the optomechanical performance and accuracy of the two models by

varying the dioptric correction goal.

- Analysis of the influence of the central corneal thickness on the optomechanical outcome.
- Mechanical sensitivity analysis by means of a 2^5 full factorial design.
- Montecarlo analysis of the influence of the material on the achieved dioptric correction with respect to the target.
- Comparison of the optical correction obtained with Munnerlyn's theoretical profiles [42] with those currently performed by commercial lasers, by means of a geometry based on clinal procedure data.
- Construction of a patient-specific model.
- Validation of the proposed methodology to simulate PRK surgery and SMILE surgery, by reproducing the surgery performed on a patient. In this case, the pre- and post-surgery geometries and the ablation profile are provided by the Barraquer clinic.
- Compare the two surgeries simulations from an opto-mechanical point of view.

2 | Materials and Methods

This chapter describes the materials and methods used to simulate laser refractive surgeries for myopia correction with finite element models. A conical model of the cornea was built, to analyse the influence of different geometrical, mechanical and optical parameters, such as central corneal thickness, lenticule position and radius, desired dioptric correction and material properties. Subsequently, the study has been completed with patient-specific models through reproducing SMILE and PRK surgeries of one real patient.

2.1. Geometry of the Cornea

The refractive power of the cornea is strictly connected to its geometry and, in order to analyze the performance of the numerical simulation, pre- and post-surgical corneal shape should be taken into account.
Modern ophthalmologic instruments (corneal topographers and pachymeters) acquire the shape of the anterior and posterior surfaces and of the thickness of the cornea at a very high resolution, generally in terms of coordinates of point clouds. In this thesis, the corneal geometry was reconstructed by using a conic model (Equation 2.1), starting from patient-specific data derived from a Pentacam topography (Figure 2.1) of a healthy patient. The corneal thickness, in particular, was set as 579 µm (being the patient's Pentacam datum, named "$Paqui\ Vertice$").

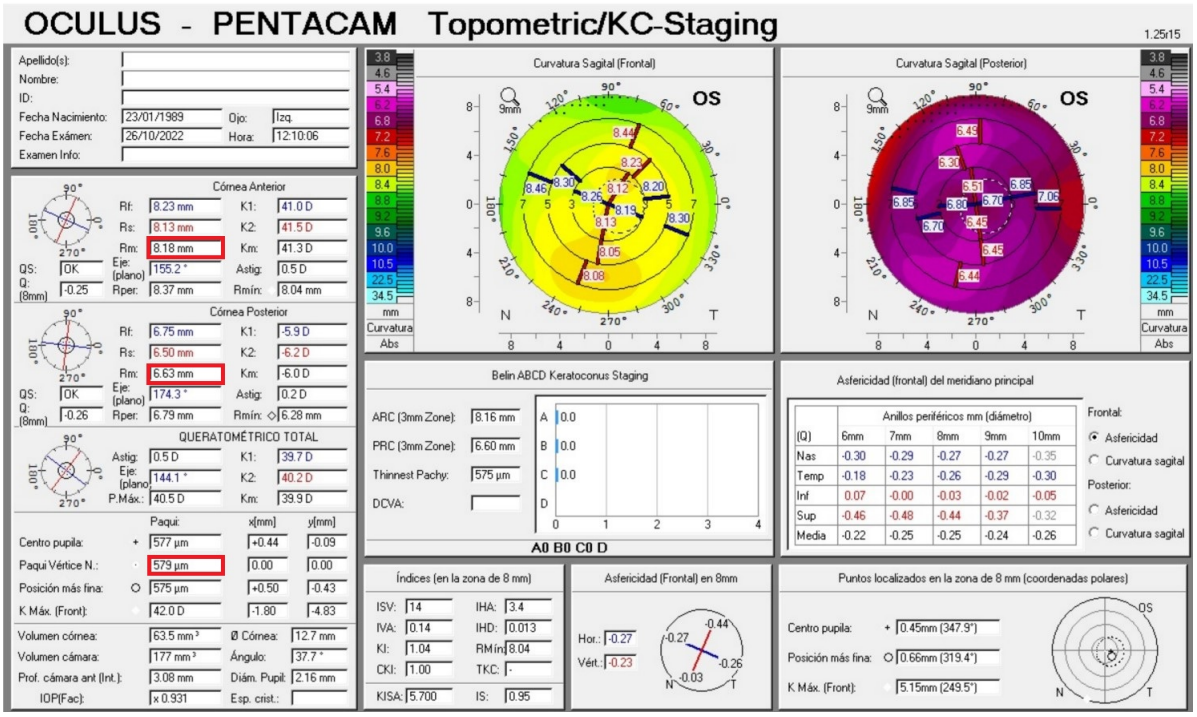

Figure 2.1: Pentacam topography of a healthy patient, used to build the geometry model by a conic approximation (the data employed to build the model are highlighted in red).

2.1.1. Conic Model

The first hypothesis assumed in this thesis is that corneal shape can be represented through a conic model, that is a rotationally symmetric solid and described by the conic Equation (2.1) [32].

$$y^2 = 2(r_0)z - (1+Q)z^2 \tag{2.1}$$

where r_0 is the apical radius and Q is the asphericity parameter, which represents the deviation of the conic from a circle. In this case, mean values of r_0 and Q were derived from the topography of Figure 2.1: the mean anterior and posterior apical radii, respectively $R_{m_{anterior}} = 8.18$ mm and $R_{m_{posterior}} = 6.63$ mm. Once the conic section is obtained (Figure 2.2), it has to be rotated around the z-axis, in order to obtain the 3D conic model. This geometry could be used to study myopia and hyperopia defects, but is not suitable for the study of astigmatism, given its rotational symmetry, that does not allow to account for different curvatures on different meridians. At the presence of astigmatic defect, it is necessary to use biconic or patient specific models, as will be seen in Chapter 2.9, since the conic model is not able to capture patient's corneal features properly.

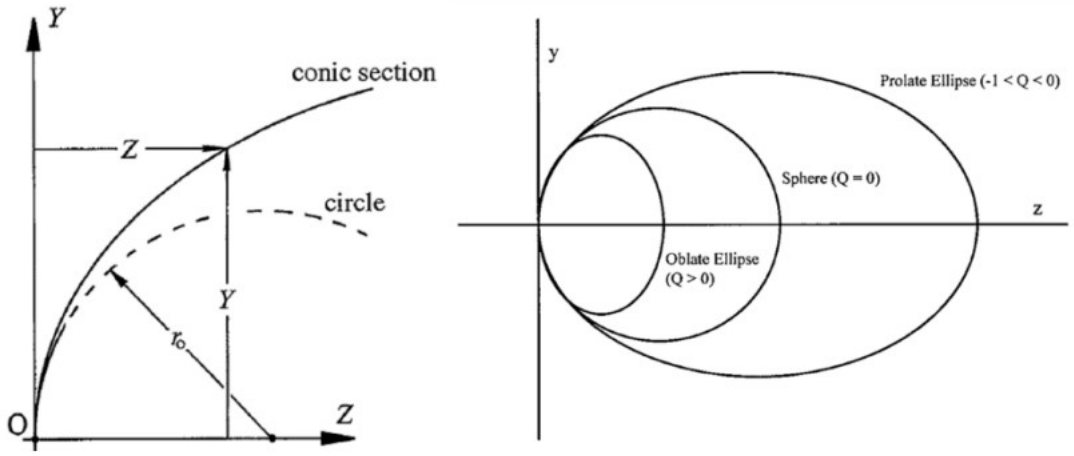

Figure 2.2: Conic section and asphericity changes [32].

2.1.2. Ablation Profile

Given the topography of a healthy patient, the refractive defect was assumed to be caused by a higher axial length with respect to an emmetrope eye and not by an anomalous corneal shape. The simulations were intended to correct from -4 D to -8 D. A conic ablation profile was build, using Equation (2.1), where the apical radius was obtained from the equation for thin lenses (Equation 2.2), while the ablation asphericity value was obtained applying the Equation (2.3), where t_0 is the corneal thickness, n is the index of refraction and D is the number of dioptres to be corrected [24].

$$R_{\text{ablation}} = \left(\frac{D}{(n-1)} \cdot \frac{1}{t_0} \right)^{-1} \tag{2.2}$$

$$Q_{\text{ablation}} = \frac{R_{\text{ablation}}^3}{t_0^3} \cdot (1+Q) - 1 \tag{2.3}$$

In order to build the right ablation volume, the optical zone (OZ) of interest, that is the area where the laser acts during the surgery, was set with a radius $R_{\text{oz}} = 3$ mm and further changed to investigate its influence on the surgery model outcomes. In order to place correctly the ablation profile, the same criterion as the one used by Manns et al. [38] was followed. This criteria proposes the same ablation profile for both surgeries: moving from the corneal apex, the ablation profile was moved down until the distance between the edge of the ablation and the edge of the OZ was null. In this way, the ablation depth was determined. The theoretical ablation depths are reported in Table 2.1, which were used for both for SMILE and PRK models, when different desired dioptric corrections where set. Moreover, the ablation depth can change depending on the OZ radius variation,

according to the Manns et al. model [38] (Table 2.2).

Desired dioptric correction [D]	Ablation Depth [µm]
-4	47.6
-5	59.6
-6	71.4
-7	83.3
-8	95.2

Table 2.1: Ablation depths in PRK and SMILE models varying the desired dioptric correction parameter (with an OZ of radius = 3 mm).

OZ Radius (mm)	Ablation Depth [µm]
3	47.6
3.5	64.7
4	84.3

Table 2.2: Ablation depths in PRK and SMILE models varying the OZ radius parameter (with a desired dioptric correction of -4 D).

2.2. FE Model

The conic geometry was obtained by building the anterior, posterior, thickness and ablation surfaces point clouds (Figure 2.3) derived from the Pentacam data, as an average idealized geometry. All the algorithms for surface creations were developed in MATLAB 2023a. The same geometry was used for all the simulations presented in the thesis, except for the patient-specific models (see Section 2.9).

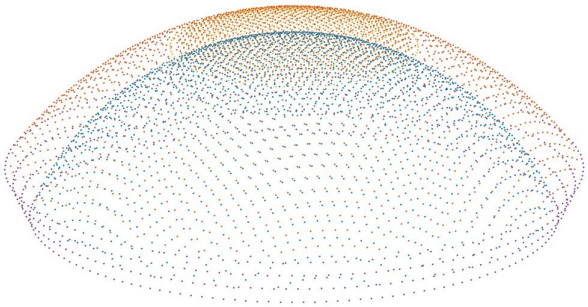

Figure 2.3: Three-dimensional geometry of the cornea defined by a conic model point cloud on MATLAB 2023a: a more dense anterior part corresponds to the OZ, both for PRK and SMILE.

Subsequently, the models were meshed with quadratic tetrahedrons, using the software ANSA pre-processor by BETA-CAE systems v22.0.1 (Figure 2.4). The use of tetrahedrons instead of hexahedrons was due to the presence of the ablation profile: the presence of edges at the extremities of the profile does not allow to use hexahedrons, which would provide, nevertheless, a more precise FE result. The choice of using quadratic elements instead of linear, was due not only to have higher accuracy of the results, but also because the phenomenon of the shear locking (i.e. in which the curvature is not accurately modeled under bending, and a shear stress is introduced) was appearing when using linear elements in the corneal model.

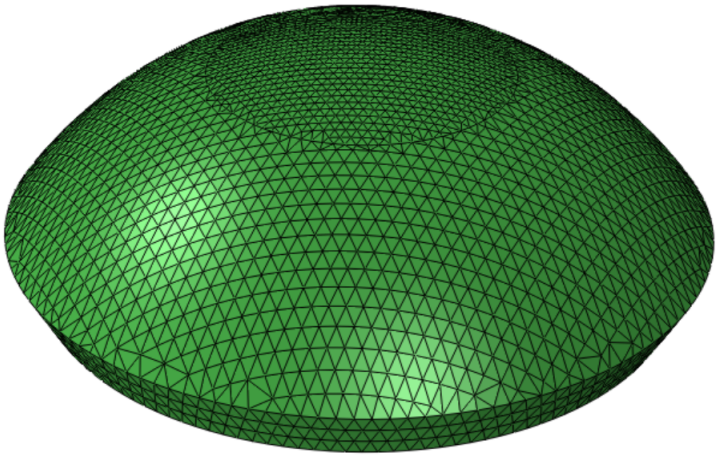

Figure 2.4: Mesh of the corneal model: quadratic tetrahedric elements from ABAQUS 6.13.

2.3. Material model

As said in section 1.2.1, collagen fibers present a preferred orientation in corneal structure: they are oriented along with nasal-temporal (N-T) and inferior-superior (I-S) directions within the central region of the human cornea and they start running circumferentially in the limbus region. Furthermore, in-plane and out-of-plane dispersions must be considered: these two parameters describe the probability of distribution of the fibers in the space. The degree of in-plane dispersion varies in depth, meaning that the fibers are more aligned along with N-T and I-S directions within the posterior thirds and are more isotropically oriented within the anterior thirds. The following strain energy density function has been considered for a nearly-incompressible material:

$$\psi = \psi(J) + \psi^{\text{matrix}}(\bar{I}_1) + \sum_{i=4}^{6} \psi^{\text{fibers}}(\mathbf{C}_{\text{dis}}, \mathbf{H_i}) \tag{2.4}$$

where $\psi(J)$ is the volumetric term, $\psi^{\text{matrix}}(I_1)$ represents the isotropic contribution, and $\psi^{\text{fibers}}(\mathbf{C}_{\text{dis}}, \mathbf{H_i})$ accounts for the fibers of the model. The volumetric term associated with the incompressibility of the material is:

$$\psi(J) = \frac{1}{D}(\ln J)^2 \tag{2.5}$$

A Neo-Hookean model was chosen to describe the behavior of the matrix component of the tissue:

$$\psi^{\text{matrix}}(\bar{I}_1) = C_{10}(\bar{I}_1 - 3) \tag{2.6}$$

where C_{10} is a stress-like parameter, which controls the isotropic component of the corneal matrix where the collagen fibers are found. To model the anisotropic behaviour of the collagen fibers, the hyperelastic Holzapfel-Gasser-Odgen model with dispersion parameters was used [44, 53]: let $\mathrm{x_R}$ represent an arbitrary material point in the reference configuration of the body, which undergoes a motion χ=($\mathrm{x_R}$,t) to the deformed body, with the deformation gradient defined as (Equation 2.7)

$$F = \nabla\chi \tag{2.7}$$

where J= det(F) > 0. The right and left Cauchy–Green tensors are given by $\mathbf{C}$= $\mathbf{F^T F}$ and $\mathbf{B}$= $\mathbf{F F^T}$, respectively. The distortional part of the deformation gradient is $\mathbf{F_{dis}}$=$J^{1/3}\mathbf{F}$ and det($\mathbf{F_{dis}}$)=1. The distortional right and left Cauchy–Green deformation tensors are $\mathbf{C_{dis}}$= $\mathbf{F^T}_{\mathbf{dis}}\mathbf{F}$ and $\mathbf{B_{dis}}$= $\mathbf{F F^T}_{\mathbf{dis}}$. There are two families of collagen fibrils in the corneal stroma and their mean referential directions are denoted by unit vectors $\mathbf{a^0}_{\mathbf{4}}$ and $\mathbf{a^0}_{\mathbf{6}}$. The unit vector $\boldsymbol{a_n}$, normal to the plane spanning by $\mathbf{a^0}_{\mathbf{4}}$ and $\mathbf{a^0}_{\mathbf{6}}$, to identify the out-of-plane direction. The invariants $\bar{I}_1$,$\bar{I}_4$, $\bar{I}_6$,$\bar{I}_{\mathrm{n}}$ are written as:

$$\bar{I}_1 = \mathrm{tr}(\mathbf{C}_{\text{dis}}) \tag{2.8}$$

$$\bar{I}_i = \mathbf{C}_{\text{dis}} : \mathbf{a}_0^i \otimes \mathbf{a}_0^i \tag{2.9}$$

for $i = 4, 6$, where

$$\bar{I}_1^* = \mathrm{tr}(\mathbf{H_i C}_{\text{dis}}) = 2k_{\text{ip}}k_{\text{op}}\bar{I}_1 + 2k_{\text{op}}(1 - 2k_{\text{ip}})\bar{I}_i + (1 - 6k_{\text{ip}}k_{\text{op}} - 2k_{\text{op}}(1 - 2k_{\text{ip}}))\bar{I}_n \tag{2.10}$$

$$\psi^f = \frac{k_1}{2k_2}\left(e^{k_2(\bar{I}_i^* - 1)^2} - 1\right) \tag{2.11}$$

k_{ip} and k_{op} are in-plane and out of-plane dispersion parameters [53], k_1 is a stress-like parameter, which controls the fibers' stiffness; k_2 is a dimensionless parameter, which governs the non-linearity of the corneal material behaviour in the stress-strain curve, due to the fibers presence.
The material parameters, according to Wang and Hatami [53], who optimized these values through inflation tests on human corneas, are shown in Table 2.3:

C_{10} [kPa]	k_1 [kPa]	k_2 [-]	D [kPa^{-1}]
30	20	400	$3.6e^{-04}$

Table 2.3: Material parameters used in the surgery simulations.

Regarding the dispersion parameters, the following equations were considered:

$$k_{ip}(\theta, r) = k_{ip}^{min} + \frac{1}{2}(k_{ip}(\theta) - k_{ip}^{min})(1 - \cos(2\pi r/R_{TZ})) \tag{2.12}$$

$$k_{op}(s) = k_{op}^{min} + (k_{op}^{max} - k_{op}^{min})(1 - \exp(-\gamma_d s)) \tag{2.13}$$

where:

- k_{ip} is the in-plane dispersion $\in [0.1, 0.5]$
- k_{op} is the out-of-plane dispersion $\in [\frac{1}{3}, 0.5]$
- R_{TZ} is the radius of transition zone (=5.5 mm) from cornea to limbus
- γ_d is the non-linearity function constant
- s is the local coordinate of the thickness $\in [0, 1]$

The material model was implemented through a User Material (UMAT) in Fortran language. Moreover, the theoretical fibers' orientation is modified by dispersion parameters. Using the PARAVIEW software, the fibers orientation can be visualized (Figure 2.5).

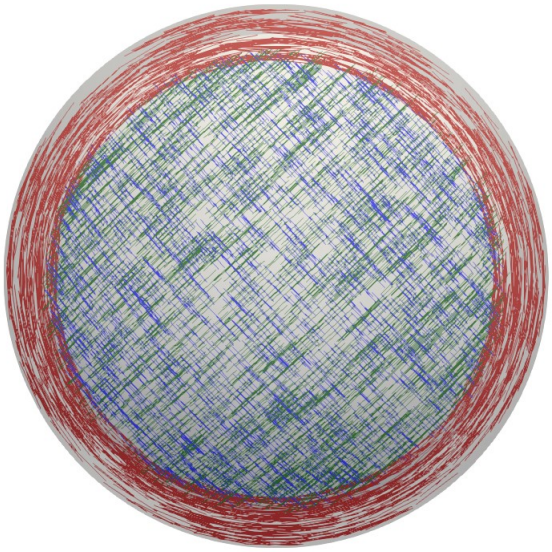

Figure 2.5: Visualization of the fibers of the anterior surface of the cornea using PARAVIEW: in red the circunferential orientetion of the fibers of the external region, in blue and green the N-T and I-S directions within the central region.

2.4. Boundary Conditions

Two different boundary conditions (BC) were tested (Figure 2.6). The first one consisted of *fixed* BC, which imposes a set of constraints at the elements composing the base of the cornea, meaning that the base could not move or rotate. The second BC imposed was the *sliding* at the base of the cornea: a best sphere fitting was performed through a least-square regression analysis, to determine the center of a spherical coordinate system. Only radial displacements were allowed, while polar and azimuthal movements were blocked .

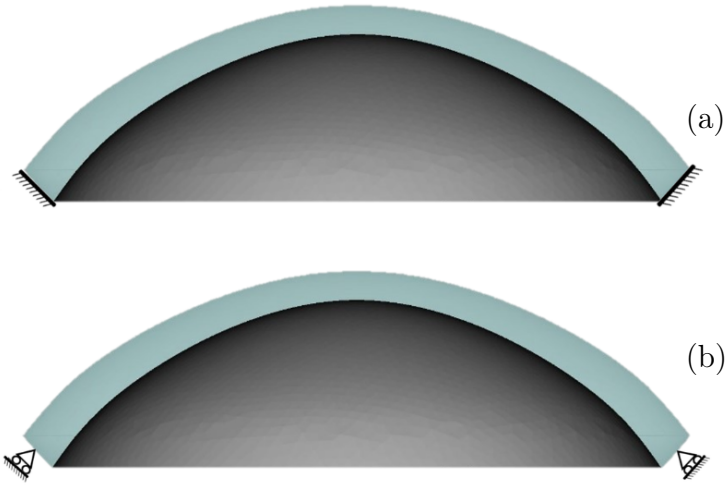

Figure 2.6: Boundary conditions application on ABAQUS 6.13 on the thickness set of elements of the cornea model: (a) fixed B.C., (b) sliding B.C.

2.5. Zero-Pressure

When the topographic acquisition of the patient's data are acquired, the eye is subjected to a physiological intraocular pressure (IOP), while the corneal pre-stress is neglected. For this reason, it is important to recover the initial stress-free configuration of the cornea in absence of the IOP: the zero-pressure geometry (Fig. 2.7).

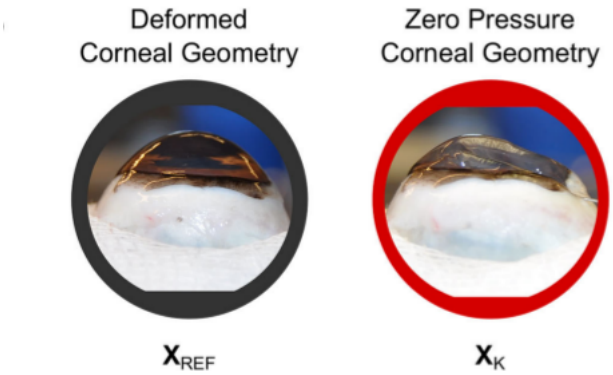

Figure 2.7: Influence of the IOP in the corneal shape [5].

The following algorithm from Ariza-Gracia et al.[5] was applied, in order to determine the stress-free configuration (algorithm in Figure 2.8, 2.9). It iteratively updates the nodal coordinates while preserving the mesh connectivity. X_{REF} represents the topographer's data derived geometry: X is a N_n x 3 matrix containing the nodal coordinates of the FE model. X_k identifies the zero-pressure configuration at iteration k and X_k^d represents the

deformed configuration when inflating the zero-pressure X_k at IOP pressure. The zero-pressure geometry is updated until the infinite norm of the nodal error between X_{REF} and X_k^d (TOL) is less than a defined value.

Given: X_{REF}, itemax, TOL

Initialize: $k = 0, X_k = X_{\text{REF}}$

Repeat

i) FE analysis: internal pressure (IOP*)

$X_k^d - X_{\text{REF}}$

$e_k = ||X_k^d - X_{\text{REF}}||_\infty$

ii) Update zero-pressure geometry

$X_{k+1} = X_k - e_k$

iv) $k = k + 1$

Until OR ($e_k \leq$ TOL, $k >$ itemax)

Figure 2.8: Algorithm for identification of the stress-free configuration [5].

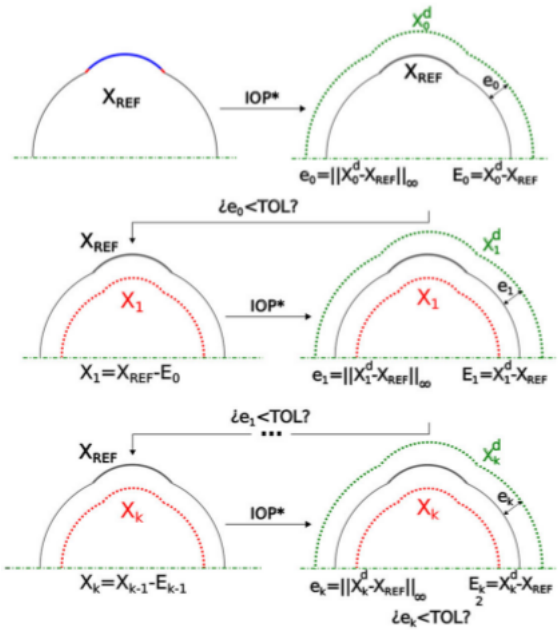

Figure 2.9: Graphical representation of the algorithm for identification of the stress-free configuration [5].

2.6. Laser Surgery FE Simulations

The zero-pressure configuration is the reference configuration from which the FE simulations were run. In the current thesis, two simulations were developed : PRK and SMILE FE surgeries. All the simulations were run using the software ABAQUS 6.13.

2.6.1. PRK simulation

The PRK simulation was made of two steps, one where the IOP was applied and the other where the laser ablation was performed, by removing the elements that were located in the ablation profile. In the case of the PRK model, the ablation volume was located at the anterior surface of the conic (Figure 2.10). The corneal models were generated with the ANSA pre-processor by BETA-CAE systems v22.0.1.

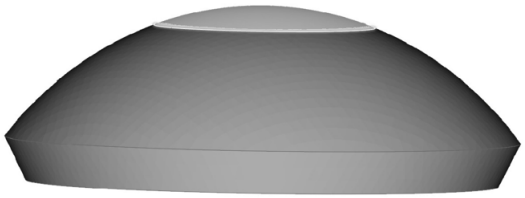

Figure 2.10: Models of PRK, where the ablation region is highlighted.

In the pressurization step, the IOP was applied to the internal surface of the ocular cavity (Figure 2.11). The value of the IOP was set at 15 mmHg, which is an average physiological value. Subsequently, it was changed to 12 mmHg and 20 mmHg to study its influence on the post-surgery maximum principal stress and maximum principal logarithmic strain distribuitions (see Chapter 2.8.5).

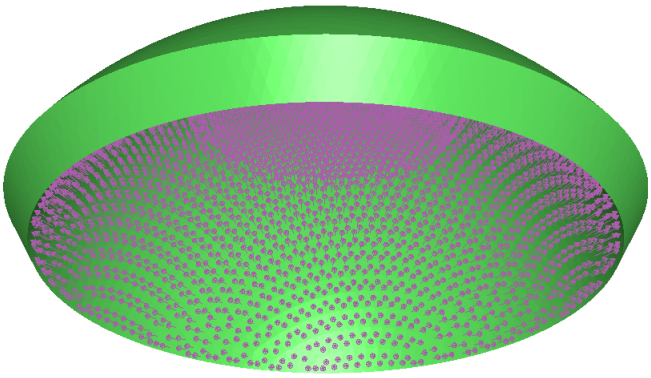

Figure 2.11: IOP load application (in purple) on ABAQUS 6.13 on the posterior surface of the cornea model.

In the ablation step, the PRK laser surgery was simulated by removing the ablation portion of elements of the anterior region of the cornea, through the interaction "Model-Change" on ABAQUS 6.13 (Figure 2.16(g)). In particular, the dioptric correction was set when the point clouds were built throughout a MATLAB 2023a code, following the Equation (2.2).

2.6.2. SMILE simulation

Starting from the corneal model, in the SMILE model, the ablation region was moved downwards through the corneal thickness (Figure 2.12). Different lenticule positions were investigated, to eventually select 120 µm, as will be explained in Chapter 2.8.1.

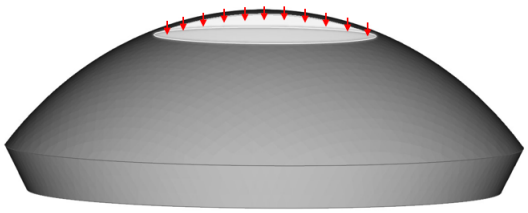

Figure 2.12: Models of SMILE, the ablation region is highlighted.

Likewise, both the pressurization step and the ablation step were defined in the SMILE model. In this simulation, an additional interaction was set, to simulate the contact between the internal surfaces after the lenticule extraction. In order to pursue the contact, the remaining internal surfaces of the cornea were selected in ANSA pre-processor by

BETA-CAE systems v22.0.1 (Figure 2.13) and they were merged trough the function "boolean" in ABAQUS 6.13. Subsequently, a "Self Contact" interaction of "type hard" was set on the surface created to avoid self penetration.

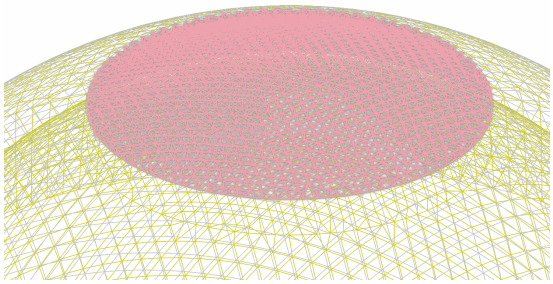

(a)

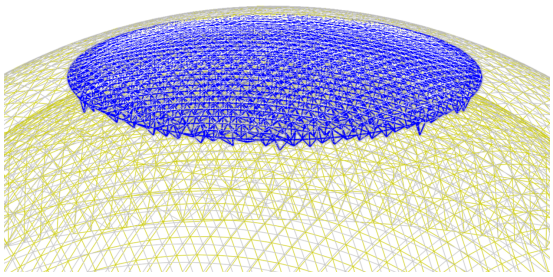

(b)

Figure 2.13: Elements composing the top (a) and bottom (b) surfaces of the cornea right after ablation selected on ANSA pre-processor by BETA-CAE systems v22.0.1.

2.7. Opto-mechanical Analysis of the simulations

To evaluate the optical performance of the models, the effective dioptric correction was computed by means of objective refraction: given the conic geometry of the model, the dioptric correction can be evaluated by looking at the curvature (measured in diopters D [1/m]) of the anterior corneal surface before and after the laser surgery. In the optical field, curvature is measured in diopters because its value is corrected by the term (n-1), where n = 1.3375 is the corneal keratometric refractive index. The difference between the post-surgical and the pre-surgical curvature values gives the dioptric correction obtained in the simulation. In order to calculate these values, an ellipsoidal fit, as explained by Navarro et al. [15], was used. In this algorithm, an ellipsoidal fitting is performed to obtain the minimum and maximum curvatures (K1 and K2, see Figure 2.1 for an example) of the corneal surface, also called principal curvatures, which are two parameters commonly used

in clinics. Subsequently, the mean curvature K_m (also indicated in any topography) is calculated as the mean of the two principal curvatures. The pre- and post-surgical mean curvature values are used for the evaluation of the achieved refractive correction. The OZ radius considered for the ellipsoidal fit analysis are of 3 mm, 3.5 mm and 4 mm.

Moreover, sagittal and mean curvature maps were computed to have a graphical view of the pre- and post-surgical anterior surface of the models, as in clinics. The sagittal curvature is the most used for corneal surface analysis in clinics, given its easy computation: it is defined as the inverse of the distance along the normal of a point of the surface and the optical axis, that passes for the origin of the reference for sake of simplicity 2.14 [50].

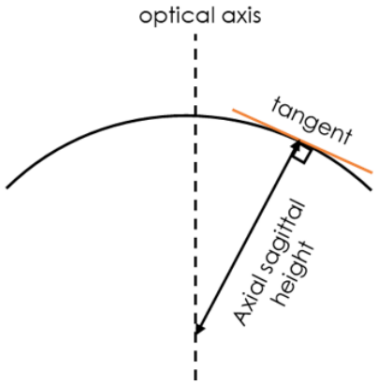

Figure 2.14: Sagittal curvature.

The mean curvature from differential geometry is calculated with the Equation 2.14.

$$H = \frac{(1 + h_x^2)h_{yy} - 2h_x h_y h_{xy} + (1 + h_y^2)h_{xx}}{2(1 + h_x^2 + h_y^2)^{3/2}} \tag{2.14}$$

where h_x, h_y, h_{xx}, h_{yy} are the first and second partial derivatives of $h(x)$, which represents the height of the cornea over its surface. This analysis, in fact, calculates the derivatives in each point of the anterior surface.

Before computing the curvature maps, Zernike polynomials were used to fit the surfaces and to reduce the error (Equation (2.15)).

$$h(r, \theta) = \sum_{n,m} C_n^m Z_n^m(r, \theta) \tag{2.15}$$

where $h(r, \theta)$, represents the fitted height of the surface in polar coordinates, Z_n^m is a polynomial sequence, that guarantees orthonormality over the whole circular surface, and C_n^m are the coefficients, that describe the root mean square of the optical error. The

indexes n and m represent the order and the phase of the polynomial. The condition of orthonormality is crucial because it allows to add terms without affecting those already computed. The fitting error is the percentage difference between the real surface and the polynomial-built one: in order to provide a low error, an order of 10 was selected (Figure 2.15).

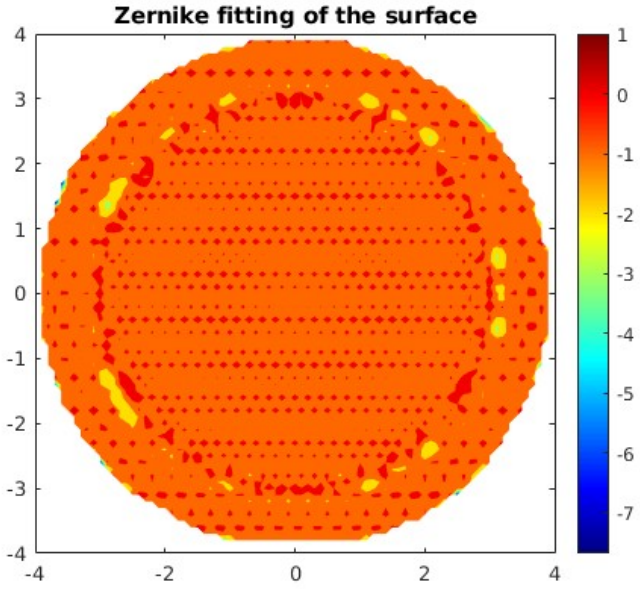

Figure 2.15: Zernike polynomial fitting error

The fitting error must be kept low in order to preserve the initial optical characteristics of patient's corneas. The mechanical analysis consisted in considering the maximal principal stress and maximal principal logarithmic strain distributions on the anterior, posterior and corneal section surfaces, the difference in this parameters before and after surgery and the apical node displacement. They were extracted for the pre-surgery configurations (meaning right after the IOP application) and the post-surgery one (meaning at the end of the ablation).

2.8. Simulations

Two groups of analyses were carried out, in order to determine the initial set up of the simulations:

- the boundary conditions analysis, which was previously explained in Chapter 2.4, to choose the boundary conditions to be applied to all the simulations that would have been run after;

- the lenticule position analysis in SMILE models, to determine where the ablation region should be located in the SMILE models (Chapter 2.8.1).

Subsequently, other models' parameters were changed in different analyses, regarding geometrical, optical and mechanical features for both PRK and SMILE models:

- variation of the desired dioptrical correction (Chapter 2.8.2);
- variation of the CCT of the models (Chapter 2.8.3);
- variation of the OZ (Chapter 2.8.4);
- Mechanical sensitivity analysis, varying the mechanical parameters (Chapter 2.8.5);
- Montecarlo analysis for the study of the influence of the material model onto the optical outcome, varying simultaneously the mechanical and geometrical properties (Chapter 2.8.6).

2.8.1. Lenticule Position analysis in SMILE surgery simulation

When developing the SMILE surgery simulation pipeline, the influence of the lenticule position throughout corneal thickness was analysed. For this analysis, an OZ of radius R_{OZ} = 3 mm was selected and a myopic correction of -4 D was set.

At the beginning, the lenticule was placed at a 75% depth of the central corneal thickness (CCT) with respect to the anterior surface and progressively moved to 60%, 50% , 40%, 30% and 20% depth of the CCT (Figure 2.16 (a)-(f)). Being the SMILE surgery actually performed between 30% and 20% of CCT in current clinical procedures, the major concern of this procedure are the post-operative complications due to the structural changes caused to the mechanical properties of the corneal tissue: the superficial layer does not fully preserve its mechanical resistance and the posterior surface is subjected to a higher load. For this reason, the aim was to evaluate the influence of this parameter on the optical properties of the post-surgical configuration and determine if it was doable to place more in depth the lenticule, also from a mechanical point of view.

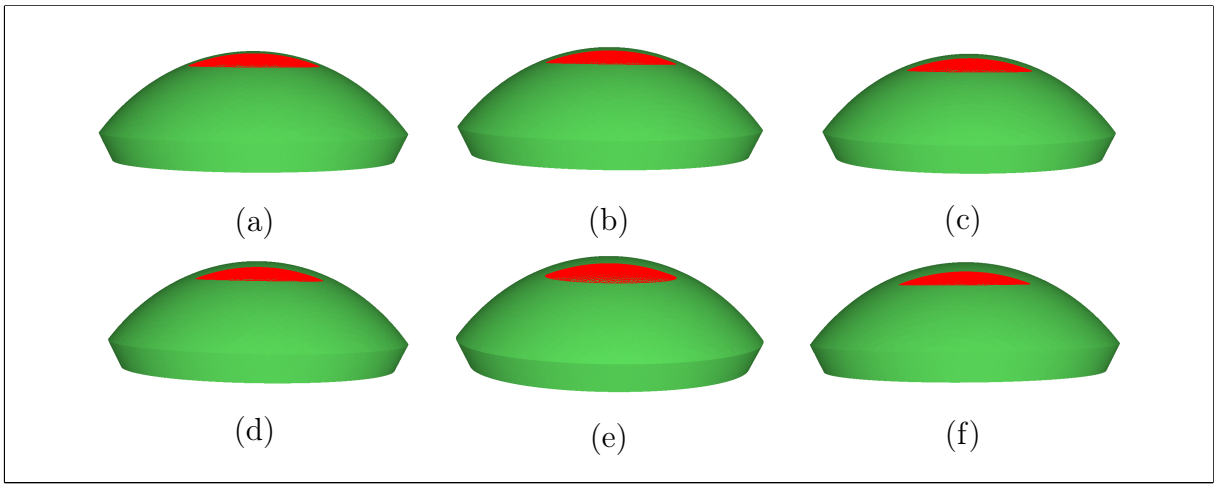

Figure 2.16: ABAQUS representations of the ablation elements for SMILE with lenticule position depth at 20% CCT (a), 30% CCT (b), 40% CCT (c), 50% CCT (d), 60% CCT (e), 75% CCT (f) with an OZ of 3 mm and CCT from Pentacam data.

The mechanical outputs of interest, used to compare the different cases, were the anterior and posterior surface apex displacements of the corneal models.

The optical analysis consisted in calculating the actual dioptric correction obtained for each case, evaluating the mean curvature of the anterior surface in the pre-surgery and post-surgery configurations. Furthermore, the mean value of the maximum principal stresses and maximum principal logarithmic strains of four apical elements of the anterior and posterior surface of the models were collected (as will be further shown in Figure 2.17 (b)).

2.8.2. Dioptric target correction variation

Another analysis that was performed was related to the dioptric correction goal: while the initial choice was to correct a fixed myopic defect of -4 D, which is the value that was considered in all the previously run simulations, the correction was then set to higher values to test the influence of this parameter on the optomechanical performance of the two simulations: in particular it was set to -5 D, -6 D, -7 D, and -8 D in both PRK and SMILE models. The other parameters were kept constant: OZ of radius $R_{OZ} = 3$ mm and, the lenticule position was kept at 20% of CCT (only for SMILE models). The ablation depths for each simulation are reported in Table 2.2. For these simulations, the actual dioptric corrections were collected, by means of the mean curvature of the anterior surface in the pre- and post-surgical configurations.

Moreover, the mechanical changes due to the different dioptric corrections and, consequently, to the ablations depths are reported, by looking at the apical node displacement of the anterior surface before and after surgery (as explained in Chapter 2.8.1).

As it will be deeply explained in the results (See Section 3.3), the SMILE surgery with the theoretical ablation profile from literature [42] showed poorer optical outcome with respect to PRK model. This could be caused by the fact that in clinics a correction of 10% higher with respect to the refractive target is applied to avoid under-corrections. Moreover, an additional thickness of 15 µm is considered when choosing the proper lenticule profile to avoid rupture when the surgeon extracts it. For these reason, other 5 simulations of SMILE surgery models were run. These models considered a 10% higher correction and an external thickness of 15 µm (with an OZ of radius 3.25 mm). The maximal lenticules' thickness that were used are reported in Table 2.4.

Dioptric correction [D]	CCT [µm]	Lenticule Maximal Thickness [µm]
-1 (1.1)	579	33
-2 (2.2)	579	51
-3 (3.3)	579	69
-4 (4.4)	579	85
-5 (5.5)	579	101

Table 2.4: Parameters for the clinical data based SMILE simulations.

Then, the mean curvature of the anterior surfaces these models was collected.

2.8.3. CCT variation

Then, the CCT parameter was investigated too. It was changed with the following values of 500, 510, 520, 530, 540, 550, 560, 570, 580, 590, 600 µm both for SMILE and PRK models to determine the optical and mechanical influence of on the simulations.

Both optical and mechanical analysis were performed. The dioptric correction was calculated by means of the mean curvature obtained with the ellipsoidal surface fitting, while the mechanical properties were evaluated looking at the apical node displacement of the anterior surface before and after surgery.

Moreover, when analysing the models' mechanical behaviour after surgery, 5 elements were selected from the anterior and posterior surfaces of the corneal models (Figure 2.17).

The corresponding maximum principal stress and logarithmic strain were obtained from ABAQUS CAE 6.13 and then averaged.

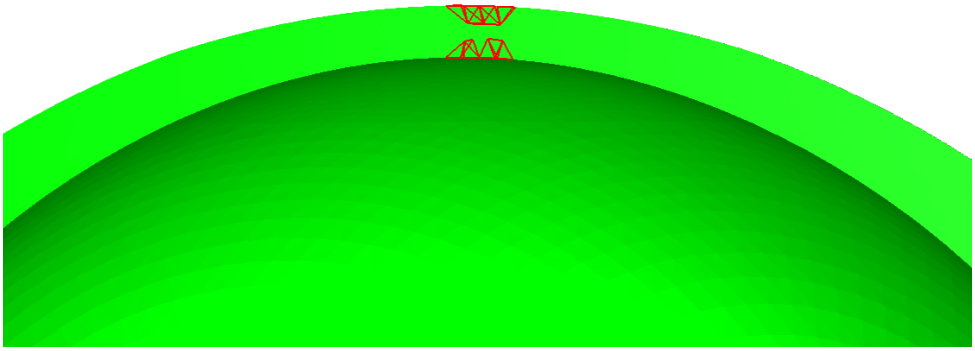
(a)

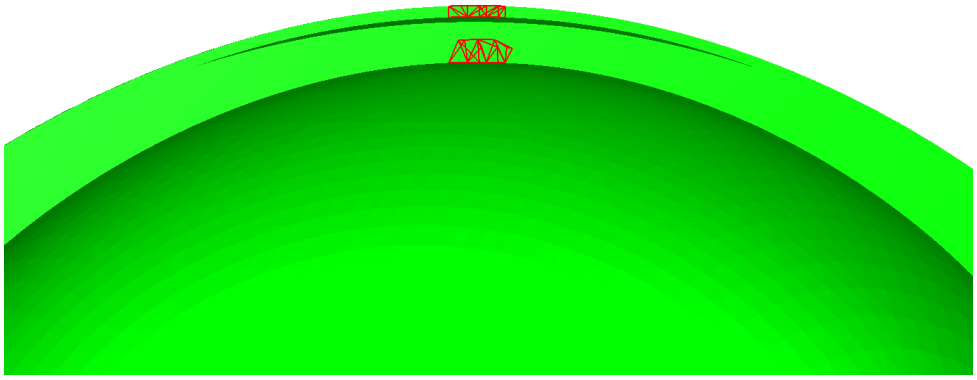
(b)

Figure 2.17: Elements selection (in red) on the anterior and posterior surface of PRK (a) and SMILE (a) models for the mechanical analysis.

2.8.4. OZ radius variation

As said in Chapter 2.1.2, the OZ parameter directly affects the ablation depth of the models: when the OZ is larger, the lenticule becomes thicker (see Table 2.2). For both PRK and SMILE, three models with OZ radii of 3 mm, 3.5 mm and 4 mm were compared, in terms of refractive outcome (i.e. reached dioptric correction). The dioptric corrections were evaluated through the ellipsoidal surface fitting mean curvature method.

2.8.5. Sensitivity analysis: 2^5 full factorial design

In order to determine which factors had the higher influence on the optical and mechanical results, a sensitivity analysis on the parameters of the two simulations was performed. The

five chosen parameters related to the mechanical behaviour of the cornea were: the matrix stiffness constant C_{10}, the fibers' stiffness constant k_1, the fibres non-linearity constant k_2, the IOP and the central corneal thickness. They influence the final curvature assumed by the anterior corneal surface after surgery, directly related to the refractive power of the eye. A 2^5 full factorial design of experiment was conducted, combining the values in Table 2.5 for PRK and for SMILE, with a total of 64 simulations, 32 for PRK and 32 for SMILE models. A variation of ±50% was applied to the material constants (C_{10}, k_1 and k_2, while the IOP and the thickness assumed different values in a physiological and non-pathological range. The minimum thicknesses of the models were set for PRK and SMILE at 490 µm and 500 µm, respectively, being the lowest values at which the two surgeries are performed, in order to avoid a higher risk of developing post-surgical complications [27].

	C_{10} [kPa]	k_1 [kPa]	k_2 [-]	IOP [mmHg]	CCT [µm]	Dioptric correction [D]	Ablation Thickness [µm]
Target	30	20	400	15	579	-4	47.6
Low (PRK)	15	10	200	12	490	-4	47.6
Low (SMILE)	15	10	200	12	500	-4	47.6
High	45	30	600	20	600	-4	47.6

Table 2.5: Set of parameters for the full factorial analysis.

Each simulation was performed starting from the construction of the model using 32 combination of these parameters (as shown in Table 2.6), imposing the zero-pressure configuration, the IOP and the ablation both for PRK and SMILE. The outputs considered for each simulations were the dioptric correction, the anterior and posterior surface stress and displacement configurations before and after surgeries and their differences.

Test	C_{10} [kPa]	k_1 [kPa]	k_2[-]	IOP [mmHg]	Thickness [µm]	
					PRK	SMILE
1	45	30	600	20	600	600
2	15	30	600	20	600	600
3	45	10	600	20	600	600
4	15	10	600	20	600	600
5	45	30	200	20	600	600
6	15	30	200	20	600	600
7	45	10	200	20	600	600
8	15	10	200	20	600	600
9	45	30	600	12	600	600
10	15	30	600	12	600	600
11	45	10	600	12	600	600
12	15	10	600	12	600	600
13	45	30	200	12	600	600
14	15	30	200	12	600	600
15	45	10	200	12	600	600
16	15	10	200	12	600	600
17	45	30	600	20	490	500
18	15	30	600	20	490	500
19	45	10	600	20	490	500
20	15	10	600	20	490	500
21	45	30	200	20	490	500
22	15	30	200	20	490	500
23	45	10	200	20	490	500
24	15	10	200	20	490	500
25	45	30	600	12	490	500
26	15	30	600	12	490	500
27	45	10	600	12	490	500
28	15	10	600	12	490	500
29	45	30	200	12	490	500
30	15	30	200	12	490	500
31	45	10	200	12	490	500
32	15	10	200	12	490	500

Table 2.6: Mechanical Sensitivity analysis set of parameters.

A two-way ANOVA analysis was then performed to determine which were the most influential variables and, also, if the interaction among them was significant.

2.8.6. Montecarlo analysis

To fully understard the influence of the material model onto the optical outcome of the two surgeries' simualtions, a second analysis based only on the dioptric correction was carried out. In particular, four different corneal models with different CCTs (500, 530, 560, 590) µm were selected, for both PRK and SMILE, varying the C_{10}, k_1 and k_2, randomly choosing 60 values from the ranges in Table 2.7 and running 60 simulations for each CCT case, for a total of 240 simulations for PRK and 240 for SMILE. The desired dioptric correction was set at -4 D for all the cases. The mean curvature of the anterior surface of the pre- and post-surgical models was computed and the dioptric corrections were derived. Then, a linear relation, through linear regression, between the CCT of the corneal model and the dioptric correction was derived.

	C_{10} [kPa]	k_1 [kPa]	k_2 [-]
Low	15	10	200
High	45	30	600

Table 2.7: Set of parameters for the Montecarlo analysis

2.9. Patient-Specific Models

After analyzing a conic and symmetric geometry, the choice to investigate a patient-specific case was made, in order to simulate surgeries performed on a real patient and verify if the correction obtained in the simulations reflects the correction obtained in the surgery performed in clinics. For this purpose, Pentacam data were used to build the corneal geometries. In particular, a patient who underwent PRK was taken into account. Both surgeries were simulated onto the same patient, in order to be able to compare both optical and mechanical performance of the two surgeries' simulations. The patient signed a written informed consent and data were anonymized by our clinical partner, Barraquer Ophtalmologic Center (Barcelona). Data acquisition followed good clinical practices and adhered to the tenets of the Declaration of Helsinki. This study was approved by the Ethics Committee of Research with drugs of the Barraquer Ophtalmologic Center (CEIm), Spain (Code CEIM: 191_Modelización_PRK).
The corneal model was built starting from the outputs of the Pentacam topography, which provide an *elevation* file, that consists of a point cloud of the anterior and posterior

surfaces, taking into account corneal thickness point-wisely. Then, since Pentacam topographer is unable to reconstruct the whole corneal surface ($\phi = 12$ mm) due to patient misalignment and blinking (it covers an area between 5 and 8 mm), it is necessary to apply an algorithm to reconstruct the missing portion of the surface, in order to build the 3D FE model. Data extrapolation is performed by means of Zernike polynomials to fit and reconstruct the corneal surfaces (Figure 2.18).

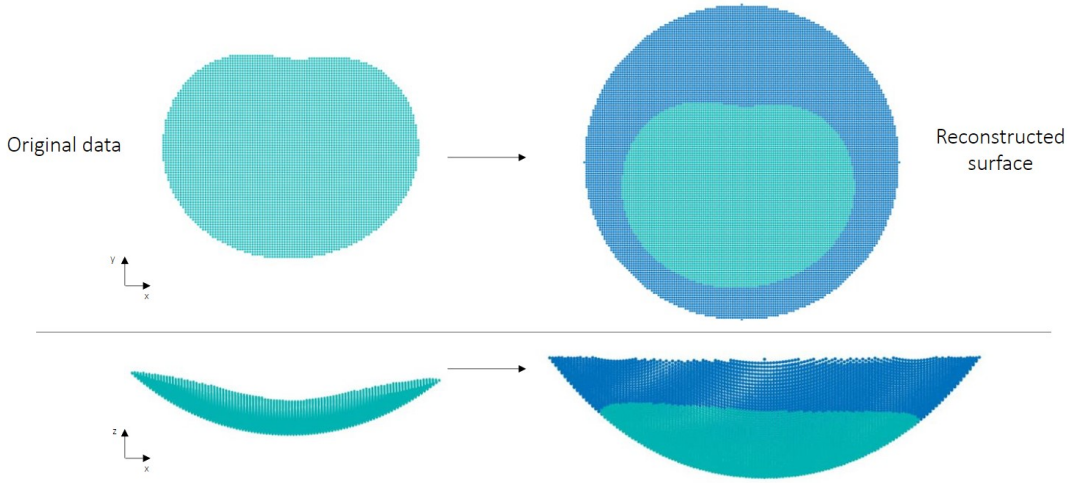

Figure 2.18: Reconstruction of missing portion of surface through Zernike polynomials.

For the patient-specific models, a biconic geometry was selected to define the ablation profile, since it is a more complex and realistic geometry, when compared with the conic, as it also allows to consider astigmatism, given the possibility to have distinct curvatures on different meridians (Figure 2.19). The biconic equation in cilindrical coordinates is the following (Equation 2.16) [52]:

$$z(\rho, \theta, R_s, R_f, Q_s, Q_f, \theta_s, z_0) = z_0 - \frac{\rho^2 A}{\left(1 + \sqrt{1 - \rho^2 B}\right)} \tag{2.16}$$

where

$$A = \frac{\cos^2(\theta - \theta_s)}{R_s} + \frac{\sin^2(\theta - \theta_s)}{R_f} \tag{2.17}$$

and

$$B = (Q_s + 1)\frac{\cos^2(\theta - \theta_s)}{R_s^2} + (Q_f + 1)\frac{\sin^2(\theta - \theta_s)}{R_f^2} \tag{2.18}$$

Where R_s and R_f are the radii of curvature of the steepest and the flattest meridians, Q_s and Q_f are the corresponding asphericities and θ_s is the angle of astigmatism.

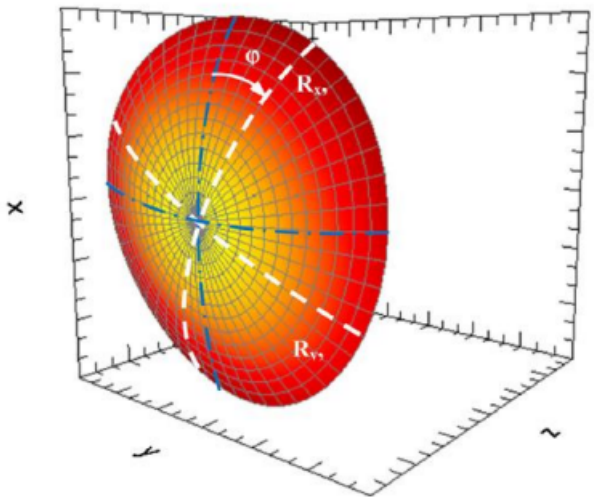

Figure 2.19: Schematic representation of a biconic surface [21]

For the patient-specific case, sliding BC were used and patient's biomechanically-corrected IOP measured with Corvis Non-Contact Tonotemer was applied (bIOP = 19.88 mmHg). Moreover, the material parameters used in all the conic simulations were applied (Table 2.3), but subsequently the C_{10} coefficient was changed to an higher and a lower value (Table 2.8), to simulate a stiffer and a softer material, to see if a better optical results could be achieved, closer to the actual dioptric correction obtained in surgery.

	C_{10} [kPa]	k_1 [kPa]	k_2 [-]
Initial	30	20	400
Low	15	20	400
High	60	20	400

Table 2.8: Three sets of parameters for the material of the patient-specific models.

After performing the simulations, the mechanical analysis was carried out, comparing the two surgeries in terms of maximal principal stress and strain on anterior, posterior surfaces and corneal section. Furthermore, an optical analysis was carried out too, fitting the surfaces of the pre- and post-surgical configurations again with the ellipsoidal fit by Navarro et al. [15], for all the material models previously illustrated. The pre-surgical sagittal curvature map was computed using the Zernike polynomials for the fitting of the surfaces and compared to the one computed by Pentacam topographer to verify that the patient-specific model was actually reproducing the initial optical properties of patient's cornea.

2.9.1. PRK surgery

The patient underwent PRK refractive surgery, performed with the excimer laser Wavelight EX500 by Alcon (Forth Worth, Texas, USA). The treatment plan was exported directly from the software associated to the employed laser (Figure 2.21).
The pre-surgical Pentacam topography of the patient is reported in Figure 2.20.

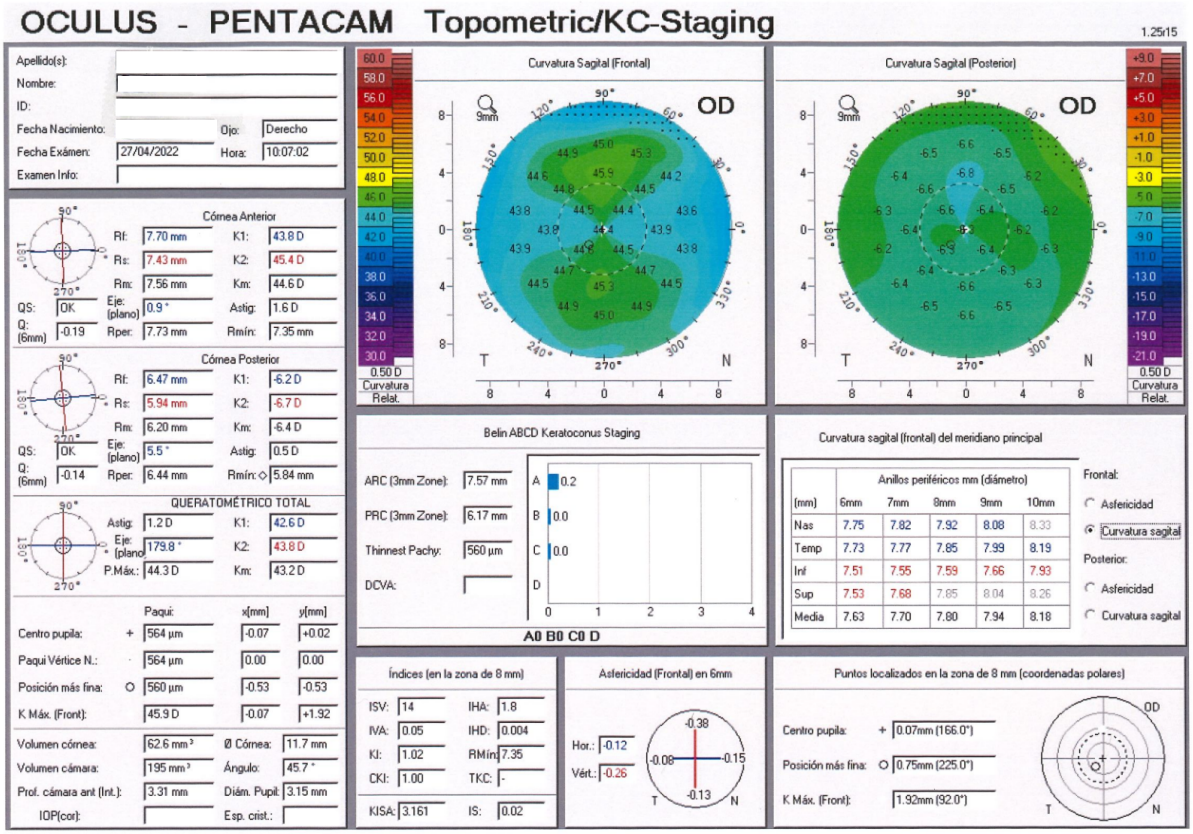

Figure 2.20: Pentacam topography of the PRK patient.

The initial mean curvature , given by the mean of the two principal curvatures, is $K_m = (K_1 + K_2)/2 = 44.6$ D, the ablation depth was extracted from the treatment report and was of 74.09 µm to correct -4 D of myopia and -1 D x 170° of astigmatism, considering an OZ of 6.50 mm (Figure 2.21).

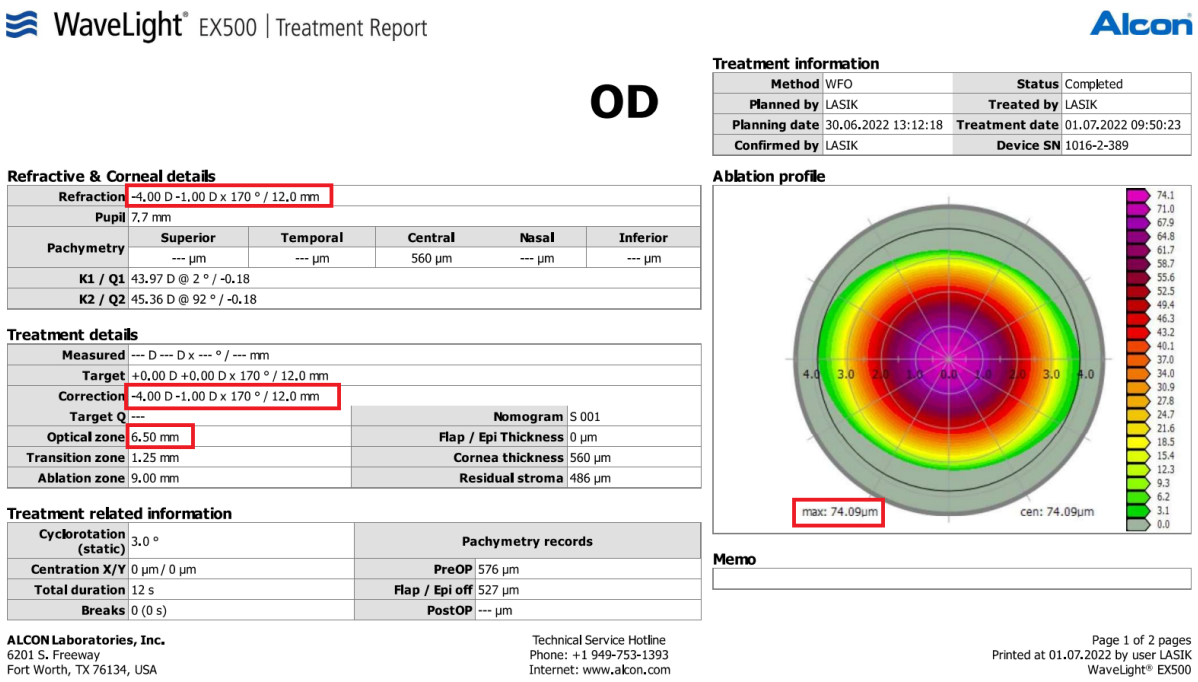

WaveLight® EX500 | Treatment Report

Alcon

OD

Treatment information

Method	WFO	**Status**	Completed
Planned by	LASIK	**Treated by**	LASIK
Planning date	30.06.2022 13:12:18	**Treatment date**	01.07.2022 09:50:23
Confirmed by	LASIK	**Device SN**	1016-2-389

Refractive & Corneal details

Refraction	-4.00 D -1.00 D x 170 ° / 12.0 mm				
Pupil	7.7 mm				
Pachymetry	**Superior**	**Temporal**	**Central**	**Nasal**	**Inferior**
	--- µm	--- µm	560 µm	--- µm	--- µm
K1 / Q1	43.97 D @ 2 ° / -0.18				
K2 / Q2	45.36 D @ 92 ° / -0.18				

Ablation profile

Treatment details

Measured	--- D --- D x --- ° / --- mm		
Target	+0.00 D +0.00 D x 170 ° / 12.0 mm		
Correction	-4.00 D -1.00 D x 170 ° / 12.0 mm		
Target Q	---	**Nomogram**	S 001
Optical zone	6.50 mm	**Flap / Epi Thickness**	0 µm
Transition zone	1.25 mm	**Cornea thickness**	560 µm
Ablation zone	9.00 mm	**Residual stroma**	486 µm

Memo

Treatment related information

Cyclorotation (static)	3.0 °	**Pachymetry records**	
Centration X/Y	0 µm / 0 µm	**PreOP**	576 µm
Total duration	12 s	**Flap / Epi off**	527 µm
Breaks	0 (0 s)	**PostOP**	--- µm

ALCON Laboratories, Inc.
6201 S. Freeway
Fort Worth, TX 76134, USA

Technical Service Hotline
Phone: +1 949-753-1393
Internet: www.alcon.com

Page 1 of 2 pages
Printed at 01.07.2022 by user LASIK
WaveLight® EX500

Figure 2.21: Treatment details for PRK surgery.

Clinicians and optometrists usually refer to the mean curvature K_m as sphere power (S) to indicate the pre- and post-surgical optical power of patients' corneas and the needed myopic correction that they should receive. Moreover, given that in real patient-specific cases the symmetry in the cornea is lost, the term cylinder is also used to describe the degree of astigmatism that affects patients' corneas and it is calculated as the difference between the two principal curvatures (C = K1 - K2).

2.9.2. SMILE surgery

While the target correction corresponded to the refraction of the patient for the PRK case (see red rectangles in Figure 2.20), it was necessary to take into account some more aspects for the SMILE model. During the development of the current thesis' work, thanks to the feedbacks received from our clinical partner, we discovered two important aspects that must be considered when simulating SMILE surgery. The first was that the ablation depth in SMILE surgery is a 10% higher with respect to PRK at the same dioptric target, e.g. for the refractive correction of the patient of interest (-5 D, given by the sum of sphere and cylinder powers), in PRK an ablation of 74.05 µm is performed, while in SMILE a correction of -5.5 D is applied and a lenticule thickness of 86 µm is obtained. Moreover, above mentioned 15 µm of thickness must be added to the whole lenticule, to avoid the

rupture at the extraction (see Section 2.8.2). Consequently, the final lenticule thickness applied to the SMILE model was of 101 µm, much higher than the ablation performed in the PRK model. Also for SMILE model, an OZ of 6.5 mm was considered.

3 | Results

This chapter describes the results obtained in this thesis. First, the analysis of the boundary conditions is reported and commented. Then, the lenticule positioning in SMILE simulations was investigated. The changes in the target dioptric correction were analysed. Subsequently, the OZ diameter and the influence of the CCT were explored. To have an overview of all the aspects that were analysed in each study, the full-factorial and Montecarlo analyses were run, in order to study simultaneously the influence of different variables. Finally, the last results consisted in the validation of the models throughout a comparison between patient-specific data and the data obtained throughout FE simulations for both the surgeries.

3.1. Boundary Conditions analysis

The first step consisted in choosing the boundary conditions for the surgery models. In this step, the *fixed* and the *sliding* BC were analyzed, in order to highlight the differences they cause in the mechanical and optical outcome. Moreover, it was important to evaluate if one of the two BC better represented the real corneal configuration or if the the differences between them were negligible in the region of interest, namely the OZ. The comparison between two PRK models with a 579 µm CCT (derived from the Pentacam patient's data), a -4 D refractive desired correction and a 6 mm OZ diameter was carried out: one with fixed BC and one with sliding BC. Furthermore, two SMILE models with those same parameters and a lenticule situated at the 20% of the CCT depth starting from the corneal anterior surface (which is the value used in surgery and will be further investigated in Chapter 3.2) were built and the two different BC were tested, too. The maximum principal stresses and maximum principal logarithmic strains differences between the post-surgery configuration and the pre-surgery one were collected as outputs of the simulations, in order to perform an evaluation of the tested BC.

3.1.1. Mechanical results

The maximal principal stresses and logarithmic strains distributions through all the corneal volume after ablation are quite different between the two boundary conditions. For PRK, higher maximal principal stresses are concentrated in the outer zone of the posterior surface of the sliding BC model (Figure 3.1), while higher maximum principal logarithmic strains are concentrated in the outer zone of the posterior surface of fixed BC models (Figure 3.2). Nevertheless, in the OZ, the mechanical behaviour in PRK models can be considered equivalent, as reported in Table 3.1, where the mean values of maximal principal stresses and logarithmic strains of the anterior and posterior surfaces apical elements are displayed.

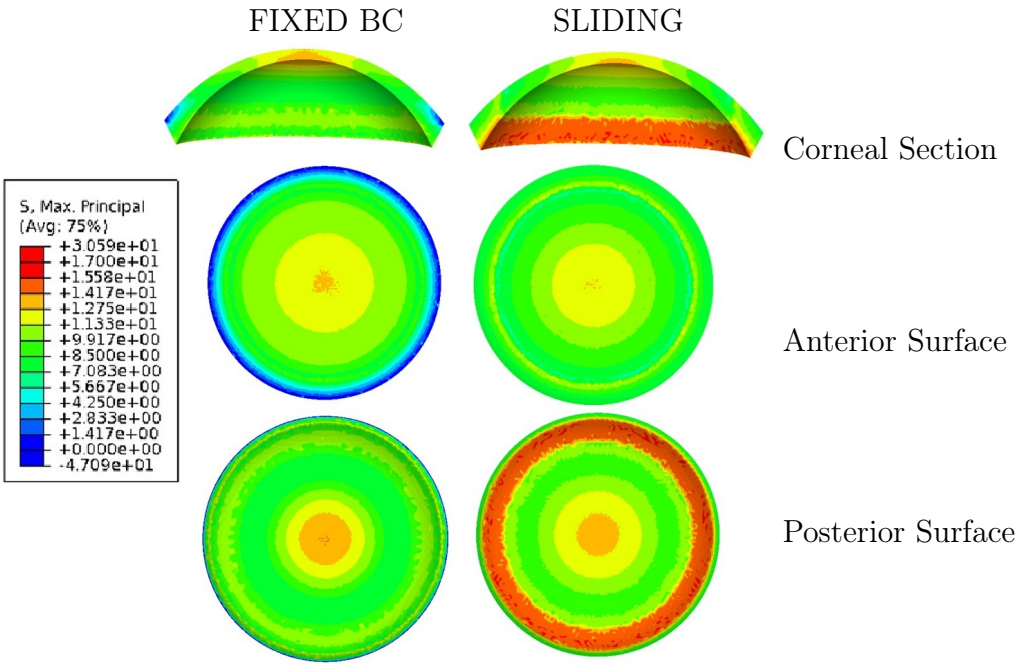

Figure 3.1: Maximum principal stress distribution [kPa] in PRK simulation.

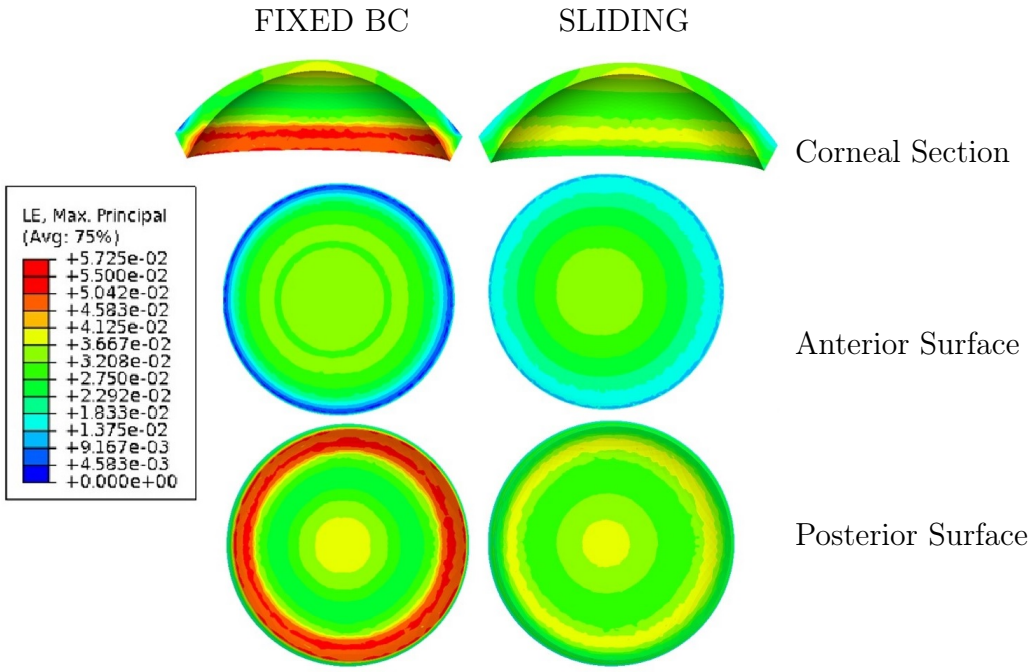

Figure 3.2: Maximum principal logarithmic strain distribution [-] in PRK simulation.

	PRK			
	Fixed BC		Sliding	
	Anterior apical element	Posterior apical element	Anterior apical element	Posterior apical element
Maximum principal Logarithmic Strain [-]	0.036	0.040	0.035	0.036
Maximum principal Stress [kPa]	12.72	13.94	12.53	12.71

Table 3.1: Maximum principal logarithmic strain and maximum principal stress for anterior and posterior apical nodes in fixed BC and sliding BC in PRK analysis

In SMILE models, the results are similar: higher maximal principal stresses are concentrated in the outer zone of the posterior surface of the sliding BC model (Figure 3.3), while higher maximum principal logarithmic strains are concentrated in the outer zone of the posterior surface of both models and are higher in fixed BC model (Figure 3.4). However, also in this case, the mechanical behaviour in the OZ can be considered equivalent, as shown by the mean values of maximal principal stresses and logarithmic strains of the anterior and posterior surfaces apical elements (Table 3.2).

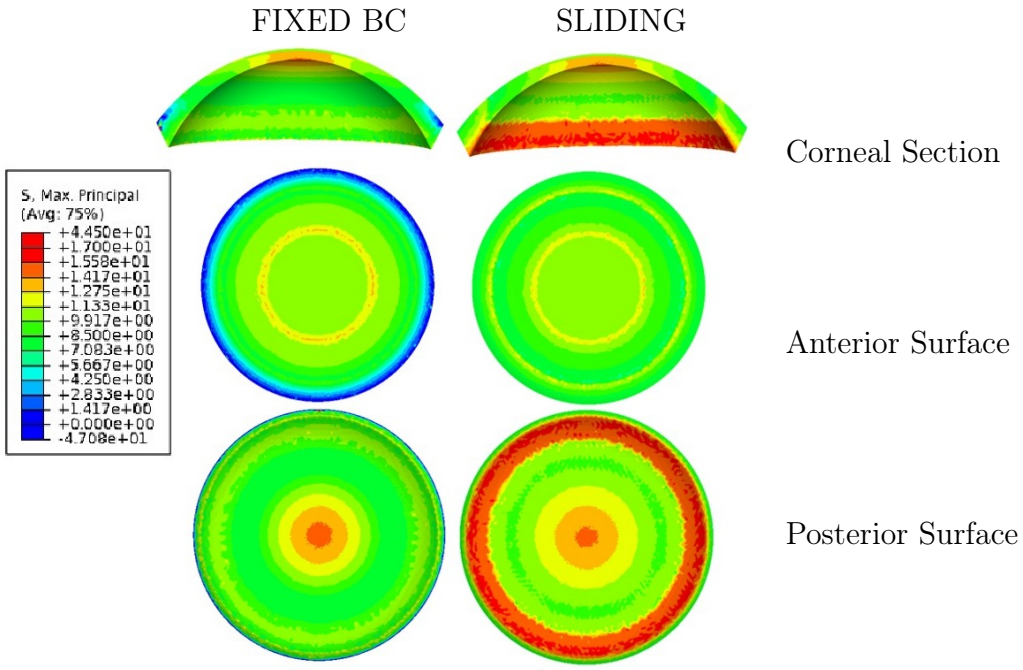

Figure 3.3: Maximum principal stress distribution [kPa] in SMILE simulation.

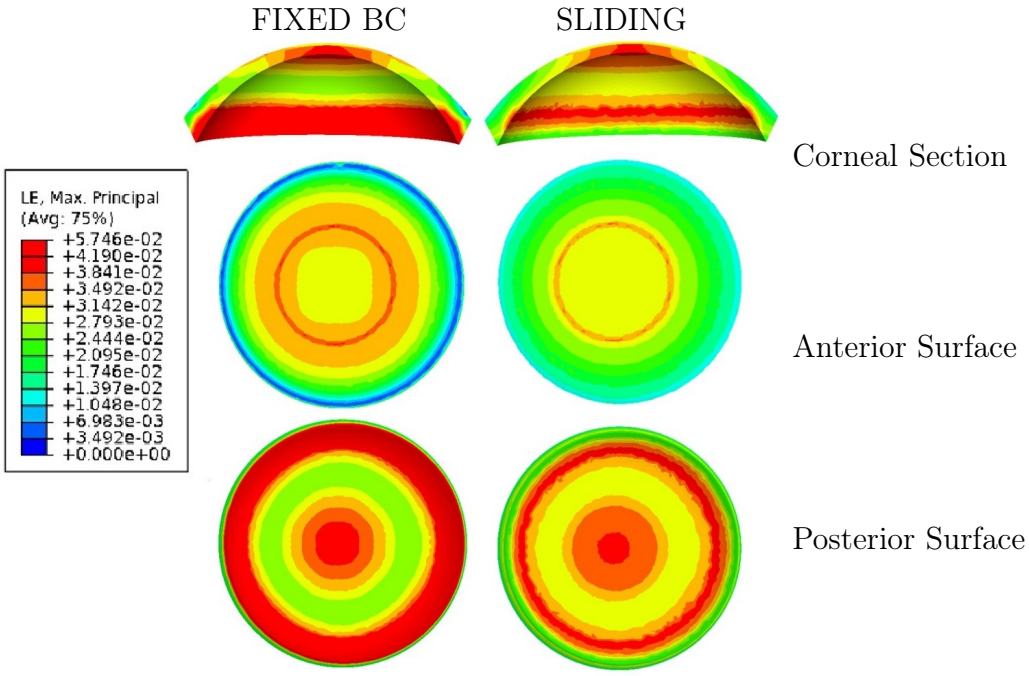

Figure 3.4: Maximum principal logarithmic strain [-] distribution in SMILE simulation.

	SMILE			
	Fixed BC		Sliding	
	Anterior apical element	Posterior apical element	Anterior apical element	Posterior apical element
Maximum Principal Logarithmic Strain [-]	0.030	0.040	0.029	0.040
Maximum principal Stress [kPa]	10.50	14.53	10.00	13.95

Table 3.2: Maximum principal logarithmic strain and maximum principal stress for anterior and posterior apical nodes in fixed BC and sliding BC in SMILE analysis

3.1.2. Optical Results

The ellipsoid-fitted mean curvatures are calculated for different OZ radii (3, 3.5 and 4 mm). The results reveal that the anterior surface curvature difference before and after surgery, meaning the dioptric power change, do not vary significantly in the OZ of interest when the boundary conditions are changed (Table 3.3, 3.4).

The fixed BC causes a higher anterior apical node displacement in the PRK models when compared to the sliding, where the limbus is more free to move radially, but in curvature terms, the difference between the achieved dioptric corrections between the two BC is null (Table3.3). In the SMILE models, the maximum difference in terms of dioptric correction is 0.4 D, where a R_{OZ} of 3 or 3.5 mm is considered, while is 0.2 D for a R_{OZ} of 4 mm (Table 3.4). This last value can be considered negligible.

Moreover, when comparing PRK and SMILE with the same boundary conditions, a better dioptric correction is noticeable for the PRK procedure: for sliding BC, the difference between the two procedures is maximum 1.2 D correction (if the case of a 3 and 4 mm R_{OZ} is considered) while, for fixed BC, a maximum difference of 1 D correction is reached (considering the case of $R_{OZ} = 3.5$ and 4 mm). The pre-surgical mean curvatures maps are the same both for PRK and SMILE with the same boundary conditions, as the ablation has not taken place yet (Figure 3.5). The post-ablation configurations are reported in Figure 3.5, and show that in the OZ, the difference between the BC is null.

R_{OZ} [mm]	PRK					
	FIXED BC			SLIDING BC		
	Mean Curvature [D]					
	pre-surgery	post-surgery	achieved correction	pre-surgery	post-surgery	achieved correction
3	41.7	39.5	-2.2	41.7	39.5	-2.2
3.5	41.7	38.4	-3.3	41.7	38.4	-3.3
4	41.8	38.1	-3.7	41.8	38.1	-3.7

Table 3.3: Anterior surface ellipsoid-fitted mean curvatures for fixed and sliding BCs in PRK.

R_{OZ} [mm]	SMILE					
	FIXED BC			SLIDING BC		
	Mean curvature [D]					
	pre surgery	post surgery	achieved correction	pre surgery	post surgery	achieved correction
3	41.7	40.3	-1.4	41.7	40.7	-1.0
3.5	41.7	39.4	-2.3	41.7	39.8	-1.9
4	41.8	39.1	-2.7	41.8	39.1	-2.5

Table 3.4: Anterior surface ellipsoid-fitted mean curvatures for fixed and sliding BCs in SMILE.

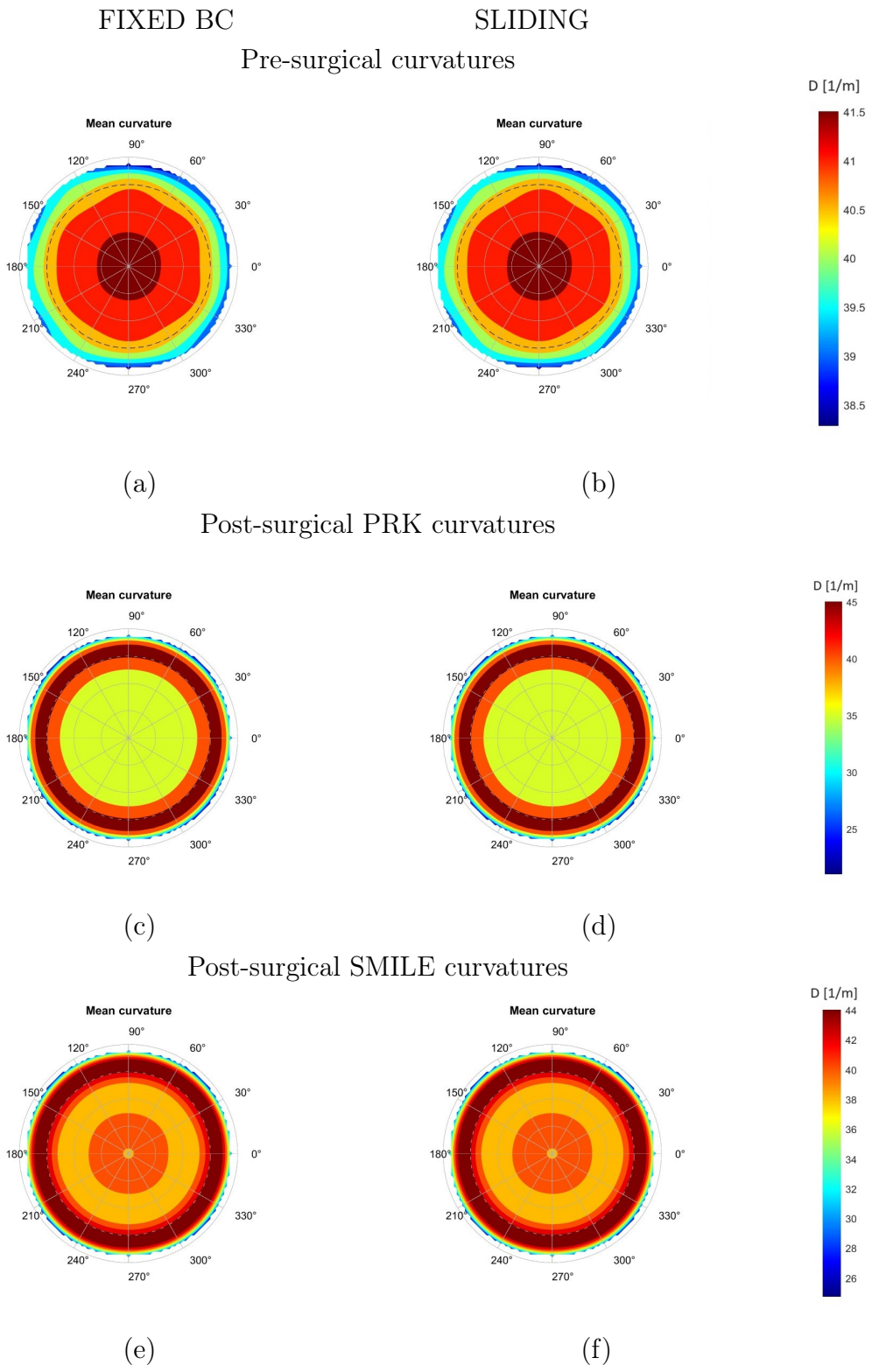

Figure 3.5: Pre-surgical mean curvatures for fixed (a) and sliding (b) BCs; post-surgical mean curvatures for PRK with fixed (c) and sliding (d) BC, post-surgical mean curvatures for SMILE with fixed (e) and sliding (f) BC

The anterior and posterior surface profiles of both models with fixed boundary conditions were plotted in Figure 3.6. The anterior surface apical node before the surgery is located in (0;0), while after ablation, both the surgeries present a downwards displacement of the anterior surface, due to the elimination of the ablation region of the cornea. PRK shows a more accurate dioptric correction and this is confirmed by a higher flattening of the anterior surface, which ensures a higher refractive correction (Figure 3.6 (a)). The posterior surface, on the other hand, is moving upwards, mainly due to the IOP application both for PRK and SMILE (Figure 3.6(b)). Similar results can be observed in the sliding boundary condition profiles, without a significant difference in behaviour (Figure 3.7).

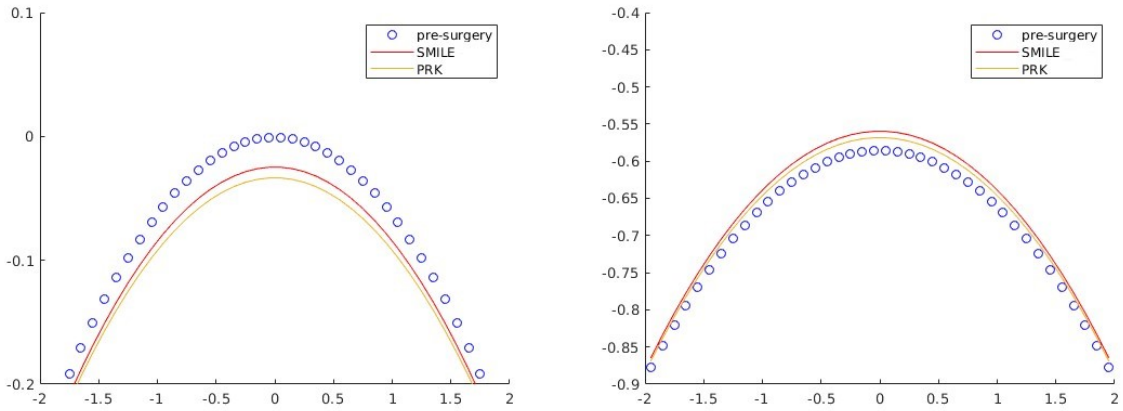

(a) (b)

Figure 3.6: Anterior surface (a) and posterior surface (b) profiles for PRK and SMILE models with fixed BC .

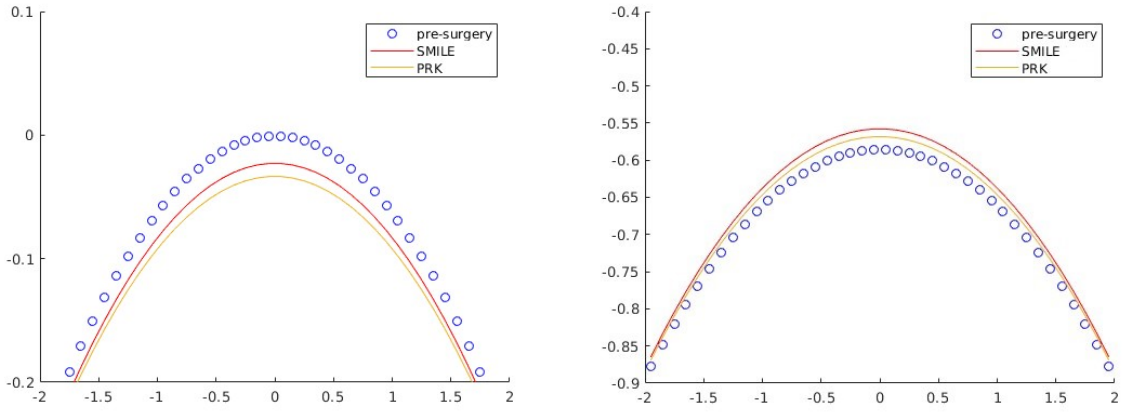

(a) (b)

Figure 3.7: Anterior surface (a) and posterior surface (b) profiles for PRK and SMILE models with sliding BC.

The decision to use the *fixed* boundary condition from now on was made, as it provides a lower computational cost, considering that the two boundary conditions are analogous from a mechanical and optical point of view in the OZ of interest.

3.2. Lenticule position in SMILE Surgery

The value at which the SMILE surgery is currently performed in clinic is at 110 - 120 µm (i.e. 20% CCT) [33]. However, in this thesis six SMILE simulations were launched to evaluate in which way the lenticule position in the corneal thickness would influence the optical outcome: the more in depth in the corneal thickness the surgery is performed, the more the mechanical strength of the anterior portion of the cornea is preserved, but the accuracy in the dioptric correction is affected by this factor too. The lenticule positions were set, starting from the anterior surface going towards the posterior, at 20%, 30%, 40%, 50%, 60%, and 75% of CCT. Through the evaluation of anterior surface curvature variation, the dioptric corrections have been collected in Table 3.5. The highest optical dioptric correction was obtained at 20% of CCT, while going deeper in the corneal thickness meant correcting progressively less until reaching a threshold, at 50 % of CCT considering an OZ radius of 3 mm and an OZ radius of 3.5 mm and at 60% of CCT considering an OZ radius of 4 mm, in which the anterior surface curvature changes, after surgery, of a negligible value. As it can be observed in Figure 3.9 (a), the anterior surface profiles of the OZ before and after surgery, in fact, coincide for the model with ablation depth at 60% of CCT, while they are progressively moved downwards under the

pre-surgery configuration at lower ablation depths, suggesting also that the most precise fitting is obtained with the OZ radius of 4 mm. Above the threshold, the dioptric power increases, meaning that a higher refractive defect was caused, instead of being corrected, as shown in Table 3.5. This outcome is visually confirmed in Figure 3.8, where is showed that when the lenticule position is at 75% of CCT, the post-surgery mean curvature in the OZ is higher than in the pre-surgery configuration. The anterior surface profile variation shows a better applanation for the lowest depths in lenticule position (Figure 3.9 (a)). The posterior surfaces, on the other hand, move upwards under the effects of the IOP application (Figure 3.9 (b)). Note that, for models with lenticule positions at lower percentages of total CCT, the anterior surfaces move more downwards than for the models with lenticule position at higher percentages of total CCT, while the posterior surfaces move more upwards for models with lenticules at higher percentages of CCT and in models presenting the lenticules at lower percentages of CCT the posterior surfaces move less.

Lenticule Position	OZ [mm]	Mean Curvature [D]		
		pre-ablation	post-ablation	achieved correction
20 % CCT	3	41.7	40.3	-1.4
	3.5	41.7	39.4	-2.3
	4	41.8	39.1	-2.7
30 % CCT	3	41.7	40.9	-0.8
	3.5	41.7	40.1	-1.6
	4	41.8	39.7	-2.1
40 % CCT	3	41.7	41.5	-0.2
	3.5	41.7	40.9	-0.8
	4	41.8	40.4	-1.4
50 % CCT	3	41.7	42.1	0.4
	3.5	41.7	41.7	0
	4	41.8	41.2	-0.6
60 % CCT	3	41.7	42.8	1.1
	3.5	41.7	42.6	0.9
	4	41.8	42.1	0.3
75 % CCT	3	41.7	43.8	2.1
	3.5	41.7	43.9	2.2
	4	41.8	43.5	1.7

Table 3.5: Mean curvature variations in SMILE models moving the lenticule through the corneal thickness (the desired correction was set at -4 D).

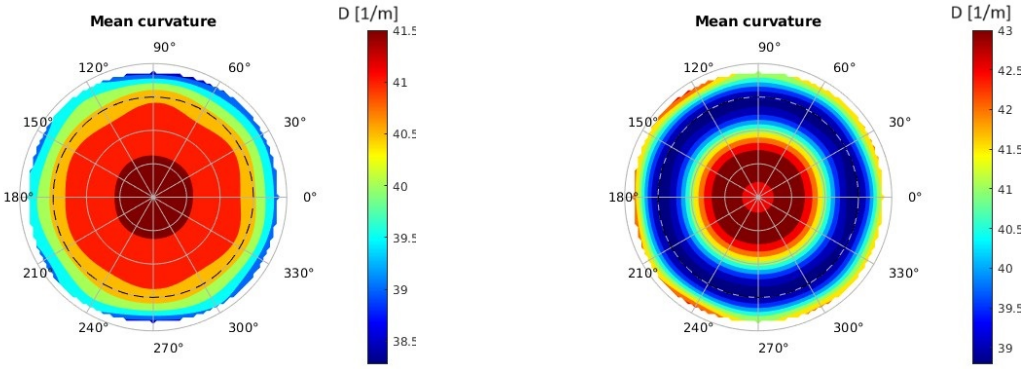

(a) (b)

Figure 3.8: Anterior surface mean curvatures in SMILE with an ablation depth of 75% of CCT. (a) Pre-surgery mean curvatures. (b) Post-surgery mean curvatures.

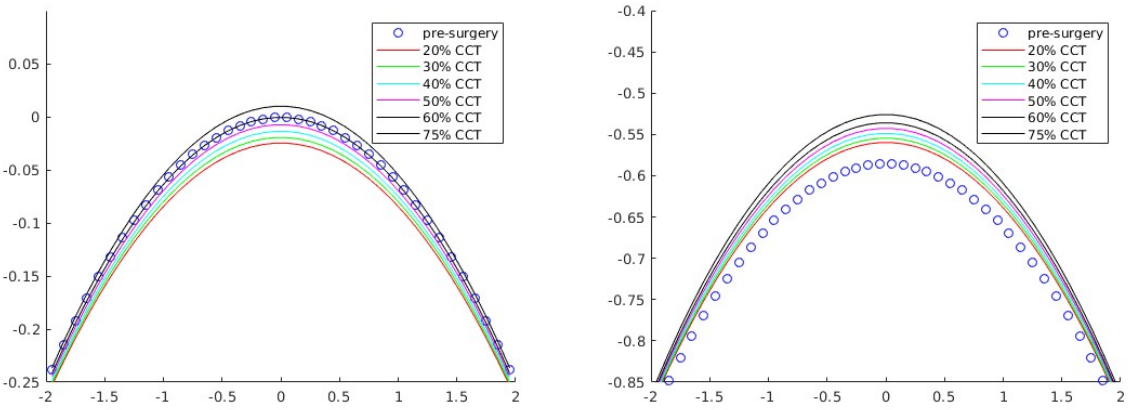

(a) (b)

Figure 3.9: Anterior surface (a) and posterior surface (b) profiles for SMILE with different lenticule positions in the corneal thickness: growing percentage of total CCT.

Furthermore, the mechanical properties were analysed through the apical displacement before and after ablation. The pre-surgical configuration is the same for each model, due to the fact that the ablation has not been performed yet. When increasing the depth at which the lenticule is extracted, the anterior surfaces move increasingly upwards (Figure 3.10(a)), until reaching the threshold at maximum 60% of CCT, beyond which the anterior surface apical coordinate of the post-surgical configuration overcomes the one of the pre-surgical configuration, confirming that the dioptric correction is not performed. Figure 3.10 (b) reports the dioptric correction reached for each case, in function of the lenticule position, for each OZ considered in the curvature analysis.

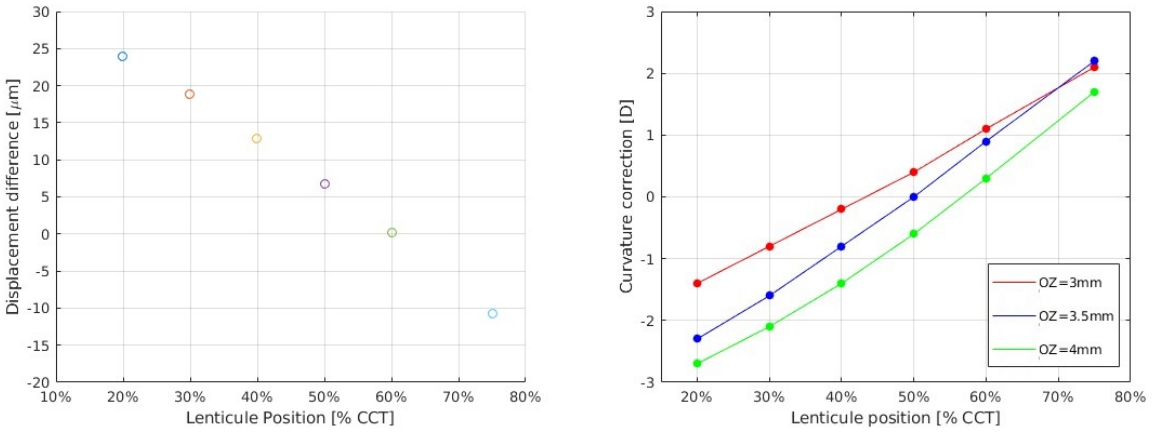

(a) (b)

Figure 3.10: Anterior surface displacement difference(in module) between pre-surgery and post-surgery configurations (a) for growing lenticule position depths in SMILE and curvature correction for each lenticule position (b).

Moreover, the maximum principal stresses' differences between the post-surgical and pre-surgical apical elements on the anterior (Table 3.6) and posterior surface (Tab 3.7) were collected, as well as the maximum principal logarithmic strain differences between the two steps. As shown, the anterior surface maximum principal stress is lower in the post-surgical than in the pre-surgical configurations (negative difference) for all the lenticule positions, except from the 75% CCT, where the post-surgical maximum principal stress is higher that the pre-surgical one. The maximum principal logarithmic strain differences on the anterior surface decrease while the lenticule is place deeper in corneal thickness and present lower values for the post-surgical configurations than the pre-surgical ones (negative differences), except from the last case (75 % CCT), where the strain difference is almost null. On the posterior surface, the maximum principal stresses increase moving down the lenticule through the thickness of the cornea, with a noticeable difference between the first and the last model of 7.45 kPa. Also the maximum principal strain differences on the posterior surface increase when moving down the lenticule. Furthermore, the anterior surface reaches low maximum principal stress and logarithmic strain values, while the posterior surface mechanical outcomes are more affected by the lenticule positioning.

Lenticule Position Depth	Anterior Surface	
	Maximum Principal Strain [-]	Maximum Principal Stress [kPa]
20% CCT	-0.0020005	-0.71
30% CCT	-0.0020147	-0.72
40% CCT	-0.0018567	-0.66
50% CCT	-0.0014619	-0.52
60% CCT	-0.0010015	-0.36
75% CCT	0.0002125	0.04

Table 3.6: Maximum principal stresses and maximum principal strain differences between the post-surgical and pre-surgical apical elements on the anterior surface.

Lenticule Position Depth	Posterior Surface	
	Maximum Principal Strain [-]	Maximum Principal Stress [kPa]
20% CCT	0.0028577	1.33
30% CCT	0.0028702	1.49
40% CCT	0.0040939	2.10
50% CCT	0.0055524	2.78
60% CCT	0.0078471	4.18
75% CCT	0.0138228	8.87

Table 3.7: Maximum principal stresses and maximum principal logarithmic strain differences between the post-surgical and pre-surgical apical elements on the posterior surface.

In particular, the maximum principal stresses distribution and the maximum principal strain distribution in the corneal section of the models respectively with a lenticule position at 20% CCT and 75 % CCT after ablation are shown in Figure 3.11: the higher stresses on the posterior surface for the second model are noticeable (Figure 3.11 (a)), as well as the deformations (Figure 3.11 (b)).

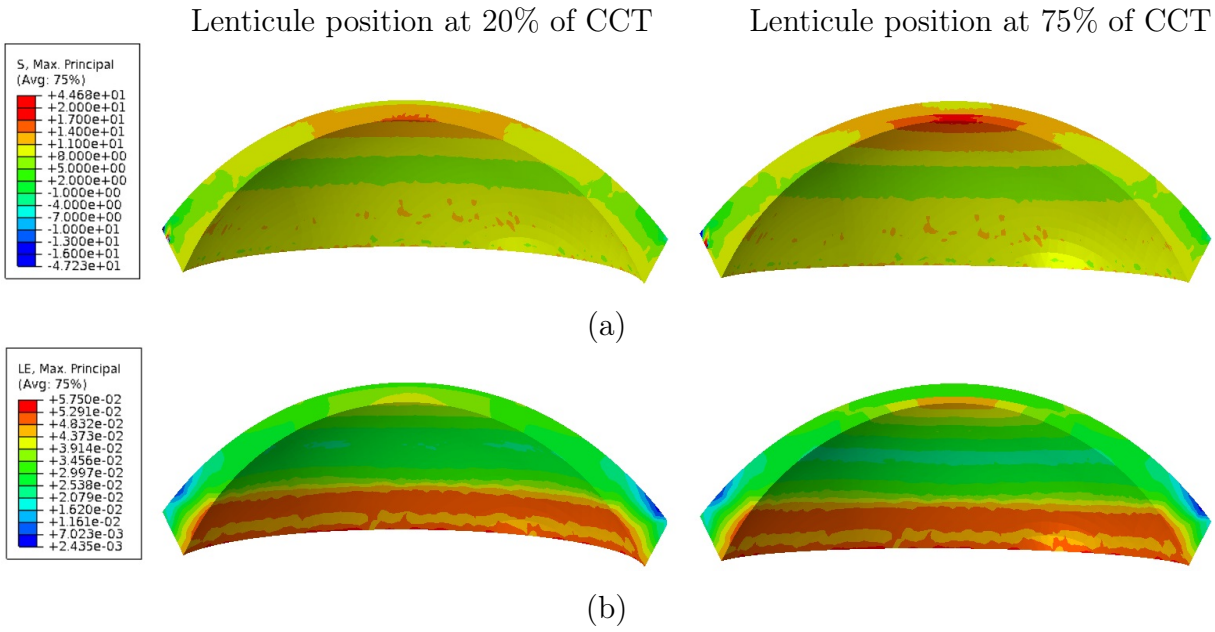

Figure 3.11: Maximum principal stress distributions (a) and maximum principal strain distributions (b) in SMILE models with lenticule position at 20 % of CCT and 75 % of CCT.

In conclusion, the chosen lenticule position for a representative SMILE model was at 20% of CCT, as it represents the current clinical standard and effectively obtains the best refractive correction, causing lower mechanical and structural changes with respect to the other tested configurations.

3.3. Dioptric corrections analysis

After selecting the most appropriate boundary conditions for both models and the correct lenticule position for SMILE, the target dioptric correction was changed, to verify whether the desired correction was achieved. In this analysis, the theoretical ablation thicknesses from literature [42] have been considered, which are also reported in Table **??**. These changes were applied to both models of PRK and SMILE surgeries. The dioptric corrections applied were -4 D, -5 D, -6 D, -7 D and -8 D. The ellipsoid-fitted mean curvatures of the anterior surface are reported in Table 3.8 for PRK and SMILE models, considering OZ radii of 3 mm, 3.5 mm and 4 mm.

Dioptric correction [D]	R(OZ) [mm]	PRK			SMILE		
		Mean Curvature [D]					
		pre-ablation	post-ablation	achieved correction	pre-ablation	post-ablation	achieved correction
-4	3	41.7	39.5	-2.2	41.7	40.3	-1.4
	3.5	41.7	38.4	-3.3	41.7	39.4	-2.3
	4	41.8	38.1	-3.7	41.8	39.1	-2.7
-5	3	41.7	39.0	-2.7	41.7	40.0	-1.7
	3.5	41.7	37.6	-4.1	41.7	38.9	-2.8
	4	41.8	37.3	-4.5	41.8	38.4	-3.4
-6	3	41.7	38.5	-3.2	41.7	39.7	-2.0
	3.5	41.7	36.8	-4.9	41.7	38.3	-3.4
	4	41.8	36.5	-5.3	41.8	37.8	-4.0
-7	3	41.7	38.0	-3.7	41.7	39.5	-2.2
	3.5	41.7	36.0	-5.7	41.7	37.8	-3.9
	4	41.8	35.7	-6.1	41.8	37.1	-4.7
-8	3	41.7	37.5	-4.2	41.7	39.2	-2.5
	3.5	41.7	35.3	-6.4	41.7	37.2	-4.5
	4	41.8	34.9	-6.9	41.8	36.5	-5.3

Table 3.8: Ellipsoid-fitted mean curvature variations and achieved dioptric corrections (i.e. difference between pre- and post- surgery curvatures) imposing different dioptric correction input for PRK and SMILE, with an OZ radius of 3, 3.5 and 4 mm.

The effective dioptric corrections obtained for PRK models were 53.5 (± 0.01)% of the desired correction for an OZ radius of 3 mm, 81.5 (± 0.02)% for an OZ radius of 3.5 mm and 88.9 (± 0.03)% for an OZ radius of 4 mm, while, for SMILE, they were 33 (± 0.02)% of the correction goal for an OZ radius of 3 mm, 56.4 (± 0.002)% for an OZ radius of 3.5 mm and 67.1 (± 0.009)% for an OZ radius of 4 mm. These data point out a better refractive outcome in PRK rather than in SMILE, for every case taken into account. Moreover, a more accurate correction is achieved considering the OZ radius of 4 mm. With the theoretical ablation profile, for PRK we reached a correction close to the target, but accuracy in the result decreases when the target correction increases, while for SMILE surgery, a worse optical outcome is achieved, even for lower corrections.

The corneal anterior and posterior profiles are reported for PRK (Figure 3.12) and SMILE (Figure 3.13).

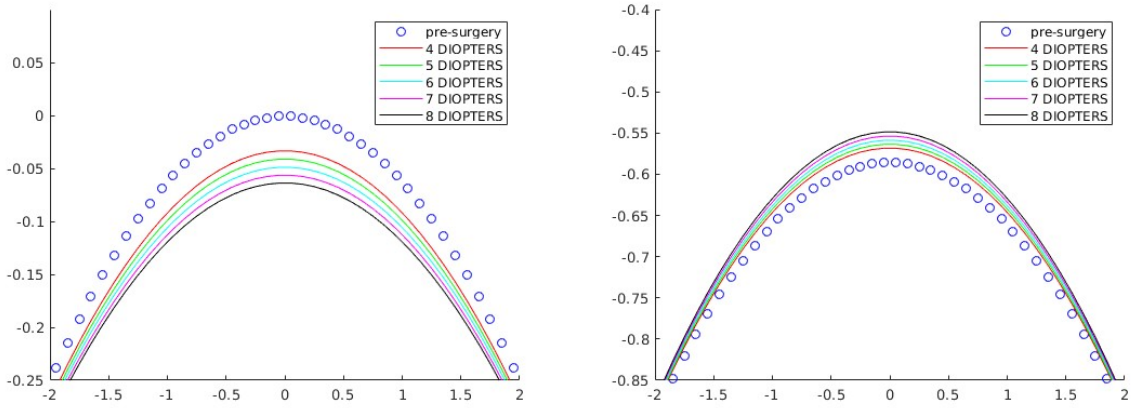

(a) (b)

Figure 3.12: Anterior surface (a) and posterior surface (b) profiles for PRK with growing dioptric corrections imposed.

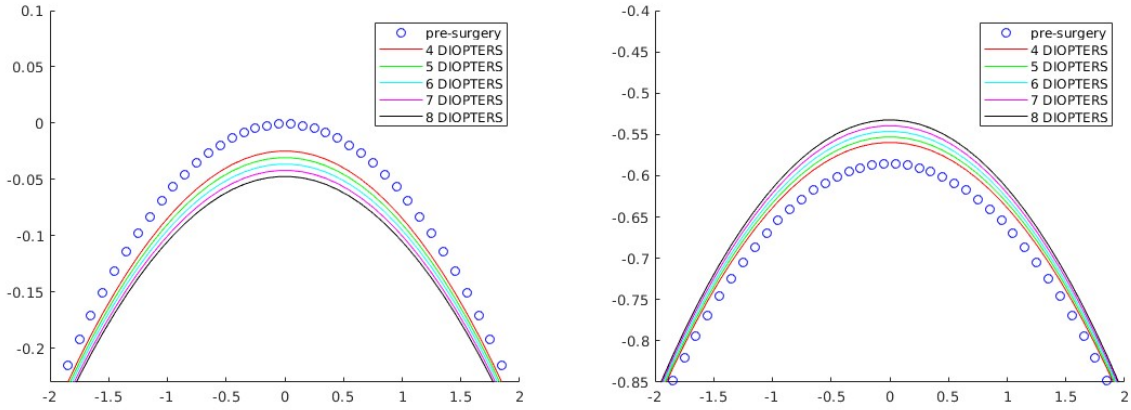

(a) (b)

Figure 3.13: Anterior surface (a) and posterior surface (b) profiles for SMILE with growing dioptric corrections imposed.

In PRK models, the apical node of the post-surgical anterior surface is selected, to trace the movement of the post-surgical anterior surface. It is important to note that the pre-surgery apical node does not coincide with the post-surgery one: after ablation, in fact, the ablation elements and their respective nodes are eliminated. As shown in Figure 3.14 (a), the post-surgical apical displacement is higher than the pre-surgical one, but, for the reason mentioned previously,they are respectively calculated on different nodes. Even though the post-surgery apical node is moving upwards (loosing a portion of the dioptric correction), it does eventually reach a lower position than the pre-surgery apical node,

resulting in a final curvature correction, as confirmed in the ablation profiles in Figure 3.12. The displacement difference increases with increasing dioptric corrections, due to the fact that the mechanical response of the corneal tissue in terms of deformations is higher due to the fact that a thicker ablation profile is removed. In Figure 3.14 (b) the dioptric corrections obtained in the models in function of the theoretical dioptric correction were plotted: considering an OZ radius of 4 mm, trying to correct lower dioptres gives more accurate simulation results than for higher requests of dioptric corrections.

In SMILE models, for growing dioptric corrections, the apical displacement difference between pre-surgery configuration and post-surgery configuration grew in module, meaning that the apical z-coordinate was moving downwards, resulting in the flattening of the anterior surface (Figure 3.15 (a)). Moreover, as for the PRK analysis, in Figure 3.14 (b) the dioptric corrections obtained in the models in function of the theoretical dioptric correction were plotted. As can be seen, the higher myopic correction is requested, the lower dioptric correction is achieved. As the corneal thickness decreases in the post-surgery configuration, while the deformation is greater.

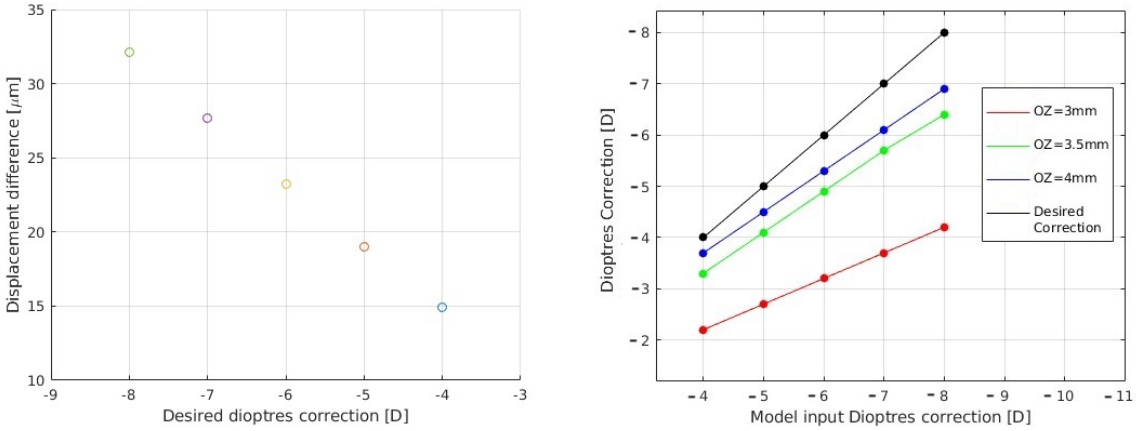

(a) (b)

Figure 3.14: Anterior surface pre-surgery apical displacement displacement difference (a) and theoretical vs actual dioptres correction (b) for PRK.

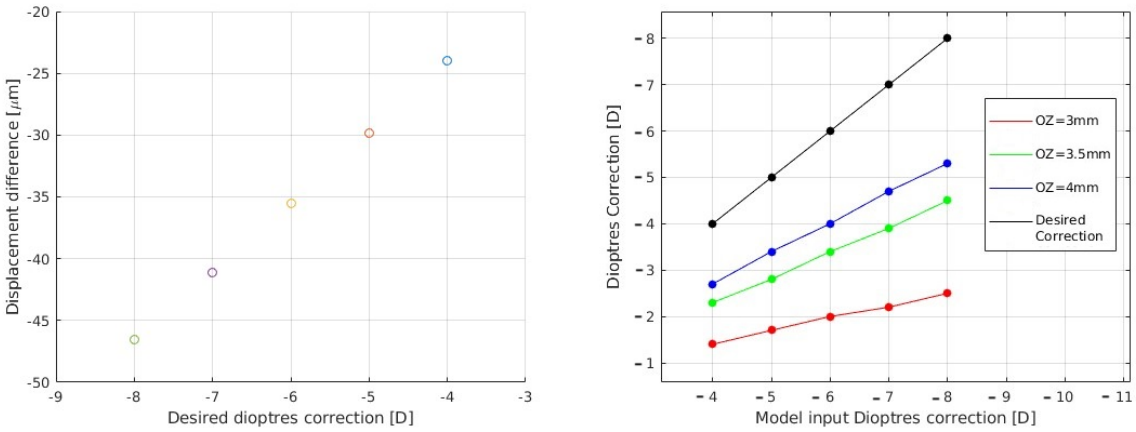

(b) (b)

Figure 3.15: Anterior surface pre-surgery apical displacement displacement difference (a) and theoretical vs actual dioptres correction (b) for SMILE.

Since the desired correction was not achieved with the numerical simulations, the ablation depths applied in the clinic were investigated: for SMILE surgery, a 10 % is currently added to the refractive goal in the clinics. To verify which correction could be achieved with the higher corrections, 5 SMILE simulations with different dioptric correction (ranging from -1 D to -5 D) and the ablation thickness reported in Table 2.4 were run, with the following curvature results, considering an OZ of 4 and 4.5 mm (Table 3.9):

Dioptric Correction Input [D]	Desired Dioptric Correction [D]	R(OZ) [mm]	Mean Curvature [D]		
			pre-ablation	post-ablation	achieved correction
-1.1	-1	4	41.7	41.5	-0.2
		4.5	41.7	40.2	-1.5
-2.2	-2	4	41.7	40.6	-1.1
		4.5	41.7	39.4	-2.3
-3.3	-3	4	41.7	39.8	-1.9
		4.5	41.7	38.5	-3.2
-4.4	-4	4	41.7	39.1	-2.6
		4.5	41.7	37.8	-3.9
-5.5	-5	4	41.7	38.4	-3.3
		4.5	41.7	37.1	-4.6

Table 3.9: Ellipsoid-fitted mean curvatures and achieved dioptric corrections for SMILE models, based on the clinical ablation depths.

As shown, the carried out analysis considering an OZ radius of 4.5 mm brings the most accurate results in dioptric correction, while the lower OZ radius provides lower dioptric corrections than the desired ones (Figure 3.16).

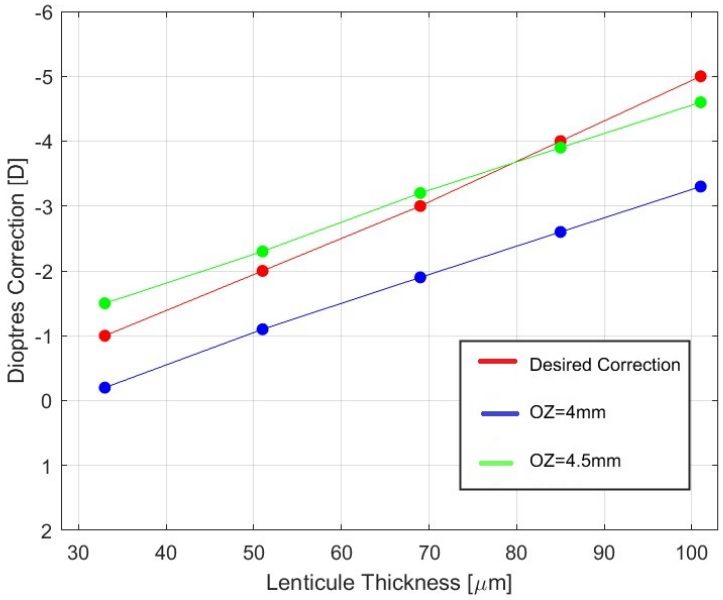

Figure 3.16: Desired dioptric correction VS actual dioptric correction obtained in SMILE models, in function of the lenticule thickness [µm], built based on clinical data, imposing a 10% more of dioptric correction in the input data.

3.4. OZ radius

Varying the OZ radius parameter and leaving the other parameters constant (-4 D correction, CCT = 579 µm) gave the curvature corrections shown in Table 3.10. The lenticule thicknesses depend on the OZ value and are showed in Table 2.2. In this case, for the optical analysis, different OZ were considered and the highest dioptric correction was reached for an OZ radius of 4 mm for the first two cases, while for the third case, the highest correction was reached considering an OZ of 5 mm, due to the fact that the optical zone of the ablation was bigger (4 mm).

OZ Radius [mm]	R(OZ) [mm]	Mean Curvature [D]					
		PRK			SMILE		
		pre-ablation	post-ablation	achieved correction	pre-ablation	post-ablation	achieved correction
3	3	41.7	39.5	-2.2	41.7	40.3	-1.4
	3.5	41.7	38.4	-3.3	41.7	39.4	-2.3
	4	41.8	38.1	-3.7	41.8	39.1	-2.7
	4.5	41.8	38.5	-3.3	41.8	39.3	-2.5
	5	41.8	39.2	-2.6	41.8	39.8	-2
3.5	3	41.8	39.4	-2.4	41.8	40.4	-1.4
	3.5	41.7	39.4	-2.3	41.7	40.5	-1.2
	4	41.7	38.5	-3.2	41.7	39.8	-1.9
	4.5	41.7	38.1	-3.6	41.7	39.3	-2.4
	5	41.8	38.4	-3.4	41.8	39.4	-2.4
4	3	41.8	39.5	-2.3	41.8	40.5	-1.3
	3.5	41.8	39.5	-2.3	41.8	40.5	-1.3
	4	41.8	39.5	-2.3	41.8	40.6	-1.2
	4.5	41.8	38.8	-3.0	41.8	40.1	-1.7
	5	41.8	38.3	-3.5	41.8	39.6	-2.2

Table 3.10: Curvature variations and achieved dioptric corrections varying the OZs in PRK and SMILE.

3.5. Central corneal thickness

To evaluate the influence of the corneal thickness on the opto-mechanical outcome of the models, different CCTs were considered. The values of 500 µm, 510 µm, 520 µm, 530 µm, 540 µm, 550 µm, 560 µm, 570 µm, 580 µm, 590 µm and 600 µm were taken into account both for PRK and SMILE. The other parameters were: 3 mm OZ radius for ablation, -4 D of desired dioptric correction and ablation depth of 47.6 µm. The dioptric correction outcomes of the simulations are shown in Table 3.11 for PRK and SMILE.

CCT [µm]	R(OZ) [mm]	PRK			SMILE		
		Mean Curvature [D]					
		pre-ablation	post-ablation	achieved correction	pre-ablation	post-ablation	achieved correction
500	3	41.7	39.8	-1.9	41.7	40.8	-0.9
	3.5	41.7	38.7	-3	41.7	39.9	-1.8
	4	41.8	38.4	-3.4	41.8	39.4	-2.4
510	3	41.7	39.8	-1.9	41.7	40.7	-1.0
	3.5	41.7	38.6	-3.1	41.7	39.8	-1.9
	4	41.8	38.4	-3.4	41.8	39.4	-2.4
520	3	41.7	39.7	-2.0	41.7	40.7	-1.0
	3.5	41.7	38.6	-3.1	41.7	39.8	-1.9
	4	41.8	38.3	-3.5	41.8	39.4	-2.4
530	3	41.7	39.7	-2.0	41.7	40.6	-1.1
	3.5	41.7	38.6	-3.1	41.7	39.7	-2.0
	4	41.8	38.3	-3.5	41.8	39.3	-2.5
540	3	41.7	39.6	-2.1	41.7	40.6	-1.1
	3.5	41.7	38.5	-3.2	41.7	39.6	-2.1
	4	41.8	38.3	-3.5	41.8	39.2	-2.6
550	3	41.7	39.6	-2.1	41.7	40.5	-1.2
	3.5	41.7	38.5	-3.2	41.7	39.6	-2.1
	4	41.8	38.2	-3.6	41.8	39.2	-2.6
560	3	41.7	39.6	-2.1	41.7	40.5	-1.2
	3.5	41.7	38.4	-3.3	41.7	39.5	-2.2
	4	41.8	38.2	-3.6	41.8	39.2	-2.6
570	3	41.7	39.5	-2.2	41.7	40.4	-1.3
	3.5	41.7	38.4	-3.3	41.7	39.5	-2.2
	4	41.8	38.2	-3.6	41.8	39.1	-2.7
580	3	41.7	39.5	-2.2	41.7	40.3	-1.4
	3.5	41.7	38.4	-3.3	41.7	39.5	-2.2
	4	41.8	38.1	-3.7	41.8	39.1	-2.7

CCT [µm]	R(OZ) [mm]	PRK			SMILE		
		Mean Curvature [D]					
		pre-ablation	post-ablation	achieved correction	pre-ablation	post-ablation	achieved correction
590	3	41.7	39.5	-2.2	41.7	40.3	-1.4
	3.5	41.7	38.3	-3.4	41.7	39.4	-2.3
	4	41.8	38.1	-3.7	41.8	39.0	-2.8
600	3	41.7	39.4	-2.3	41.7	40.3	-1.4
	3.5	41.7	38.3	-3.4	41.7	39.4	-2.3
	4	41.8	38.1	-3.7	41.8	39.0	-2.8

Table 3.11: Ellipsoid-fitted curvature variations and achieved dioptric corrections imposing different CCTs for PRK and SMILE, with an OZ radius of 3, 3.5 and 4 mm.

The more the CCT is high, the more the curvature differences increase, with a maximum difference of 0.3-0.4 D among the fitting radii for PRK. In SMILE models the maximum differences are 0.4-0.5 D for the same fitting radii. These results mean that a slightly higher dioptrical correction is achieved when increasing the CCT, even though the difference between the results is low. This suggests that the central corneal thickness has a small influence on the optical result.

The Figure 3.17 shows the curvature correction variations in function of the CCT values, both for PRK models and SMILE models: the OZ radius of 4 mm guarantees better results for both models in terms of dioptric correction: given that the goal was to correct -4 D, PRK simulation reached a good optical correction (-3.7 D), while the optical outcome of SMILE was poorer (-2.8 D).

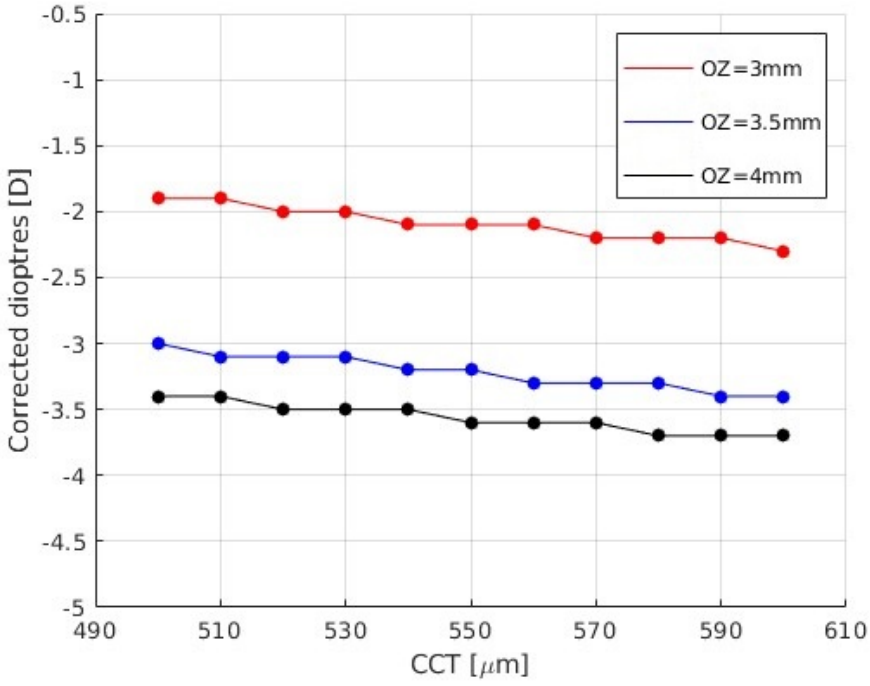

(a)

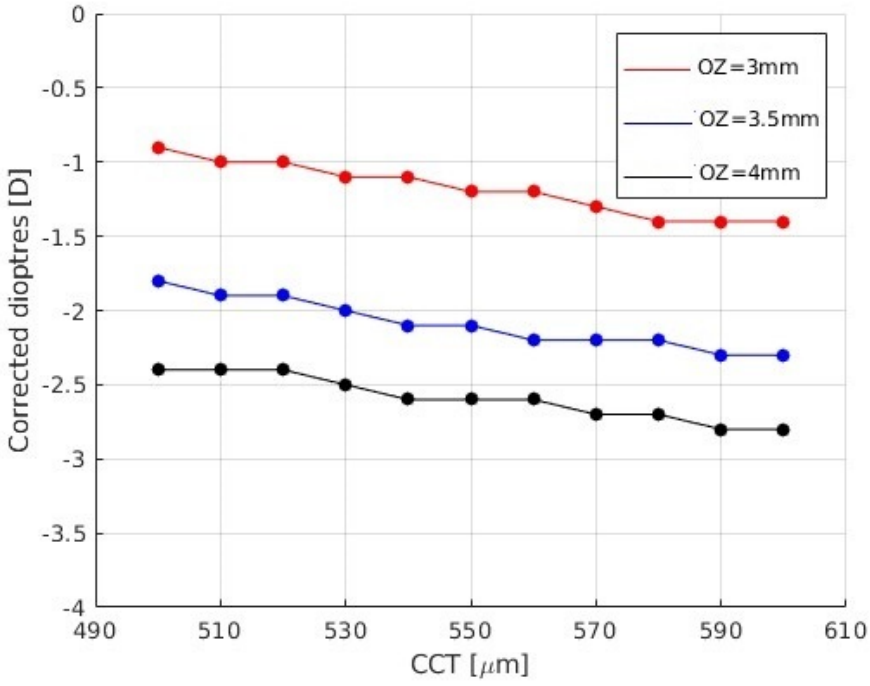

(b)

Figure 3.17: Dioptric correction variation depending on CCT for PRK (a) and SMILE (b) models. The desired dioptric correction is -4 D.

Anterior surface apical nodes displacement difference between pre-surgical and post-surgical configurations are shown in Figure 3.18 (a) for PRK and (b) for SMILE. The graphs show that the CCT does not highly affect the displacement of the anterior surface in both the models. The difference between the post-surgical displacement and the pre-surgical displacement, in fact, shows a variation in the range of (19.96±2.5) µm for PRK and (22.17±2.4) µm, which is negligible.

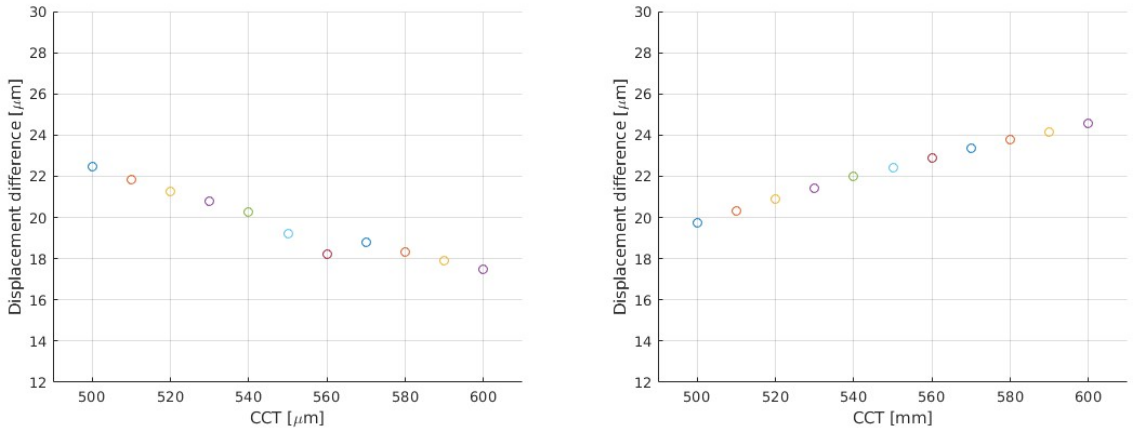

(a) (b)

Figure 3.18: Anterior surface apical nodes displacement difference between pre-surgical and post-surgical configurations in module for PRK (a) and SMILE (b) with different CCTs.

A selection of 5 elements on the anterior and posterior surfaces was made and the stress and strain values were averaged (both for PRK and SMILE, for each CCT considered). The results confirm that the CCT does not influence the mechanics of the post-surgical configuration (Figure 3.19), as the difference between pre-surgery and post-surgery maximum principal stresses and maximum principal logarithmic strain can be considered almost constant for all the CCTs models.

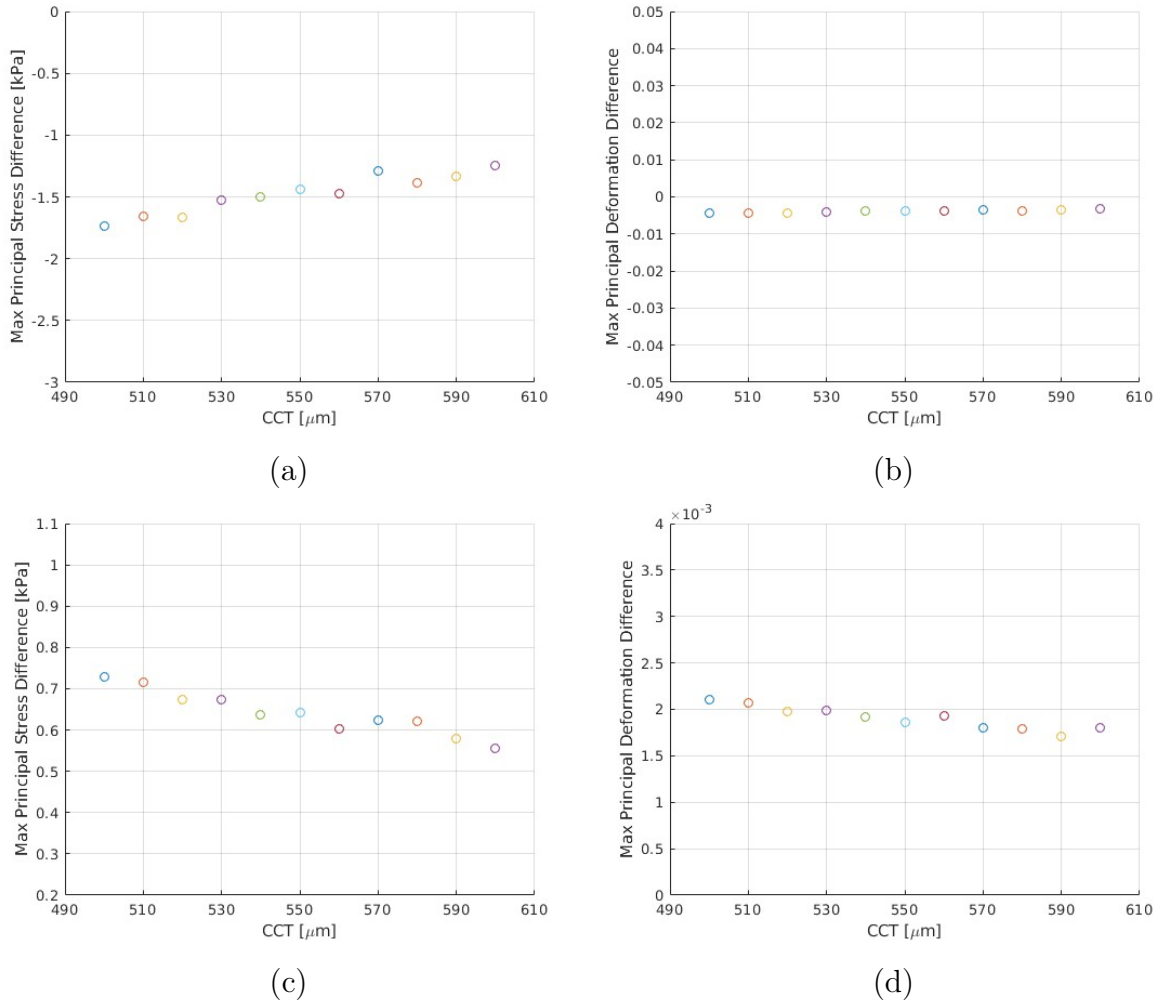

Figure 3.19: Anterior surface maximal principal stress (a) and logarithmic strain differences between post-surgery and pre-surgery configurations (b) for PRK and anterior surface maximal principal stress (c) and logarithmic strain difference between post-surgery and pre-surgery configurations (d) for SMILE for varying CCTs.

3.6. Full-Factorial analysis

A biomechanical sensitivity analysis was conducted in order to determine the parameters that mostly influenced the final outcome of the laser refractive surgery simulations.
For sake of simplicity, given the higher accuracy of the results for a radius of 4 mm for the ellipsoid surface fitting, the optical results considering this radius will be showed from now on. In Table 3.12, the parameters for which the dioptric corrections obtained are comparable to the desired one (-4 D) are reported. As it can be seen, a larger number of PRK models (out of a total of 32) reach the desired correction if compared to SMILE. The material parameters combination through which the higher dioptres correction is reached

is: C_{10}=15 kPa, k_1=30 kPa, k_2=600 kPa (with an IOP of 20 mmHg and for both the CCTs considered in PRK and SMILE).

Model	C_{10} [kPa]	k_1 [kPa]	k_2 [kPa]	IOP [mmHg]	CCT [µm]	achieved correction [D]
PRK	15	30	600	20	600	-4.18
	15	10	600	20	600	-4.07
	45	30	600	12	600	-3.97
	15	30	600	12	600	-3.94
	45	10	600	12	600	-3.93
	45	30	200	12	600	-3.96
	45	10	200	12	600	-3.93
	15	30	600	20	490	-4.12
	15	10	600	20	490	-4.03
SMILE	15	30	600	20	600	-3.98
	15	10	600	20	600	-3.92
	15	30	600	20	490	-3.95

Table 3.12: Highest dioptric corrections (i.e. ellipsoid-fitted curvature variations) reached in PRK and SMILE models and respective material and geometrical parameters.

For PRK surgery, the corrected dioptres were mainly affected by the variation of the thickness of the model and, in particular, higher thicknesses provide higher dioptric corrections (Figure 3.20 (a)). For SMILE, on the other hand, the correction variation among different models is mainly affected by C_{10} coefficient variation and the higher dioptric corrections are reached for C_{10}=15kPa (Figure 3.20 (b)).

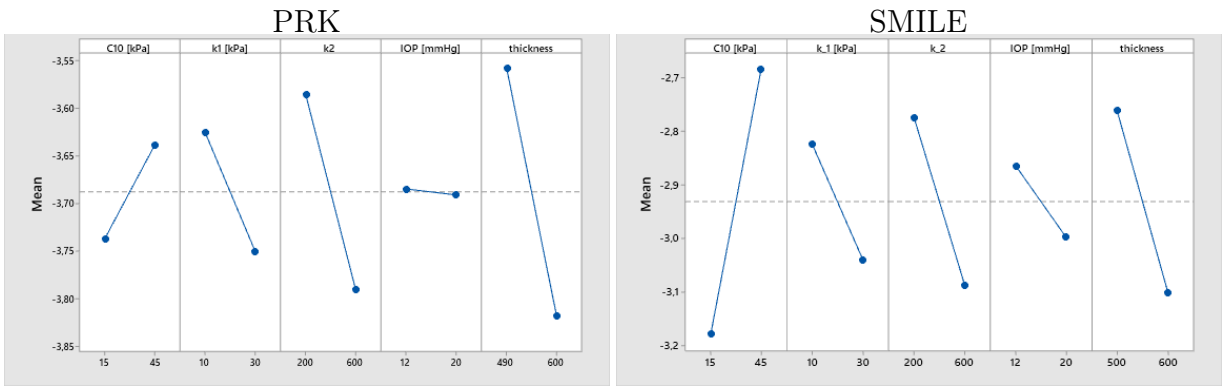

Figure 3.20: Influence of material properties, IOP and corneal thickness on the dioptric correction for PRK (a) and SMILE (b).

While the configuration before ablation (which is the same for both the PRK and SMILE models) shows a major influence on the stresses by the IOP and on deformations by the C_{10} value (Figure 3.21), after ablation, the posterior surface stresses are more affected by the influence of the IOP (Figure 3.22), as they are the surface of application of the IOP. The anterior surfaces stresses resent of the IOP too, and are also mainly affected by the C_{10} coefficient.

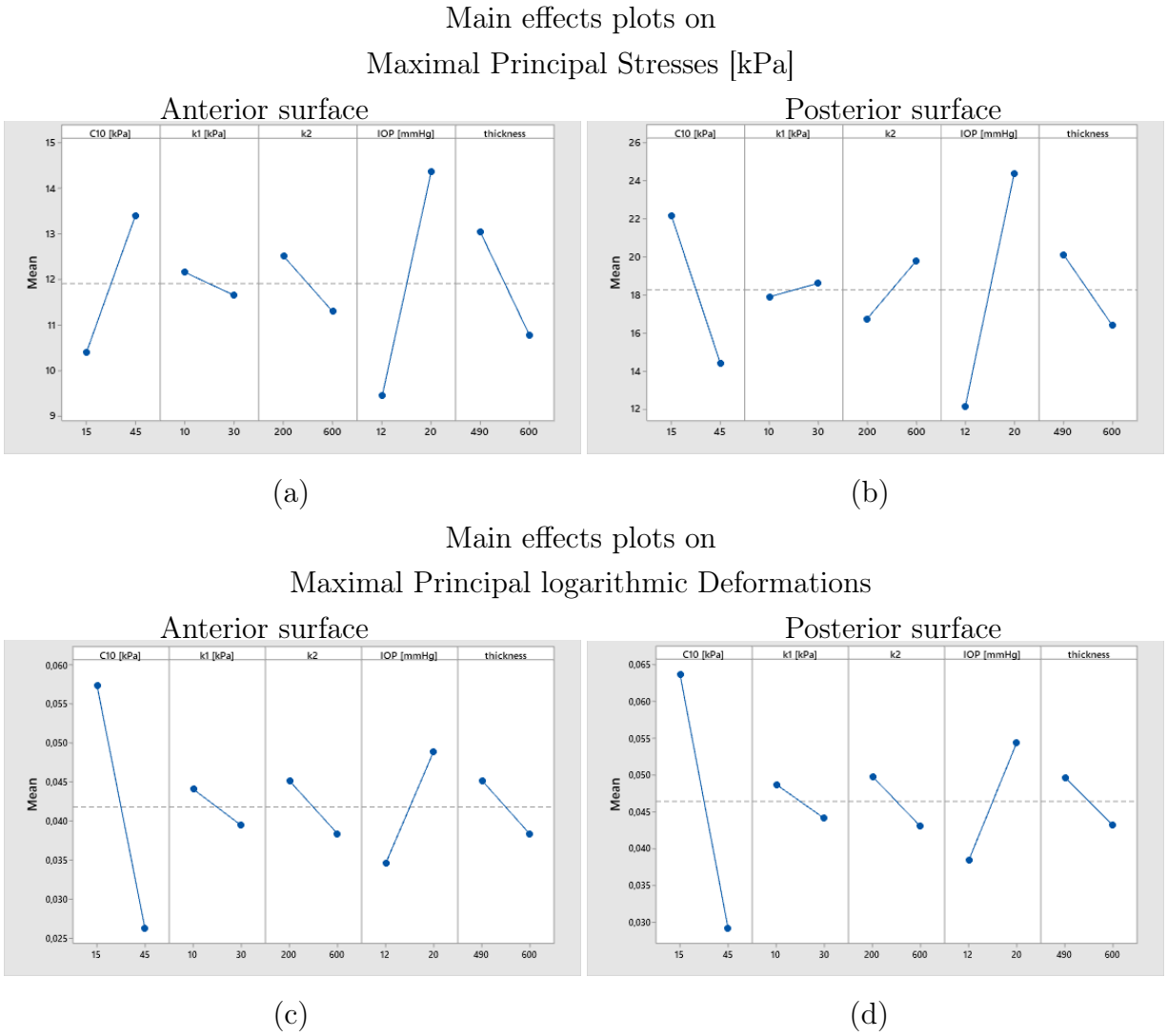

Figure 3.21: Main effects plots: influence of material properties, IOP and corneal thickness on the stresses (a), (b) and deformations (c), (d) of anterior (a), (c) and posterior (b), (d) surfaces before performing ablation.

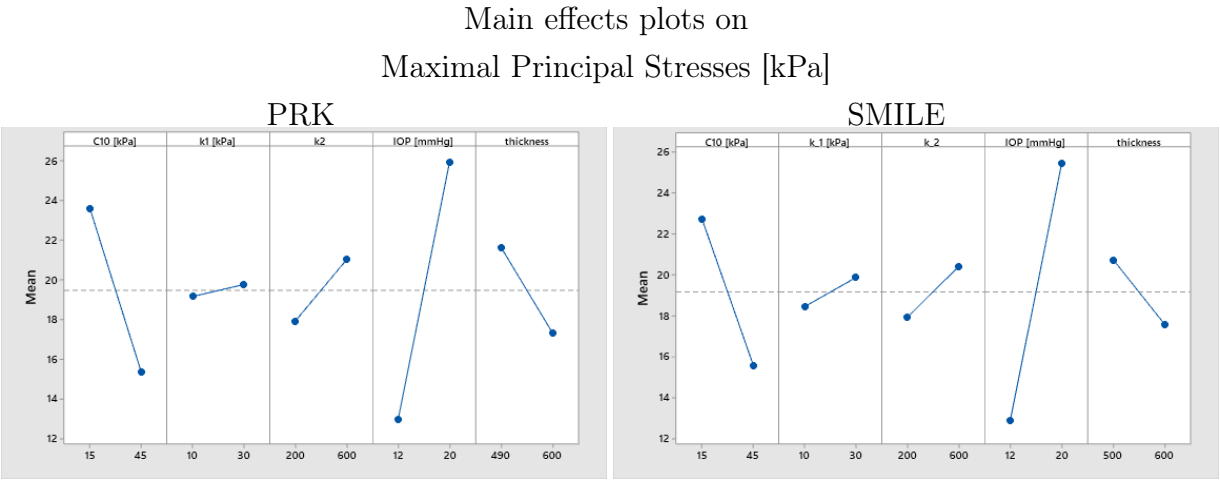

(a) (b)

Figure 3.22: Main effects plots: influence of material properties, IOP and corneal thickness on the stresses on the posterior surfaces of PRK (a) and SMILE (b) after performing ablation.

3.7. Montecarlo analysis

The analysis results show that varying the CCT and the mechanical properties of the corneal tissue influences the dioptric correction obtained, given a certain input of desired correction (in this case it was set on -4 D). The maximum dioptric corrections is obtained for the data: C_{10} = 17.37 kPa, k_1 = 28.42 kPa, k_2 = 494.42 kPa for all CCTs cases and, in particular, the highest dioptric correction is reached for CCT=600 µm (-3.9 D in PRK and -3.3 D in SMILE). The minimum correction is reached for C_{10} = 23.09 kPa, k_1 = 13.56 kPa, k_2 = 319.21 kPa for all CCTs cases, but more specifically, the lowest dioptric correction is for CCT=500 µm (-3.2 D in PRK and -2.1 D in SMILE). A more accurate correction is reached in models with an higher CCT. The PRK models reach, in general, an higher dioptric correction than the SMILE models for the same ablation profile. Moreover, through a linear regression, a function relating the effective dioptric corrections and the CCTs has been traced, using the mean values obtained in each group of simulations with the same CCTs (Figure 3.23). The linear relations and the standard deviations are reported in Equation 3.1, 3.2 for PRK and SMILE respectively.

$$\begin{gathered} \mathrm{D\ (PRK)} = -0.0030\,\mathrm{CCT} - 1.9143 \\ \text{standard deviation} = 0.1125 \end{gathered} \tag{3.1}$$

$$\text{D (SMILE)} = -0.0038\,\text{CCT} - 0.6038 \qquad (3.2)$$
$$\text{standard deviation} = 0.1408$$

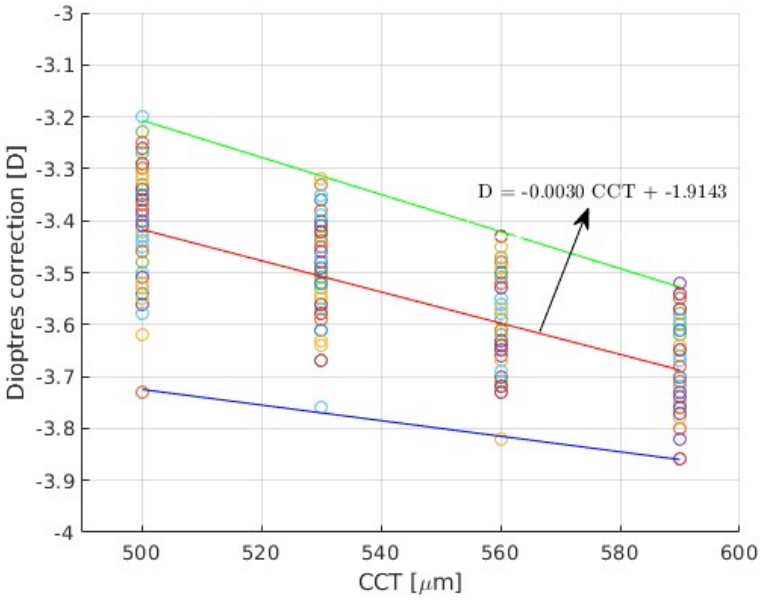

(a)

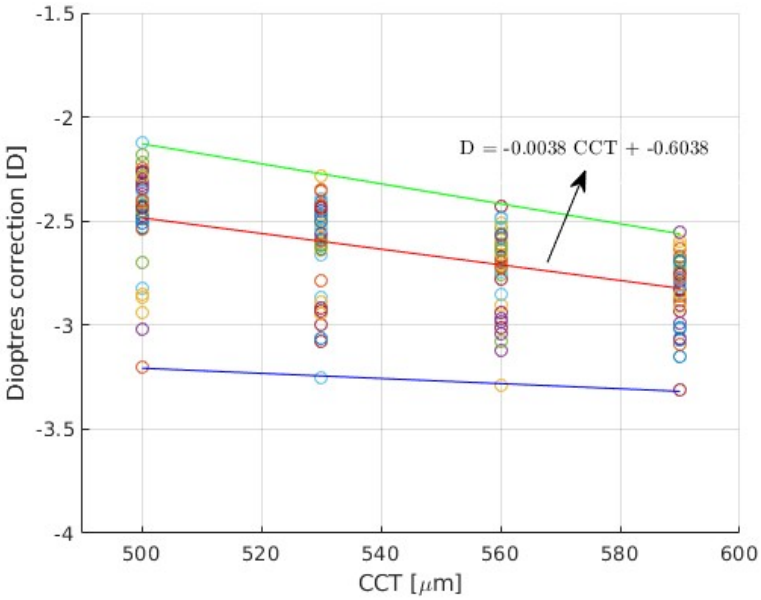

(b)

Figure 3.23: Dioptric correction variation depending on the CCT, with different material parameters, determined by a linear regression for PRK (a) and SMILE (b).

3.8. Patient-specific models

The two models simulating the PRK and SMILE surgeries of a specific patient were compared from an optical and mechanical point of view.

The displacement differences and the maximum principal strain and stress differences between the pre- and the post-surgical configurations are reported respectively in Figure 3.24, 3.25 and 3.26. From Figure 3.24, we can appreciate how the two surgeries' simulations behave in a very different way: in PRK, the removal of the ablation tissue causes a small upward displacement, due to the action of the IOP; in SMILE surgery, instead, the anterior surface moves downwards, while the posterior moves upwards, reaching higher values of displacement with respect to PRK simulation. This is due to the fact that IOP is acting directly onto the posterior surface and the removal of the lenticule from the corneal thickness causes a discontinuity in corneal tissue, so that the stresses can redistribute on a smaller volume with respect to PRK, where the tissue is removed from the anterior surface. This observation is confirmed by the stress distribution in SMILE simulation (Figure 3.26 (b)), where the stresses are higher at the posterior surface, while the anterior surface is unloaded. In PRK (Figure 3.26 (a)) stresses are more homogeneously distributed throughout the whole corneal thickness. As a consequence of the lenticule extraction, corneal structure in SMILE surgery is subjected to higher mechanical imbalances that cause higher levels of deformations, with respect to PRK, that preserves much more the mechanical integrity of the whole tissue.

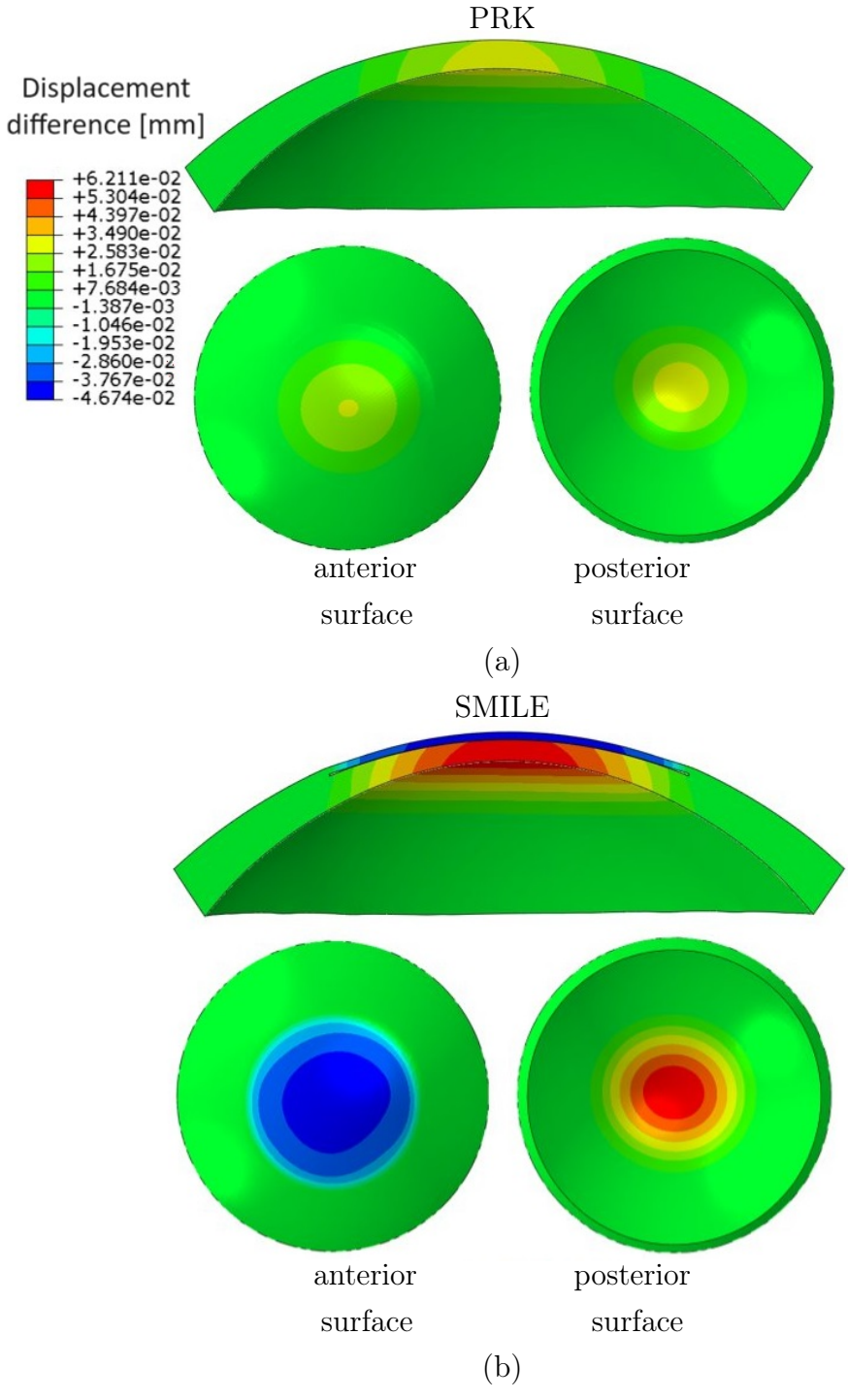

Figure 3.24: Maximum principal displacement difference in PRK (a) and SMILE (b) patient-specific models.

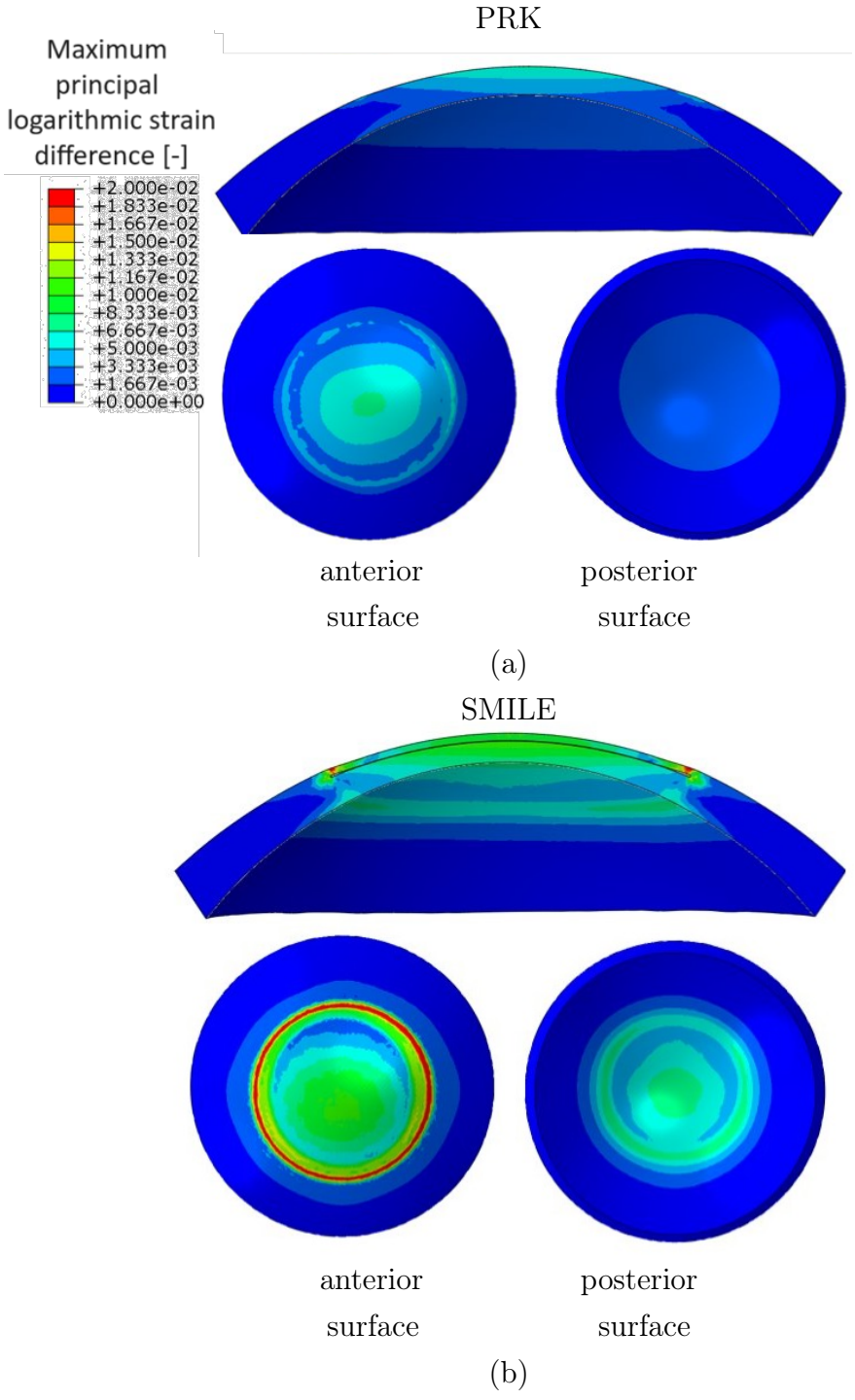

Figure 3.25: Maximum principal strain difference in PRK (a) and SMILE (b) patient-specific models.

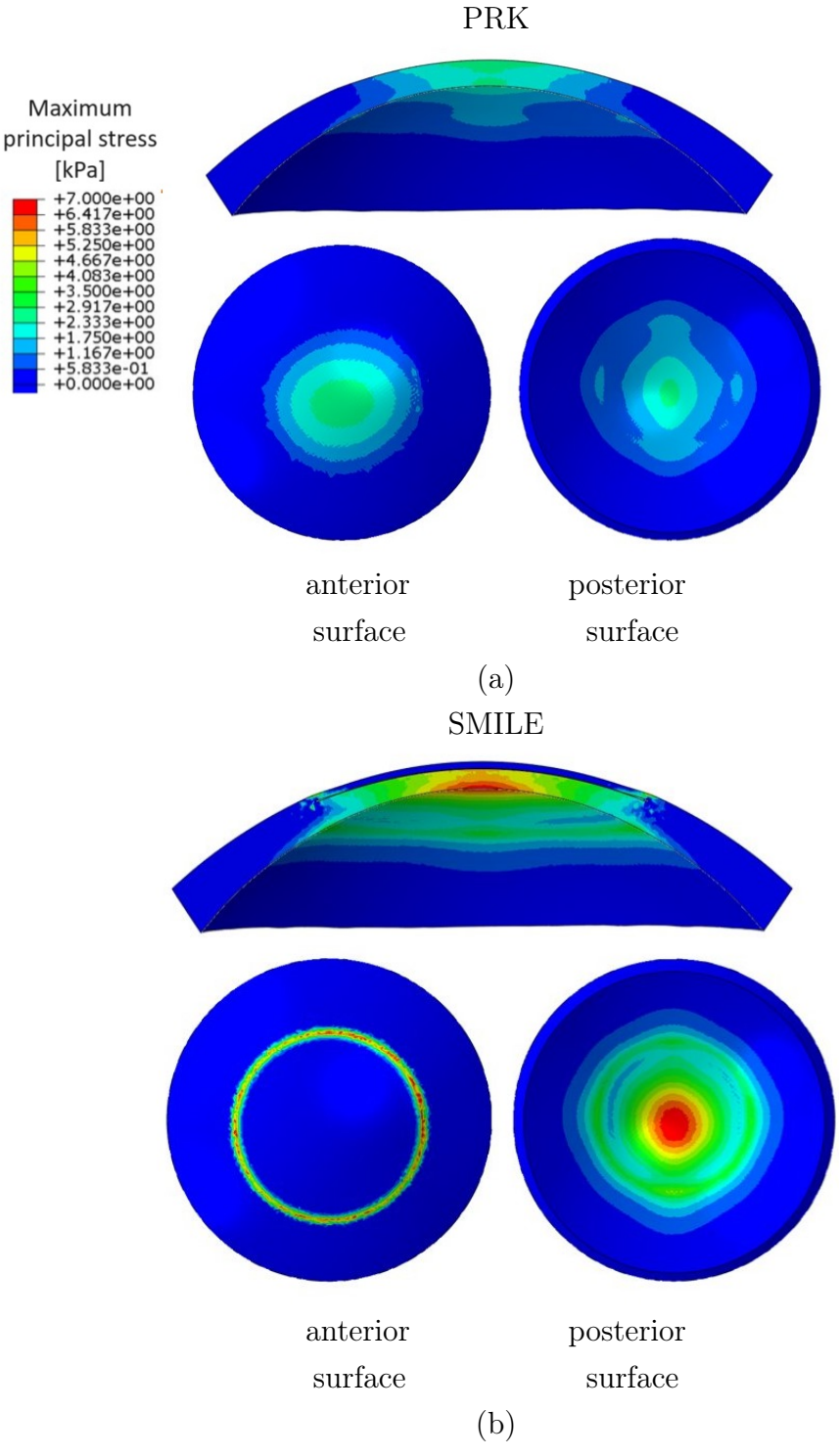

Figure 3.26: Maximum principal stress difference in PRK (a) and SMILE (b) patient-specific models.

Moving to the optical analysis, at first we evaluated if the geometrical model was reflecting the patient's initial optical characteristics. In Figure 3.27, the pre-surgery Pentacam

derived sagittal map (a) and the anterior surface of the patient-specific model (b) are reported. The sagittal curvature map of the anterior surface of the model confirms that the patient's initial optical properties are accurately reproduced by the numerical model.

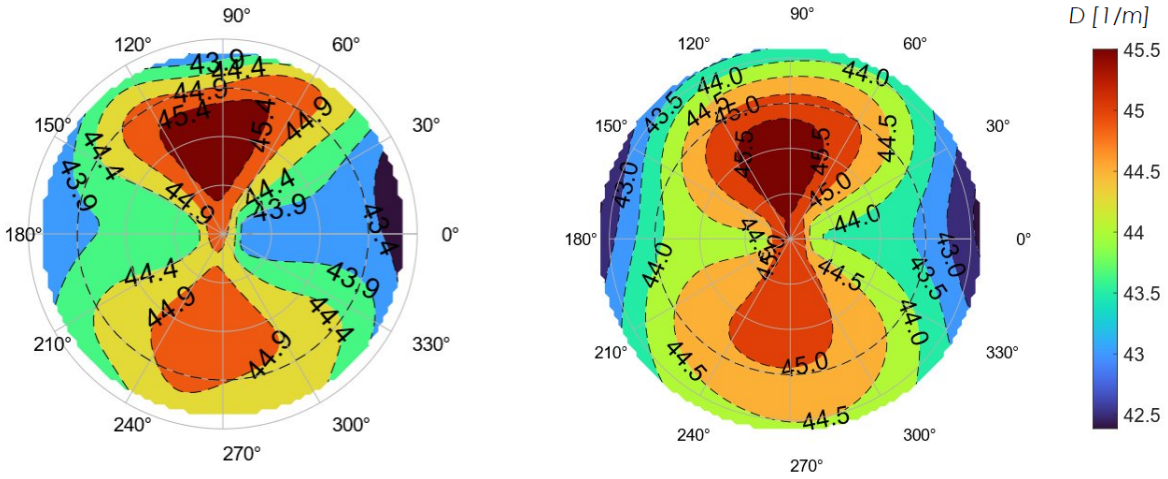

Figure 3.27: Pentacam-derived patient anterior surface sagittal curvature map (a) and anterior surface sagittal curvature map of the patient-specific model(b).

The curvature variations are reported in Table 3.14 and Table 3.15, calculated by means of the elliptic-fitted curvature with an OZ radius of 4.5 mm. Since we are dealing with patient-specific models, we report more in detail the specifics of the anterior surface of the two models, i.e. the principal curvatures K1 and K2, the sphere or mean curvature Km, the cylinder C or astigmatism and the astigmatism axis α, that indicates the orientation of the astigmatic defect. In Table 3.13, the pre- and post-surgical Pentacam data of the patient who underwent PRK surgery are reported and will be used as refractive target to validate our simulations from an optical point of view.

The first two patient-specific simulations for PRK and SMILE were run with the same material constants used throughout all the simulations performed in this thesis (C_{10} = 30 kPa). While PRK simulation was closer to the actual correction achieved on the patient subjected to the real surgery (post-surgical Km = 40.9 D with respect to Pentacam Km = 40.5 D, see Tables 3.13-3.14), SMILE simulation reached a poor optical outcome (post-surgical Km = 41.9 D).

Consequently, a final analysis varying the C_{10} parameter was conducted (Tables 3.14-3.15), as already explained in Section 2.9. These results show that a softer material (C_{10} =15 kPa) achieves the surgery dioptric target, providing the actual diopric correction: while for PRK the difference in correction is not particularly high between the different

material models considered (even though the highest dioptric correction is achieved for the softest material), for SMILE the difference is more noticeable, suggesting that the chosen material has a higher influence on the optical performance of this surgery.

Pentacam data		
	pre-ablation	post-ablation
K1 [D]	43.8	40.1
K2 [D]	45.5	41.0
Km [D]	44.6	40.5
C [D]	1.6	0.9
α [°]	0.9	21.6

Table 3.13: K1, K2, Km, C, α values derived from the Pentacam data of the patient.

PRK						
	$C_{10} = 30$ kPa		$C_{10} = 60$ kPa		$C_{10} = 15$ kPa	
	pre-ablation	post-ablation	pre-ablation	post-ablation	pre-ablation	post-ablation
K1 [D]	44.5	40.3	44.5	40.0	44.5	39.8
K2 [D]	46.1	41.8	46.1	41.4	46.1	41.2
Km [D]	45.3	41.1	45.3	40.7	45.3	40.5
C [D]	1.6	1.4	1.6	1.4	1.6	1.4
α [°]	0.1	179.6	0.2	179.5	0.2	179.6

Table 3.14: K1, K2, Km, C, α values for PRK patient-specific model, varying the C_{10} coefficient.

SMILE						
	C_{10} = 30 kPa		C_{10} = 60 kPa		C_{10} = 15 kPa	
	pre-ablation	post-ablation	pre-ablation	post-ablation	pre-ablation	post-ablation
K1 [D]	44.5	40.6	44.5	40.2	44.5	39.1
K2 [D]	46.1	42.1	46.1	41.7	46.1	40.5
Km [D]	45.3	41.3	45.3	40.9	45.3	39.8
C [D]	1.6	1.5	1.6	1.5	1.6	1.5
α [°]	0.1	179.9	0.2	179.9	0.2	179.8

Table 3.15: K1, K2, Km, C, α values for SMILE patient-specific model, varying the C_{10} coefficient.

The optical performance of the simulation does not vary linearly with the variation of the material constants: in fact, the lowest correction was achieved for the medium case (C_{10} = 30 kPa) in both models, while, in PRK, the highest correction was achieved for the softest case (C_{10} = 15 kPa) and in SMILE, the for the stiffest case (C_{10} = 60 kPa) determined a slight undercorrection and the softest a slight overcorrection. To explain this behavior, we calculated the curves of the maximum principal logarithmic strain vs. maximum principal stress for the apical zone of the anterior and posterior surfaces for both PRK and SMILE simulations (Figures 3.28 (a) and (b), 3.29 (a) and (b), respectively) and we report the differences, only due to the ablation step (i.e. the section of the curves between the two circles, Figures 3.28,3.29), in stresses and strains at the anterior and posterior surfaces in Tables 3.16,3.17. In PRK simulations, if we look at the red curve of the softest case in Figure 3.28, we can see that the surgery causes the lowest deformation, given that at the end of the pressurization step the geometry is already highly deformed, and this is confirmed by the strain value in Table 3.16. Then, the stiffest case shows a slightly higher strain difference value, that corresponds to a lower refractive correction (Table 3.14). Finally, the intermediate case is the one characterized by the higher strain difference, causing to achieve the lowest refractive correction among the three cases. Moreover, it is important to notice that in the softest case (Figure 3.28 (b), red curve), the fibers at the posterior surface are highly working, causing the deformation due to the surgery to be the lowest.

For SMILE surgery, it is more complex to explain the influence of the material model onto the refractive outcome. As already underlined, in SMILE surgery we have a different behavior at the anterior and posterior surfaces, due to the discontinuity introduced by

the lenticule extraction: while the posterior surface is more loaded due to less volume available for the stresses to redistribute, the anterior surface undergoes a relaxation and the stresses decrease: this is the reason why the black circle in Figure 3.29 (a), that represents the end of the simulation, has 'come back' in the stress-strain curve. Thus, the amount of this 'relaxation' with respect to the pressurized configuration will determine the final optical outcome achieved by the simulation. While in PRK the differences in the optical outcome of the three simulations are low (maximum difference in the post-surgical curvature 0.6 D, Table 3.14), in SMILE it is possible to notice much higher differences depending on the selected material properties (maximum difference in the post-surgical curvature 1.9 D, Table 3.14)). As already said, also for SMILE simulation, the softest case gave the more accurate and correct refractive correction.

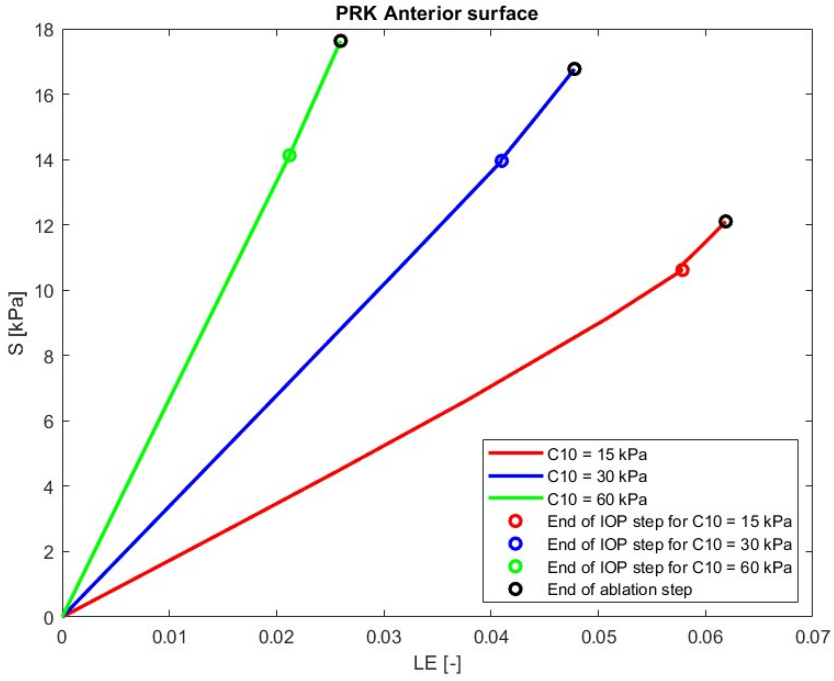

(a)

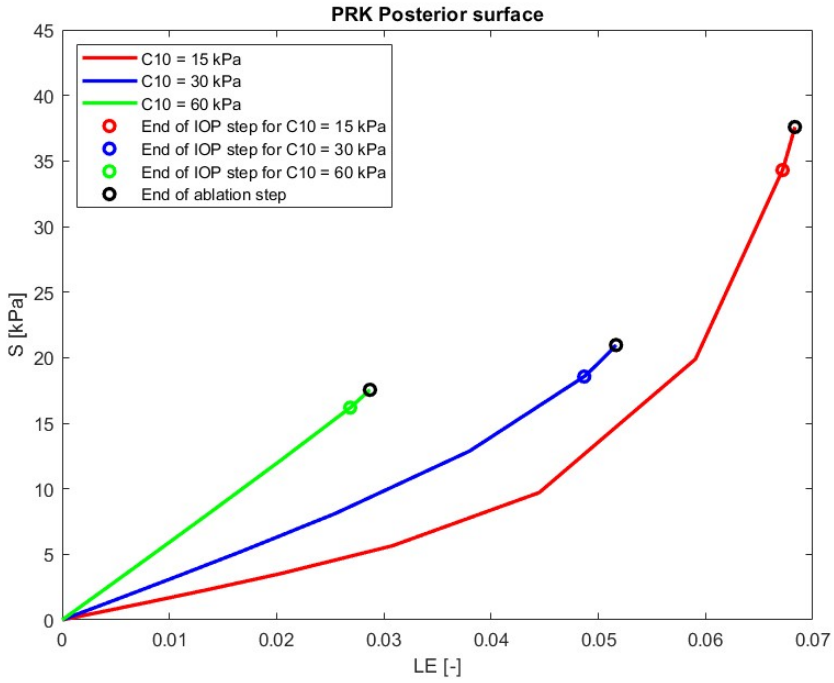

(b)

Figure 3.28: Mechanical behavior of the apical zone of the anterior (a) and posterior (b) surfaces in PRK simulation.

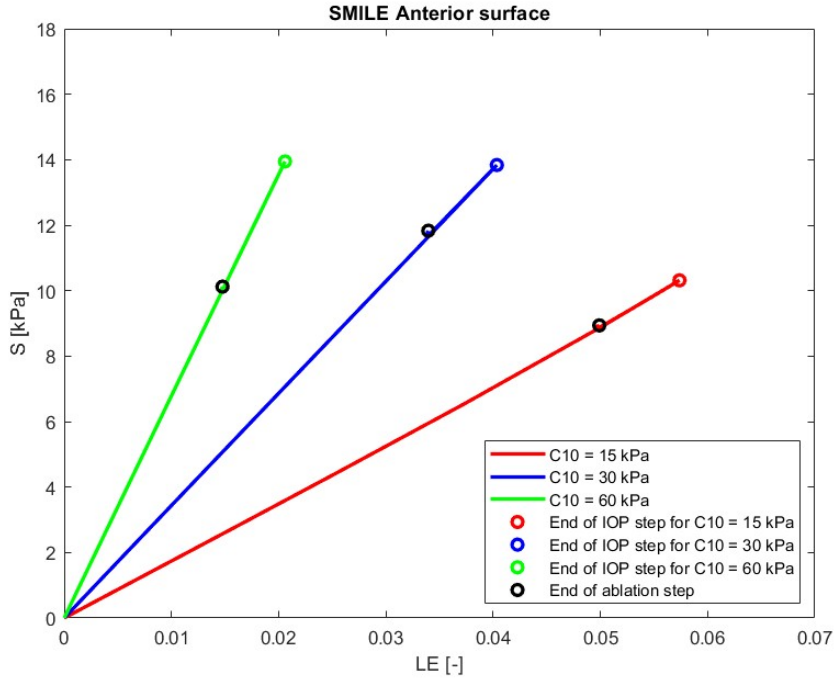

(a)

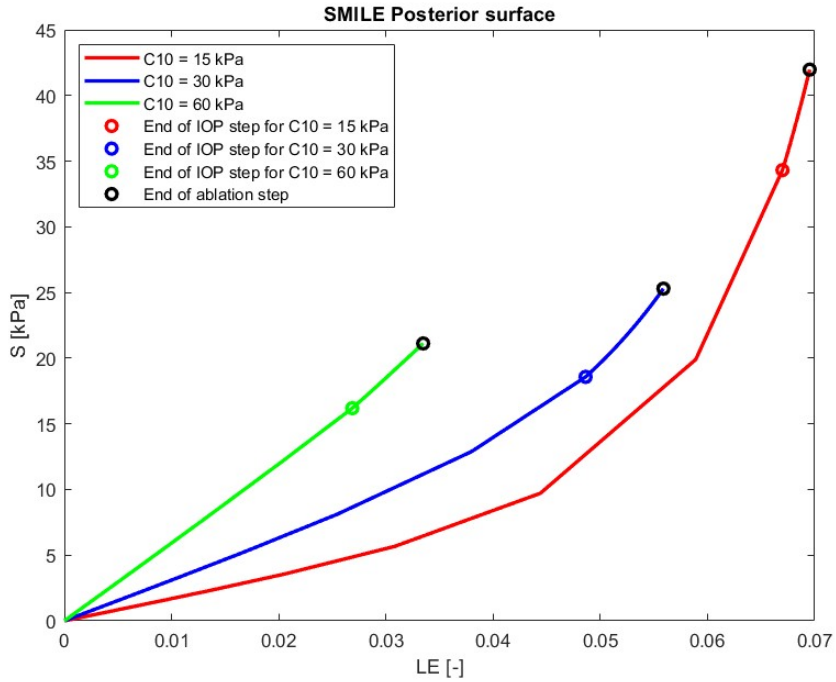

(b)

Figure 3.29: Mechanical behavior of the apical zone of the anterior (a) and posterior (b) surfaces in SMILE simulation.

C_{10} [kPa]	PRK		SMILE	
	Strain Difference [-]	Stress Difference [kPa]	Strain Difference [-]	Stress Difference [kPa]
15	0.004	1.49	-0.0075	-1.38
30	0.0068	2.81	-0.0064	-2
60	0.0048	3.5	-0.0058	-3.82

Table 3.16: Comparison of maximum principal logarithmic strain and stress differences on the anterior surfaces for PRK and SMILE at different C_{10} values.

C_{10} [kPa]	PRK		SMILE	
	Strain Difference [-]	Stress Difference [kPa]	Strain Difference [-]	Stress Difference [kPa]
15	0.0011	3.28	0.0025	7.65
30	0.003	2.4	0.0073	6.72
60	0.0018	1.36	0.0066	4.93

Table 3.17: Comparison of maximum principal logarithmic strain and stress differences on the posterior surfaces for PRK and SMILE at different C_{10} values.

4 | Discussion

The aim of this thesis was to build and validate the models of two refractive sugeries: PRK and SMILE and to determine their main differences from an opto-mechanical point of view. In order to do that, geometrical, optical and mechanical parameters were analysed, with the purpose of understanding how they affected the final outcome of the numerical simulations. The models were then validated using patient-specific data.

The choice of the most suitable boundary conditions was made based on the mechanical and optical output of the simulations. The fixed BC on the external thickness surface was applied to all the models. This choice was made because, even though the comparison between the maximum principal stresses and maximum logarithmic strains in all the corneal surfaces highlighted some differences between fixed BC and sliding BC, in the zone of interest, i.e. the OZ, the differences were negligible, as against an higher computational cost for sliding. Moreover, the dioptric correction achieved was nearly the same for both the BC.

In the second analysis, we chose to investigate the influence of the lenticule position in the corneal thickness on the optomechanical result of the simulation performace. The aim was to choose the best setup to be followed when simulating SMILE surgery. As a result, the lenticule position was set at 20% of CCT in the thickness of the cornea, coupling both higher dioptric correction and lower maximum principal stress distributions on the posterior surface of the cornea. This datum is very relevant, because it confirms what is currently done in the clinical practice. In fact, deeper lenticule positions turned out to reach lower dioptric corrections or, even worse, to cause a higher defect with respect to the initial conditions of the model. By tracing the profiles of the anterior surfaces of the models using their nodes coordinates, the value for which the pre-surgery profile coincided with the post-surgery one was in the model with ablation at 60% CCT, identifying a threshold where the surgery doesn't actually cause any change in terms of dioptric power. Calculating the dioptric correction with an OZ of radius of 4 mm (Table 3.5) confirmed the result shown in Figure 3.9. Furthermore, placing the lenticule more in depth towards the posterior surface causes an increase in the the post-surgical curvature and worsens

the pre-surgical refractive defect of the cornea. Moreover, as shown in Table 3.7 and Figure 3.11 (a), as we place the lenticule more in depth in the corneal thickness, the posterior surface of the cornea is progressively more loaded, while the anterior surface is less influenced by the lenticule positioning. This is due to the fact that, after the SMILE surgery, the anterior surface is not loaded, since the highest maximum principal stresses and logarithmic deformations concentrate under the lenticule volume, once it has been removed. Higher values of maximum principal stress on the posterior surfaces could increase the probability of post-surgical complications like ectasia, as previously explained in Chapter 1.8.3. For this reason, the choice to perform the surgery at 20% CCT is not only favourable for its optical outcomes, but also from a mechanical point of view, providing lower stress on the posterior surface.

Nevertheless, an important parameter that must be considered when evaluating models' performance is the comparison between the target and the achieved dioptric correction. Changing the dioptric target parameter means changing the whole ablation profile, controlling the thickness of the ablation tissue to be removed. Thus, the need to evaluate how the actual dioptric correction and the theoretical one differed arose and an analysis on different corrections was performed. The dioptric corrections calculated through the mean curvatures of the anterior surfaces showed the most accurate results considering an OZ radius of 4 mm. In general, comparing the optical performance of the two sugeries' simulations, PRK models reached a higher dioptric correction than the SMILE models. This was due to the fact that the PRK surgery is based on a direct action on the anterior surface, eventually eliminating a portion of the anterior surface (i.e. the OZ), while the SMILE surgery acts indirectly on the anterior surface curvature, removing a lenticule from the corneal thickness and, as a consequence of the lenticule's extraction, the curvature of the anterior surface decreases: when the internal surfaces created due the lenticule extraction adhere on each other, they cause the flattening of the anterior surface. With the theoretical ablation profiles, we did not reach the target correction in neither of the two models, but PRK was very close to the target (0.3 D of difference for a correction of -4 D). As a higher dioptric target was selected, the accuracy of the models decreased due a higher mechanical response of the corneal tissue model. Moreover, for a high correction in terms of diopters, the difference between the theoretical ablation depth and the one used in clinics increases, as it can be observed in Table 4.1.

Desired dioptric correction [D]	Theoretical Ablation Depth [µm]	PRK clinical ablation depth [µm]	SMILE clinical ablation depth [µm]
-1	14	16	33
-2	28	31	51
-3	42	46	69
-4	56	60	85
-5	70	75	101

Table 4.1: Theoretical and clinical ablation depths in PRK and SMILE models varying the desired dioptric correction parameter (with an ablation OZ of 6.5 mm).

We obtained the clinical information of Table 4.1 from our clinical partner, towards the end of the development of the current work thesis, given that this information is not currently available in literature. Therefore, due to the poor optical performance of the SMILE model, we repeated the simulations with different dioptric target by applying the real clinical ablation depth that is used when SMILE surgery is performed. This analysis on SMILE surgery, that considered a lenticule with a border thickness of 15 µm, verified that imposing a desired dioptric correction increased of the 10%, which affects the ablation depth, gives a better outcome in terms of dioptrical correction, providing a correspondence between the target dioptric correction and the achieved one. In Figure 4.1 the dioptric corrections obtained both for PRK and SMILE models with theoretical ablation profiles are reported, in comparison with the SMILE clinical model outcomes and the desired dioptric correction.

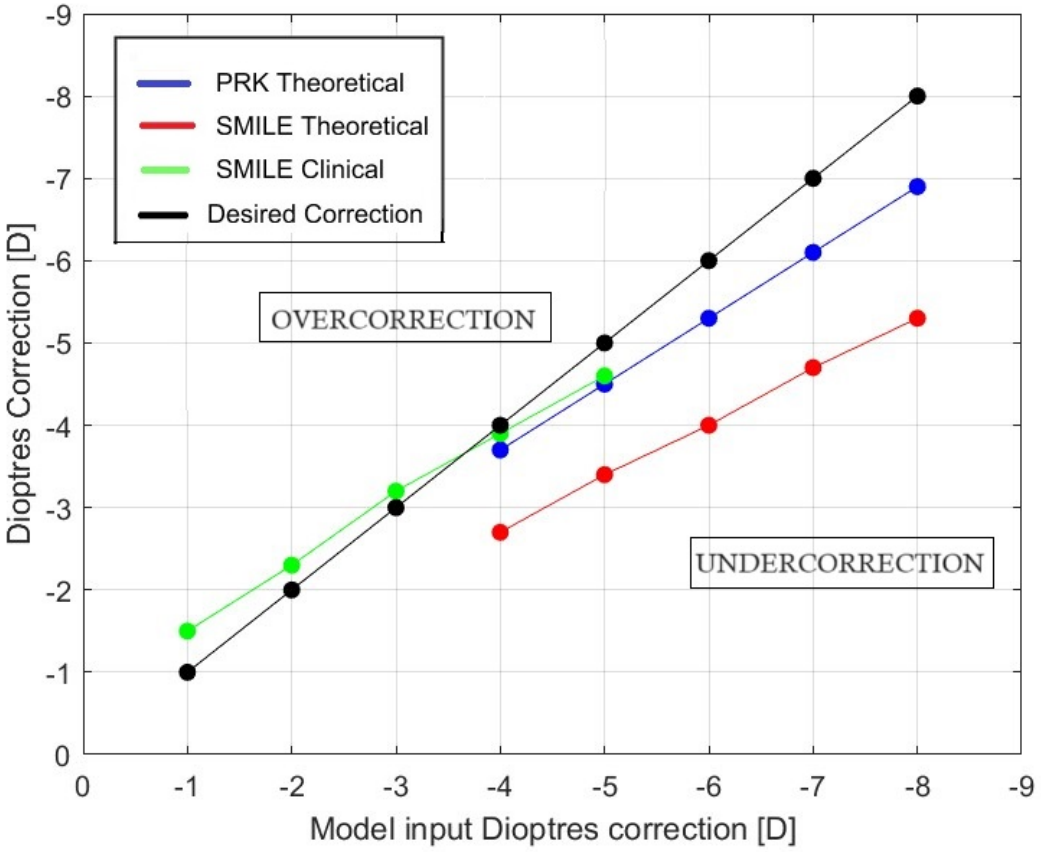

Figure 4.1: Theoretical PRK and SMILE [38] correction and SMILE clinical correction vs target dioptric.

The influence of the dimension of the OZ was also investigated, keeping in mind that changing it means also changing the thickness of the tissue to be removed (Table 2.2). Theoretically, different optical zone diameters with corresponding ablation depths should give the same dioptric correction. By changing the diameter of the optical zone of the ablation, for both PRK and SMILE, we obtained slightly different optical outcome (considering the same OZ fitting radius) (See Table 3.10). This results does not confirm the theoretical approach, used also in clinics, and could be due to the highly non linear response of the corneal model, as it was deeply explained in the patient-specific case analysis (See Section 3.8).

Then, the influence of the CCT parameter on the opto-mechanical outcome was also investigated. The CCT variation revealed that the apical node displacement difference among the models is negligible, as well as the anterior surface maximum principal stress and maximal principal logarithmic strain distributions. Regarding the optical properties, increasing the CCT of the models means increasing the dioptric correction, both for

PRK and SMILE: when the CCT is higher, the stiffness of the corneal model increases and the mechanical response of the corneal model is lower. For this reason, the curvature correction numerically depends from the corneal mechanical deformation, which is affected by the CCT. The difference in dioptric correction, however, turned out to be low for both PRK and SMILE models (the difference between the 600 µm CCT model and the 500 µm CCT model is of 0.3-0.4 D for PRK and 0.4-0.5 D for SMILE).

Knowing that the dioptric correction depends on the deformation of the cornea, the biomechanical sensitivity analysis was carried out to investigate the influence of the mechanical parameters. It showed that the best combination of material parametersshould be C_{10}=15 kPa, k_1=30 kPa, k_2=600 kPa to reach the highest dioptric correction. The C_{10} coefficient, in particular, is lower than in all the previous simulations, meaning that a softer material seems to reach a better optical outcome.

The Montecarlo analysis allowed to build, through linear regression, two relationships between the CCT and the actual dioptric correction, one for PRK model and one for SMILE model (after imposing a certain desired dioptric correction) (Equation 3.1, 3.2, Figure 4.2).

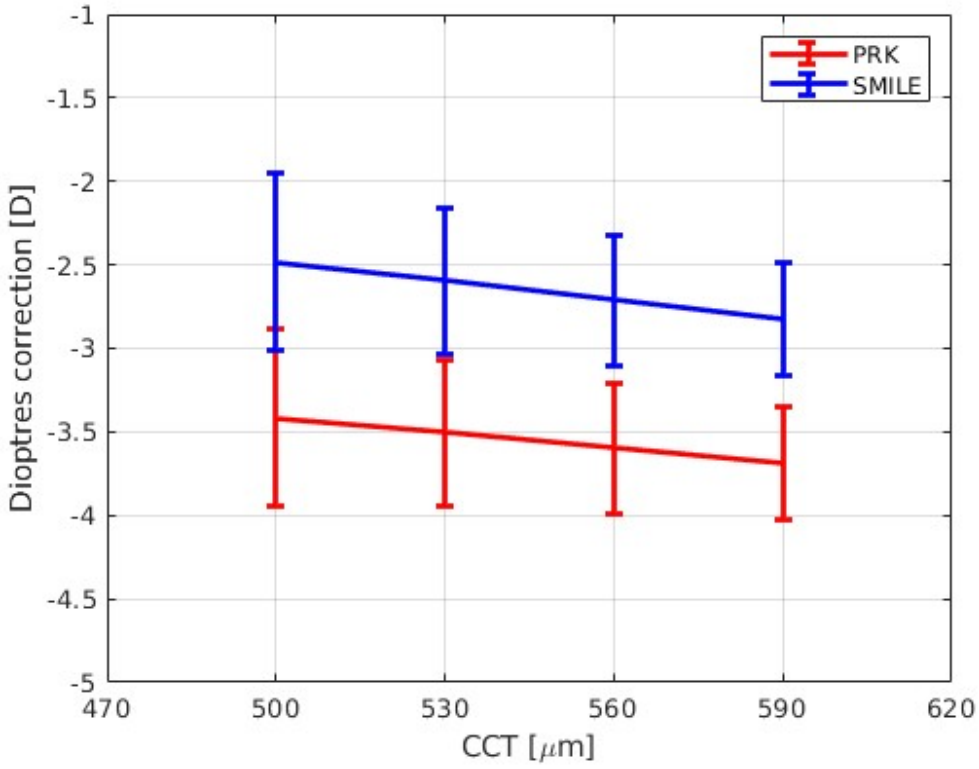

Figure 4.2: Linear regression lines that relate the CCT to the dioptric correction reached for -4D correction.

The simulations that led to these relationships considered a range of variation of the material parameters, so the linear dependence can be applied for all the models that are built considering a material with parameters in those ranges. Moreover, thanks to this analysis, the material parameters that provide the best dioptric corrections were determined, which turned out to be: C_{10} = 17.37 kPa, k_1 = 28.42 kPa, k_2 = 494.42 kPa. As in the biomechanical sensitivity analysis, this analysis showed too that a softer material would be more suitable for achieving the correction of a refractive defect, also highlighting that missed target correction could be due to patient's mechanical properties, which are unknown and it is not possible to determine them through any current clinical evaluation or test.

Moving to the last part of this thesis' work, patient-specific models were built in order to validate corneal surgeries' models. The optical analysis revealed that the models matched the patient's pre- and post-surgical topographical data. Moreover, the best dioptric correction was reached for a softer material, with a C_{10} =15 kPa, k_1=20kPa, k_2=400 in PRK. This result agrees with the biomechanical sensitivity and the Montecarlo analysis results: the material parameters that better corrected the optical defect are the ones of a softer material. On the other hand, in SMILE, the softest and the hardest materials gave similar results in terms of correction, one providing a slight undercorrection and the other an overcorrection: the influence of the material parameters has to be further investigated, as well as the optical ones. Thus, the dioptric corrections in both models don't vary linearly in function of the C_{10} coefficient: the lowest correction is reached for the intermediate value of C_{10}. Once again, this could be probably due to the highly non-linear behaviour of the corneal tissue, thus further investigation on the effect of patient-specific material properties on the optical outcome of refractive interventions is required.
Moreover, the patient-specific simulations of PRK and SMILE highlighted the different mechanical behaviors of the two surgeries: in SMILE, in fact, the highest stresses distribute in a smaller volume than in PRK, only in the corneal portion below the lenticule zone, while the anterior portion remains unloaded. Nevertheless, in PRK, the stresses distribute through all the corneal thickness, reaching lower absolute values, because the ablation is performed directly onto the anterior surface. For this reasons, the deformations are higher in SMILE, while PRK better preserves the mechanical integrity of the structure. Consequently, SMILE surgery seems to cause higher mechanical imbalances to the corneal structure with respect to PRK, which is highly less invasive.
It was possible to understand all the differences between the two simulations by analyzing the difference in terms of stress and strain distribution between the pre- and post-surgical configurations of the models. Finally, a softer material means that the model reaches

a higher deformation state when it is pressurized (due to the effect of recovering the stress-free configuration, having as a consequence a lower deformation when the surgery is simulated, since the strains are already high.

5 | Conclusions and future developments

This Chapter resumes the conclusions extracted from the fulfillment of this work. In addition, some future lines in the research of refractive surgery simulations are suggested.

5.1. Conclusions

A numerical methodology has been developed to simulate refractive surgeries. In particular, PRK and SMILE surgeries were modeled by means of finite element methods. Numerical simulations allow to define the mechanical and optical outcome of the modeled surgeries throughout the analysis of different parameters, which are set to define the model itself. Two different geometries with different complexities were taken into account: conical models, where the geometry was built starting from a conic approximation, and patient-specific models, where the geometry was defined based on patient's topography. The corneal material behaviour has been modelled using a non linear anisotropic hyperelastic formulation. The principal aspects observed are described below:

- The finite element model can be uniquely defined by the cornea embedded in the limbus. The fixed B.C.s provide low computational cost, without sacrificing the performance in surgery simulations.
- The lenticule position in the corneal thickness in SMILE surgery has a significant influence on the dioptric correction achieved: in conic model, the maximum value is achieved for the depth of 20% of the CCT. Moreover, it causes the lowest stress on the posterior surface of the cornea. This lenticule location is the one used in clinical practice, confirming that it allows to provide the highest dioptric correction while making it less prone to be affected by ectasia disease and keratoconus.
- The optical zone radius parameter determines the thickness of the lenticule and shows the highest curvature correction for a $R_{OZ} = 4$ mm.

- In the clinic, the ablation thickness in SMILE is much higher than in PRK, as an additional thickness of 15 microns is added to avoid the lenticule rupture when it is removed. The SMILE models based on the clinical data reveal that the achieved dioptres correction reaches the taget ones for low dioptric corrections, but higher corrections are more difficult to be reached, since the accuracy decreases.
- Higher CCTs allow higher dioptric correction, because these models behave more rigidly: the mechanical analysis highlighted the importance, in particular, of the thickness and C_{10} coefficients, as they mostly influenced the mechanical outcomes of the simulations.
- Knowing the CCT of the patient, the actual dioptres correction can be determined, through the linear relations defined in the Montecarlo material based analysis of both surgeries.
- The patient-specific models revealed that a softer material was more suitable to obtain the patient's dioptric correction, especially for SMILE simulation. This result is aligned with the Montecarlo analysis result, in which the highest curvature correction was reached using a softer material than the one selected from literature [53], which was applied in all the conic model based previous parameters analysis.
- PRK models always reach a better dioptrical correction than SMILE model, due to the direct action of the laser on the anterior surface of the cornea rather than on the corneal thickness like in SMILE.
- PRK surgery provides higher mechanical stability in corneal thickness, while the lenticule extraction performed in SMILE causes a concentration of stresses and deformations right under the ablation zone, while the anterior surface remains unloaded.

5.2. Limits and Future Developments

The main limits of this work are related to the geometries considered for part of the models, which are simplified ideal corneal geometries, built using a conic approximation. This inevitably affects the final results, making it not possible to take into account the real corneal asymmetries and irregularities, even though it allows to simply understand the influence of the models' parameters on the simulations. On the other hand, the patient-specific models are built based on the patient's topography, ensuring a more precise reconstruction of the corneal surfaces.
The analysis on the parameters of the conic model leaves some issues. First, the accuracy

of the numerical models decreased for higher dioptric corrections (greater than -4 D). This is due to the chosen model material constants. Therefore, as main future development, further investigations would be required on the influence of mechanical properties on patient-specific models. Moreover, the choice of the ablation OZ turned out to be an important factor of influence in the optical output of the simulations, which is in contrast with the theory, that assesses that different OZ radii correspond to different ablation depths, but should give the same dioptric correction, which was not true (Table 3.10). The highly non linear response of the model, that explains this effect, should be further investigated through patient-specific models.

Nevertheless, a more targeted analysis of the patient-specific model can be carried out, more deeply investigating the optical parameters that are considered, in order to define the wavefront aberrations, as well as the mechanical ones, further investigating the material parameters. In this way, the implementation of a more specific model that can define the ablation profile based on both wavefront aberrations and mechanical response could be carried out and it can be eventually become a tool that allows optimal correction, further employed by clinicians to assess the specific needs of a patient, without necessarily relying on nomograms.

Moreover, pathological models could be also taken into account in the future, such as keratoconus-affected corneas. This disease, in fact, can arise in patients that underwent refractive surgeries: a model that simulates this condition, with a heterogeneous material model in the corneal thickness, could be considered as a future work.

Bibliography

[1] URL https://lasiksurgeons.com/anatomy-of-the-eye/.

[2] Encyclopedia britannica. https://www.britannica.com/science/refractive-index., 2023.

[3] Blindness and vision impairment. https://www.who.int/news-room/fact-sheets/detail/blindness-and-visual-impairment., 2023.

[4] V. AH. Past and present of corneal refractive surgery: a retrospective study of long-term results after photorefractive keratectomy and a prospective study of refractive lenticule extraction. *Acta Ophthalmol.*, 2014.

[5] Z. J. P. D. e. a. Ariza-Gracia, M.Á. Automatized patient-specific methodology for numerical determination of biomechanical corneal response. *Ann Biomed Eng.*, 44: 1753–1772, 2016.

[6] K. S. Belin MW. An introduction to understanding elevation-based topography: how elevation data are displayed–a review. *Clin Exp Ophthalmol.*, 37:14 –29, 2009.

[7] J. P. Bergmanson. Clinical ocular anatomy and physiology. *Texas Eye Research and Technology Center*, 2020.

[8] D. G. D. M. W. B. R. A. J. Bernardo T. Lopes, Isaac C. Ramos. Detection of ectatic corneal diseases based on pentacam. *Z. Med. Phys.*, 26, 2016.

[9] R. K. M. R. D. S. M. M. M. J. M. D. D. A. Bower, Kraig S. MD; Sia. hd. chronic dry eye in photorefractive keratectomy and laser in situ keratomileusis: Manifestations, incidence, and predictive factors. *Journal of Cataract Refractive Surgery*, 41, 2015.

[10] C. Y. e. a. Chua SY, Sabanayagam C. Age of onset of myopia predicts risk of high myopia in later childhood in myopic singapore children. *Ophthalmic Physiol Opt.*, 36, 2016.

[11] F. Conti. *Fisiologia Medica (Second edition)*, volume 2. Edi-Erme, 2010. ISBN 9788870513479.

[12] H. S. Dua and A. Azuara-Blanco. Limbal stem cells of the corneal epithelium. *Survey of Ophthalmology*, 44(5):415–425, 2000.

[13] A. Elsheikh, D. Alhasso, and P. Rama. Biomechanical properties of human and porcine corneas. *Experimental Eye Research*, 86(5):783–790, 2008.

[14] L. B. V. P. V. R. R. C. E. A. D. D. A. R. Esporcatte LPG, Salomão MQ. Jr. biomechanical diagnostics of the cornea. *Eye Vis (Lond)*, 5, 2020.

[15] N. et al. Optics of the average normal cornea from general and canonical representations of its surface topography. *J. Opt. Soc. Am. A*, 23(2):219–231, 2006.

[16] K. F. H. H. M. A. Feizi S, Jafarinasab MR. Central and peripheral corneal thickness measurement in normal and keratoconic eyes using three corneal pachymeters. *J Ophthalmic Vis Res.*, 9:296–304, 2014.

[17] C. E. Florian Rüfer, Anke Schröder. White-to-white corneal diameter: normal values in healthy humans obtained with the orbscan ii topography system. *Cornea*, 24:259–261, 2005.

[18] M. J. D. C. D. Fuest M, Yam GH-F. Prospects and challenges of translational corneal bioprinting. *Bioengineering*, 7:71, 2020.

[19] Guyton and Hall. *Textbook of Medical Physiology*. Elsevier Inc., 2011.

[20] L. J. e. a. Hsu WM, Cheng CY. Revalence and causes of visual impairment in an elderly chinese population in taiwan: the shihpai eye study. *Ophthalmology*, 111, 2004.

[21] E. Janunts, M. Kannengießer, and A. Langenbucher. Parametric fitting of corneal height data to a biconic surface. *Zeitschrift für Medizinische Physik*, 25(1):25–35, 2015.

[22] F. S. M. G. A. S. B. A. R. Jeewan S Titiyal, Manpreet Kaur. Small incision lenticule extraction (smile) techniques: patient selection and perspectives. *Clinical Ophthalmology*, 12(7):1967, 2018.

[23] B. JI. Modification of refraction by means of intracorneal inclusions. *Ophthalmol Clin.*, 6, 1966.

[24] A. R. G. . D. B. L. J. Jiménez, J. R. Equation for corneal asphericity after corneal refractive surgery. *Journal of Refractive Surgery*, 19(1):65–69, 2003.

[25] H. JO. Extensibility of the normo-hydrated human cornea. *Acta Ophthalmol Scand.*, 73:12–17, 1995.

[26] P. F. N. L. Johan Germundsson, Georgios Karanis. Age-related thinning of bowman's layer in the human cornea in vivo. *Invest Ophtalmol Vis Sci*, 54:6143–9, 2013.

[27] L. H. Kim TH, Lee D. The safety of 250 microm residual stromal bed in preventing keratectasia after laser in situ keratomileusis (lasik). *J Korean Med Sci.*, 22(2), 2007.

[28] H. F. Kling S. Corneal biomechanics - a review. *Ophthalmic Physiol Opt.*, 37:240–252, 2017.

[29] M. H. E. Krachmer, J. Mannis. *CORNEA. Fundamentals, Diagnosis and Management.* MOSBY, 20110.

[30] E. P. L. J. Müller and G. F. Vrensen. The specific architecture of the anterior stroma accounts for maintenance of corneal curvature. *British Journal of Ophtalmology*, 85: 437–443, 2001.

[31] S. B. Laura E. Downie. Bcla clear - anatomy and physiology of the anterior eye. *British Contact Lens Assosiacion*, 44:133, 2021.

[32] S. G. . A. D. A. Lindsay, R. Descriptors of corneal shape. *Optometry and Vision Science*, 1998.

[33] T. Liu and J. Bai. Expert consensus on the removal of corneal stromal lens with femtosecond laser in chinese ophthalmology association. *Chinese Journal of Ophthalmology*, 50(1):15–21, 2016.

[34] V. A. S. M. Dubbelman and G. L. V. D. Heijde. The shape of the anterior and posterior surface of the aging human cornea. *Vision Research*, 46:993–1001, 2006.

[35] S. O. L. M. A. M. A. M. Vilaseca, F. Díaz-Doutón and J. Pujol. Optics of astigmatism and retinal image quality. *Centre for Sensors, Instruments and Systems Development (CD6) Universitat Politècnica de Catalunya (UPC).*

[36] M. Mahdian, A. Seifzadeh, A. Mokhtarian, and F. Doroodgar. Characterization of the transient mechanical properties of human cornea tissue using the tensile test simulation. *Materials Today Communications*, 26:102122, 2021.

[37] D. R. e. a. Majmudar PA, Forstot SL. Topical mitomycin-c for subepithelial fibrosis after refractive corneal surgery. *Ophthalmology*, 107, 2000.

[38] P. J. C. W. Manns F, Ho A. Ablation profiles for wavefront-guided correction of myopia and primary spherical aberration. *J Cataract Refract Surg.*, 28(5), 2002.

[39] K. M. Meek and C. Boote. The organization of collagen in the corneal stroma. *Experimental Eye Research*, 78(3):503–12, 2004.

[40] K. M. Meek and C. Knupp. Corneal structure and transparency. *Progress in Retinal and Eye Research*, 49:1–16, 2015.

[41] S. MS. Anatomy of cornea and ocular surface. *Indian J Ophthalmol.*, 66:190–194, 2018.

[42] M. J. Munnerlyn CR, Koons SJ. Photorefractive keratectomy: a tecnique for laser refractive surgery. *J Cataract Refract Surg.*, 14(1):46–52, 1998.

[43] S. Ormonde. Refractive surgery for keratoconus. *Clinical and Experimental Optometry*, 96(2):173–182, 2013. doi: https://doi.org/10.1111/cxo.12051. URL `https://onlinelibrary.wiley.com/doi/abs/10.1111/cxo.12051`.

[44] H. G. Pandolfi A. Three-dimensional modeling and computational analysis of the human cornea considering distributed collagen fibril orientations. *J Biomech Eng.*, 130, 2008.

[45] A. Ranelle. Hyperopia and myopia. `https://www.ranelle.com/lasik/hyperopia-and-myopia-2/`, 2016.

[46] H. C. S. C. K. K. F. I. K. R. Ratkay-Traub I, Juhasz T. Ultra-short pulse (femtosecond) laser surgery: initial use in lasik flap creation. *Ophthalmol Clin North Am.*, 14, 2001.

[47] R. J. Reinstein DZ, Archer TJ. Mathematical model to compare the relative tensile strength of the cornea after prk, lasik, and small incision lenticule extraction. *J Refract Surg*, 29(7):454–60, 2013.

[48] J. G. C. F. A. M. D. S. F. J. L. W. Robert N. Weinreb, Christopher K.S. Leung and K. R. Martin. Primary open-angle glaucoma. *Nature Reviews Disease Primers*, 2, 2016.

[49] W. SA. Last a. management of corneal abrasions. *Am Fam Physician*, 70(5):123–8, 2004.

[50] P. D. Sami G. El Hage, OD and M. F. Norman E. Leach, OD. Tangential or sagittal dioptric plots: Is there a difference? *ICLC*, 26, 1999.

[51] S. B. Sri Ganesh and U. Patel. Comparison of relex smile and prk in terms of visual and refractive outcomes for the correction of low myopia. *International Ophthalmology*, 38(3):1147–1154, 2018.

[52] S. B. Susana Marcos, Daniel Cano. Increase in corneal asphericity after standard

laser in situ keratomileusis for myopia is not inherent to the munnerlyn algorithm. *Journal of Refractive Surgery*, 2003.

[53] H.-M. H. Wang S. Constitutive modeling of corneal tissue: Influence of three-dimensional collagen fiber microstructure. *J Biomech Eng.*, 143, 2021.

[54] W. M. Wolle MA, Randleman JB. Complications of refractive surgery: Ectasia after refractive surgery. *Int Ophthalmol Clin.*, 56, 2016.

[55] W. B. W. Ya Xing Wang, Liang Xu and J. B. Jonas. Intraocular pressure and its normal range adjusted for ocular and systemic parameters. the beijing eye study. *PLoS ONE*, 13(5):1–16, 2018.

List of Figures

1.1 Eye anatomy [1]. 2
1.2 Diagram of the corneal structure in transverse section [49]. 3
1.3 (a) Histological section of a human cornea showing the ultrastructure of the three main layers and illustration of orthogonally aligned collagen lamellae present in the human corneal stroma[18, 53] and (b) second harmonic generated (SHG) microscopy of face views from the front of the cornea [40]. 4
1.4 Collagen fibers orientation [53]. 5
1.5 Pentacam device 6
1.6 Corcis ST device. 7
1.7 (a) Pressure deformation results of six human corneas with 65-79 years of age presented as examples of human corneal behaviour under inflation test [13] (b) Apical rise–pressure curves: the comparison between experimental data (throughout the inflation test) and six different numerical cases of Wang and Hatami work [53].. 9
1.8 Force-time graph (a) and Strain-stress curve (b) of the uniaxial-tensile test [36]. 10
1.9 The phenomenon of refraction of light [2]. 11
1.10 The refractive indexes of the eye [19]. 12
1.11 Images formation on the retina. (a) Emmetropy: the object of vision projects directly on the retinal plate. (b) In a myopic eye, the image projects in front of the retinal plate. (c) In a hyperopic eye, the image projects behind the retinal plate [45]. 13
1.12 Plots showing image formation in an eye with an astigmatic refractive error. The principal meridians (y, z) and the first and second focal lines (F'y, F'z) are shown [35]. 14
1.13 Correction of vision defects through concave and convex lenses. 15
1.14 Corneal reshaping in (a) correction of myopia and (b) correction of hyperopia. [37]. 16

1.15 Side view of lenticule removal (the blue portion is the one to be removed in order to lower the cornea superficial curvature for myopia treatment) in (a) PRK surgery, (b) LASIK surgery, (c) SMILE surgery. 18
1.16 Picture of a keratoconic eye. 19

2.1 Pentacam topography of a healthy patient, used to build the geometry model by a conic approximation (the data employed to build the model are highlighted in red). 22
2.2 Conic section and asphericity changes [32]. 23
2.3 Three-dimensional geometry of the cornea defined by a conic model point cloud on MATLAB 2023a: a more dense anterior part corresponds to the OZ, both for PRK and SMILE. 24
2.4 Mesh of the corneal model: quadratic tetrahedric elements from ABAQUS 6.13. 25
2.5 Visualization of the fibers of the anterior surface of the cornea using PARAVIEW: in red the circunferential orientetion of the fibers of the external region, in blue and green the N-T and I-S directions within the central region. 28
2.6 Boundary conditions application on ABAQUS 6.13 on the thickness set of elements of the cornea model: (a) fixed B.C., (b) sliding B.C. 29
2.7 Influence of the IOP in the corneal shape [5]. 29
2.8 Algorithm for identification of the stress-free configuration [5]. 30
2.9 Graphical representation of the algorithm for identification of the stress-free configuration [5]. 30
2.10 Models of PRK, where the ablation region is highlighted. 31
2.11 IOP load application (in purple) on ABAQUS 6.13 on the posterior surface of the cornea model. 32
2.12 Models of SMILE, the ablation region is highlighted. 32
2.13 Elements composing the top (a) and bottom (b) surfaces of the cornea right after ablation selected on ANSA pre-processor by BETA-CAE systems v22.0.1. 33
2.14 Sagittal curvature. 34
2.15 Zernike polynomial fitting error 35
2.16 ABAQUS representations of the ablation elements for SMILE with lenticule position depth at 20% CCT (a), 30% CCT (b), 40% CCT (c), 50% CCT (d), 60% CCT (e), 75% CCT (f) with an OZ of 3 mm and CCT from Pentacam data. 37

2.17 Elements selection (in red) on the anterior and posterior surface of PRK (a) and SMILE (a) models for the mechanical analysis. 39
2.18 Reconstruction of missing portion of surface through Zernike polynomials. 43
2.19 Schematic representation of a biconic surface [21] 44
2.20 Pentacam topography of the PRK patient. 45
2.21 Treatment details for PRK surgery. 46

3.1 Maximum principal stress distribution [kPa] in PRK simulation. 50
3.2 Maximum principal logarithmic strain distribution [-] in PRK simulation. . 51
3.3 Maximum principal stress distribution [kPa] in SMILE simulation. 52
3.4 Maximum principal logarithmic strain [-] distribution in SMILE simulation. 52
3.5 Pre-surgical mean curvatures for fixed (a) and sliding (b) BCs; post-surgical mean curvatures for PRK with fixed (c) and sliding (d) BC, post-surgical mean curvatures for SMILE with fixed (e) and sliding (f) BC 55
3.6 Anterior surface (a) and posterior surface (b) profiles for PRK and SMILE models with fixed BC 56
3.7 Anterior surface (a) and posterior surface (b) profiles for PRK and SMILE models with sliding BC. 57
3.8 Anterior surface mean curvatures in SMILE with an ablation depth of 75% of CCT. (a) Pre-surgery mean curvatures. (b) Post-surgery mean curvatures. 60
3.9 Anterior surface (a) and posterior surface (b) profiles for SMILE with different lenticule positions in the corneal thickness: growing percentage of total CCT. 60
3.10 Anterior surface displacement difference(in module) between pre-surgery and post-surgery configurations (a) for growing lenticule position depths in SMILE and curvature correction for each lenticule position (b). 61
3.11 Maximum principal stress distributions (a) and maximum principal strain distributions (b) in SMILE models with lenticule position at 20 % of CCT and 75 % of CCT. 63
3.12 Anterior surface (a) and posterior surface (b) profiles for PRK with growing dioptric corrections imposed. 65
3.13 Anterior surface (a) and posterior surface (b) profiles for SMILE with growing dioptric corrections imposed. 65
3.14 Anterior surface pre-surgery apical displacement displacement difference (a) and theoretical vs actual dioptres correction (b) for PRK. 66

3.15 Anterior surface pre-surgery apical displacement displacement difference (a) and theoretical vs actual dioptres correction (b) for SMILE. 67
3.16 Desired dioptric correction VS actual dioptric correction obtained in SMILE models, in function of the lenticule thickness [µm], built based on clinical data, imposing a 10% more of dioptric correction in the input data. 68
3.17 Dioptric correction variation depending on CCT for PRK (a) and SMILE (b) models. The desired dioptric correction is -4 D. 72
3.18 Anterior surface apical nodes displacement difference between pre-surgical and post-surgical configurations in module for PRK (a) and SMILE (b) with different CCTs. 73
3.19 Anterior surface maximal principal stress (a) and logarithmic strain differences between post-surgery and pre-surgery configurations (b) for PRK and anterior surface maximal principal stress (c) and logarithmic strain difference between post-surgery and pre-surgery configurations (d) for SMILE for varying CCTs. 74
3.20 Influence of material properties, IOP and corneal thickness on the dioptric correction for PRK (a) and SMILE (b). 76
3.21 Main effects plots: influence of material properties, IOP and corneal thickness on the stresses (a), (b) and deformations (c), (d) of anterior (a), (c) and posterior (b), (d) surfaces before performing ablation. 77
3.22 Main effects plots: influence of material properties, IOP and corneal thickness on the stresses on the posterior surfaces of PRK (a) and SMILE (b) after performing ablation. 78
3.23 Dioptric correction variation depending on the CCT, with different material parameters, determined by a linear regression for PRK (a) and SMILE (b). 79
3.24 Maximum principal displacement difference in PRK (a) and SMILE (b) patient-specific models. 81
3.25 Maximum principal strain difference in PRK (a) and SMILE (b) patient-specific models. 82
3.26 Maximum principal stress difference in PRK (a) and SMILE (b) patient-specific models. 83
3.27 Pentacam-derived patient anterior surface sagittal curvature map (a) and anterior surface sagittal curvature map of the patient-specific model(b). . . 84
3.28 Mechanical behavior of the apical zone of the anterior (a) and posterior (b) surfaces in PRK simulation. 88
3.29 Mechanical behavior of the apical zone of the anterior (a) and posterior (b) surfaces in SMILE simulation. 89

4.1 Theoretical PRK and SMILE [38] correction and SMILE clinical correction vs target dioptric. 94
4.2 Linear regression lines that relate the CCT to the dioptric correction reached for -4D correction. 95

List of Tables

2.1 Ablation depths in PRK and SMILE models varying the desired dioptric correction parameter (with an OZ of radius = 3 mm). 24
2.2 Ablation depths in PRK and SMILE models varying the OZ radius parameter (with a desired dioptric correction of -4 D). 24
2.3 Material parameters used in the surgery simulations. 27
2.4 Parameters for the clinical data based SMILE simulations. 38
2.5 Set of parameters for the full factorial analysis. 40
2.6 Mechanical Sensitivity analysis set of parameters. 41
2.7 Set of parameters for the Montecarlo analysis 42
2.8 Three sets of parameters for the material of the patient-specific models. . . 44

3.1 Maximum principal logarithmic strain and maximum principal stress for anterior and posterior apical nodes in fixed BC and sliding BC in PRK analysis 51
3.2 Maximum principal logarithmic strain and maximum principal stress for anterior and posterior apical nodes in fixed BC and sliding BC in SMILE analysis 53
3.3 Anterior surface ellipsoid-fitted mean curvatures for fixed and sliding BCs in PRK. 54
3.4 Anterior surface ellipsoid-fitted mean curvatures for fixed and sliding BCs in SMILE. 54
3.5 Mean curvature variations in SMILE models moving the lenticule through the corneal thickness (the desired correction was set at -4 D). 59
3.6 Maximum principal stresses and maximum principal strain differences between the post-surgical and pre-surgical apical elements on the anterior surface. 62
3.7 Maximum principal stresses and maximum principal logarithmic strain differences between the post-surgical and pre-surgical apical elements on the posterior surface. 62

3.8 Ellipsoid-fitted mean curvature variations and achieved dioptric corrections (i.e. difference between pre- and post- surgery curvatures) imposing different dioptric correction input for PRK and SMILE, with an OZ radius of 3, 3.5 and 4 mm. 64
3.9 Ellipsoid-fitted mean curvatures and achieved dioptric corrections for SMILE models, based on the clinical ablation depths. 67
3.10 Curvature variations and achieved dioptric corrections varying the OZs in PRK and SMILE. 69
3.11 Ellipsoid-fitted curvature variations and achieved dioptric corrections imposing different CCTs for PRK and SMILE, with an OZ radius of 3, 3.5 and 4 mm. 71
3.12 Highest dioptric corrections (i.e. ellipsoid-fitted curvature variations) reached in PRK and SMILE models and respective material and geometrical parameters. 75
3.13 K1, K2, Km, C, α values derived from the Pentacam data of the patient. . 85
3.14 K1, K2, Km, C, α values for PRK patient-specific model, varying the C_{10} coefficient. 85
3.15 K1, K2, Km, C, α values for SMILE patient-specific model, varying the C_{10} coefficient. 86
3.16 Comparison of maximum principal logarithmic strain and stress differences on the anterior surfaces for PRK and SMILE at different C_{10} values. 90
3.17 Comparison of maximum principal logarithmic strain and stress differences on the posterior surfaces for PRK and SMILE at different C_{10} values. . . . 90

4.1 Theoretical and clinical ablation depths in PRK and SMILE models varying the desired dioptric correction parameter (with an ablation OZ of 6.5 mm). 93

Acknowledgements

This project has received funding from the European Union's Horizon 2020 research and innovation program under the Marie Sk lodowska-Curie grant agreement No 956720 and the Department of Industry and Innovation (Government of Aragon) through the research group Grant T24–20R (cofi724 nanced with Feder 2014-2020: Construyendo Europa desde Aragon). Part of the work was performed by the ICTS "NANBIOSIS" specifically by the High Performance Computing Unit (U27), of the CIBER in Bioengineering, Bio727 materials and Nanomedicne (CIBER-BBN at the University of Zaragoza). A special mention to the clinical feedback and support provided by Barraquer Ophthalmology Center (Barcelona, Spain).